TECHNISCHE UNIVERSITÄT WIEN

DIPLOMARBEIT

Synthesis, structure and properties of the organic-inorganic plastic crystal solid solution system $[(CH_2CH_3)_4N]_x[(CH_3)_4N]_{1-x}[FeBrCl_3]$

Ausgeführt am Institut für

Angewandte Synthesechemie

der Technischen Universität Wien

unter der Anleitung von Univ.Prof. Dipl.-Ing. Dr.techn. Wolfgang Linert,

Univ.Prof. Dipl.-Ing. Dr.techn. Mari-Ann Einarsrud (Norwegian University of Science and Technology) und Dipl.-Ing. Julian Walker (Norwegian University of Science and Technology)

durch

Simon Scherrer

6.5.2020

Contents

I hereby declare that I am the sole author of this work. No assistance other than that which is permitted has been used. Ideas and quotes taken directly or indirectly from other sources are identified as such. This written work has not yet been submitted in any part.

1. Abstract

Recent decades have seen an ever-increasing demand for functional materials, putting pressure on researchers to find materials with lower costs and environmentally friendly manufacturing, while still maintaining highly specialized electrical properties, such as piezo-, ferro- and dielectric behavior. A new class of plastic molecular ferroelectrics, based on the tetramethylammonium bromotrichloroferrate(III) ($[(CH_3)_4N][FeBrCl_3]$) was investigated as a possible alternative to currently used ceramic metal-oxides. The potential for additional and enhanced properties was explored by continuously replacing the organic tetramethylammonium-cations with tetraethylammonium-cations ($[(CH_2CH_3)_4N]^+$) up to 100 % and thus studying the full compositional range of the solid solution system using low-temperature aqueous evaporation synthesis.

The resulting $[(CH_2CH_3)_4N]_x[(CH_3)_4N]_{1-x}[FeBrCl_3]$ (x = 0 – 1) system co-crystallized in two crystal structures, *Amm2* (orthorhombic) and *P6₃mc* (hexagonal) at room temperature. These space groups belong to the end members of the system, $[(CH_3)_4N][FeBrCl_3]$ and $[(CH_2CH_3)_4N][FeBrCl_3]$. Limited solubility of the substituted organic cation was observed in the reciprocal phase by tracking changes in the lattice parameters and phase weight percentages as a function of composition, based on structure fitting of powder X-ray diffraction (powder-XRD) profiles using Rietveld refinement. The exact ratio of the phases in the metastable solid solution and the solubility of the substituted cation, as well as the morphology of the crystals studied by scanning electron microscopy, depended on the crystallization rate, polarity of the solvent and thermal history of the material. Differential scanning calorimetry (DSC) revealed that all compositions had a plastic mesophase transition between 100 and 150 °C depending on the composition. Notably the mesophase allows for low temperature plastic deformation of the crystals, which provides a potential pathway for uncomplicated, low cost manufacturing of complex shapes.

Polycrystalline discs of 250 – 450 µm in thickness were produced by hot pressing crystals together and the resulting discs were used for electrical measurements. Ferroelectric behavior of $[(CH_3)_4N][FeBrCl_3]$ was confirmed, in addition to high strains (0.109 %) and piezoelectric d_{33} value of -7/7 pC/N using a Berlincourt piezometer. Switching kinetics were investigated, revealing a saturation of domain switching at electric fields of 170 kV/cm at 10 Hz frequency.

Hexagonal single crystals of $[(CH_2CH_3)_4N][FeBrCl_3]$ (up to 10 mm in length) were measured to have a piezoelectric response with a d_{33} of -7/7 pC/N. This was particularly interesting

because this value is approximately double that of the isostructural aluminum nitride which has great commercial significance as signal filters and antenna in wireless data transfer.

The solid solution compositions showed dielectric behavior in the polarization – electric field loops with no sign of hysteresis that could indicate ferroelectric switching. The materials did not undergo dielectric breakdown at electric fields up to 340 kV/cm and also had low leakage currents ($5.8 \cdot 10^{-4}$ $\mu A/cm^2$). Dielectric spectroscopy from 0.05 to 10^6 Hz at room temperature revealed a similar behavior for all samples, with a real permittivity ε' of approximately 15 – 30. Mesophase transition temperatures were confirmed from temperature dependent dielectric measurements and the lack of frequency dependence of this transition indicated that it behaved like a first order transition similar to a ferroelectric Curie transition.

The material system shows promise as a low temperature plastically formable ferroelectric and piezoelectric, but limited solubility of the organic cations caused phase separation. As a result, further investigation of the system at compositions with less than 10 mol% substitution is necessary to see if the ferroelectric and piezoelectric properties can be enhanced.

Zusammenfassung

Durch die zunehmende Nachfrage nach funktionellen Materialien in den letzten Jahrzehnten verschrieben sich immer mehr Wissenschaftler dem Ziel, Materialien mit niedrigen Produktionskosten und umweltfreundlichen Herstellungsmethoden zu finden und gleichzeitig hochspezialisierte elektrische Eigenschaften, wie piezo-, ferro- und dielektrische Merkmale zu wahren. Eine neue Gruppe plastischer molekularer Ferroelektrika, basierend auf Tetramethylammonium-Bromotrichloroferrat(III) ($[(CH_3)_4N][FeBrCl_3]$), wurde als Alternative zu aktuell verbreiteten keramischen Metall-Oxiden untersucht. Das Potenzial zusätzlicher und verbesserter Eigenschaften wurde ermittelt indem organische Tetramethylammonium-Kationen kontinuierlich durch Tetraethylammonium-Kationen ($[(CH_2CH_3)_4N]^+$) bis zu 100 % ersetzt wurden, wobei die komplette Mischung mit Hilfe von Kristallisation durch Verdunstung bei niedrigen Temperaturen in Wasser untersucht wurde.

Das resultierende $[(CH_2CH_3)_4N]_x[(CH_3)_4N]_{1-x}[FeBrCl_3]$ (x = 0 – 1) System kristallisiert in zwei Kristallstrukturen, *Amm2* (orthorhombisch) und *P6₃mc* (hexagonal) bei Raumtemperatur. Diese Raumgruppen gehören zu den reinen Verbindungen des Systems, $[(CH_3)_4N][FeBrCl_3]$ und $[(CH_2CH_3)_4N][FeBrCl_3]$. Eingeschränkte Löslichkeit der ersetzten organischen Kationen in der gegenteiligen Struktur wurde beobachtet, indem Änderungen der Gitterparameter und

Phasenverhältnisse als Funktion der Zusammensetzung verfolgt wurden, basierend auf Strukturanpassungen von Pulver-Röntgendiffraktogrammen mit Rietveld-Verfeinerung. Das genaue Verhältnis der Phasen in der metastabilen festen Lösung und die Löslichkeit der ersetzten Kationen, genauso wie die Morphologie der Kristalle, die mit Rasterelektronenmikroskopie untersucht wurden, hängen von der Kristallisationsrate, der Polarität des Lösungsmittels und der thermischen Vergangenheit des Materials ab. Dynamische Differenzkalorimetrie (DSC) zeigte, dass alle Kompositionen eine plastische Mesophase haben, mit einer Übergangstemperatur von 100 – 150 °C. Diese Mesophase erlaubt plastische Verformung der Kristalle bei niedrigen Temperaturen und eröffnet damit Möglichkeiten, unkompliziert und billig komplexe Bauteile herzustellen.

Polykristalline Scheiben mit einer Dicke von 250 – 450 µm wurden durch Heißpressen von Kristallen produziert und dann für elektrische Messungen verwendet. Ferroelektrische Eigenschaften von $[(CH_3)_4N][FeBrCl_3]$ wurden bestätigt, zusammen mit einer hohen gerichteten Verformung (0.109 %) und einem piezoelektrischen d_{33}-Wert von -7/7 pC/N, gemessen mit einem Berlincourt Piezometer. Die Untersuchung der kinetischen Wechsel der ferroelektrischen Domänen ergab eine Sättigung der möglichen Schaltungen bei elektrischen Feldern von 170 kV/cm bei einer Frequenz von 10 Hz.

Hexagonale Einkristalle aus $[(CH_2CH_3)_4N][FeBrCl_3]$ (mit bis zu 10 mm Länge) hatten eine piezoelektrischen d_{33}-Wert von -7/7 pC/N. Dies ist insbesondere interessant, weil sie in etwa dem doppelten Wert von isostrukturellem Aluminiumnitrid entspricht, ein Material mit großer kommerzieller Wichtigkeit als Signalfilter und Antenne für den drahtlosen Datenverkehr.

Die verschiedenen gemischten Kompositionen der festen Lösung zeigten dielektrische Eigenschaften wenn die Polarisierung gegen das angelegte elektrische Feld aufgetragen wurde, ohne einem Anzeichen von Hysteresis, welches auf ferroelektrisches Verhalten deuten könnte. Die Materialien hielten elektrischen Feldern von bis zu 340 kV/cm stand und wiesen einen geringen Leckstrom ($5 \cdot 10^{-4}$ µA/cm^2) auf. Dielektrische Spektroskopie von 0.05 bis 10^6 Hz bei Raumtemperatur ergab ein einheitliches Bild für alle Kompositionen, mit einer realen Permittivität ε' von ungefähr 15 – 30. Die Übergangstemperaturen in die Mesophase wurden mit Hilfe von temperaturabhängigen dielektrischen Messungen bestätigt und die Abwesenheit der Frequenzabhängigkeit deutet auf einen Phasenübergang erster Ordnung, ähnlich einem ferroelektrischem Curie-Übergang, hin.

Das Materialsystem hat Potential zu einem einsatzfähigen Ferroelektrikum und Piezoelektrikum, das bei niedrigen Temperaturen plastisch verformbar ist. Eingeschränkte Löslichkeit der organischen Kationen resultieren in Phasentrennung, weshalb weitere Untersuchungen angestellt werden müssen, die Komposition mit weniger als 10 mol% der Minderheitskomponente beinhalten um herauszufinden, ob sich die ferro- und piezoelektrischen Eigenschaften damit ändern.

2. Introduction and motivation

Materials for electrical applications are in huge demand in our modern society. No matter the application, energy consumption, miniaturization and more environmentally friendly production processes are just a few of the attributes that newly developed materials should have. In addition to others, new ferroelectrics, piezoelectrics and dielectrics are among the most sought-after material classes because of their wide range of applications. Multilayer capacitors, being the largest application for ferroelectrics, is a multi-billion-dollar industry that is expected to grow in the upcoming years. They are essential components in modern technologies from frequency filters in mobile phones, to ultrasound transducers in medical imaging.[1] These materials will have growing importance in future technologies as we move towards a more connected and digital world.

Nowadays, commercially available ferroelectrics are usually ceramic metal oxides, made from barium titanate ($BaTiO_3$) or lead zirconate titanate ($PbZrTiO_3$). These materials require high synthesizing temperatures, contain toxic elements such as lead, are difficult or impossible to recycle and are brittle and mechanically stiff. They are often doped with rare elements such as lanthanum and niobium.[2,3] This makes them less than ideal for a sustainable future as well as many possible future applications. As a result, we need to look to new material alternatives to fulfill the growing need for high performance electronics, produced in an environmentally friendly way.

Meeting all these different challenges in a single material requires multifunctional properties, careful consideration of the chemicals used and ingenuity in the synthesis chosen. Supramolecular materials present themselves as promising candidates since they make it easy to combine multiple attributes in one material. They consist of molecules, arranged in the regular positions of a crystal lattice that is held together by weak hydrogen or Van-der-Waals forces. By requiring lower synthesizing temperatures and fewer critical elements, they may prove to be sustainable material alternatives in a number of different applications. They can be designed on a molecular level to be deformable like a thermoplastic above a certain temperature, giving them the term plastic crystal. Some of these compounds have been found to have interesting electrical properties, including piezo- and ferroelectricity.

This new and emerging field of plastic crystal ferroelectrics has only recently reached some attention, and little is known about how to control and tune the functional properties. A very simple and elegant approach to tailor properties of a material is to make a solid solution,

comprising of two or more molecular species with different properties. Many variables, from the ratio of molecular species to the synthesizing method can influence the outcome but ideally, the different molecular species are homogeneously distributed among the lattice sites.[4] In an ordered crystal lattice, the major structure may be determined by the majority components of the composition, with the other one either occupying interstitial sites or replacing one of the original molecules of the lattice. It is also possible to form totally new crystal structures that are not native to either of the end compositions of the system. In addition to a gradual change of the properties with the ratio of components used, morphotropic phase boundaries (MPB's) can exist at the border of two crystal structures. That is, a structural transition as a function of composition that is nearly independent of temperature. Close to this phase transition, specific properties change dramatically. This is a phenomenon widely studied in metal oxide ferroelectrics and therefore is an excellent approach for engineering new ferroelectric materials.[5]

The concept of solid solution compositional engineering has not yet been thoroughly explored in the search for plastic crystal ferroelectrics, with research mostly focusing on specific compositions and their properties. $[(CH_3)_4N][FeBrCl_3]$ is a promising candidate for a more sustainable and easy-to-manufacture ferroelectric that has been gaining some attention recently.[6] Some other studies have been conducted on a similar material, $[(CH_2CH_3)_4N][FeBrCl_3]$ which has similar mechanical properties and a crystal structure that could induce piezoelectric strain.[7–9] Their chemical similarity make them great candidates to perform an investigation of the $[(CH_3)_4N][FeBrCl_3]$ - $[(CH_2CH_3)_4N][FeBrCl_3]$ solid solution system, in hopes of tuning the respective properties.

Previous studies that focused on compositional changes of the $[(CH_3)_4N][FeBrCl_3]$-family usually focused on altering the anion, either by varying the ratio of Bromide to Chloride or by using different tetrahedral metal-halide or metal-oxide species.[10] Research suggests that the structural changes arising from these variations do not promote any significant change in the properties of the material. Manipulating the cation, on the other hand, could induce all kinds of structural changes, resulting in new mechanical and electrical properties.

$[(CH_3)_4N][FeBrCl_3]$ is an organic-inorganic molecular ferroelectric in which the electric properties arise from a displacement of molecules rather than atoms. In contrast to ceramics, this material exhibits a so-called mesophase of a cubic crystal structure in between the liquid and solid phase, making it a plastic crystal. This means that parts made from this material can

be shaped at much lower temperatures. This process can even be repeated several times, something that is not possible with sintered ceramics. $[(CH_3)_4N][FeBrCl_3]$ displays distinctive multiaxial ferroelectric behavior, owing to the multiple allowable polarization directions in the polar crystal structure (*Amm2*) at room temperature. Contrary to uniaxial ferroelectrics, the multiaxial ferroelectrics are not limited to the 180° domain switching and thus can be manufactured as polycrystalline materials and then polarized so that the polarization vectors are approximately aligned in a single macroscopic polarization direction.[6] Large strain values can be obtained when applying an electric field, going up to around 0.1 %.

Research has been conducted on $[(CH_2CH_3)_4N][FeBrCl_3]$, also showing a plastic mesophase in between the solid and liquid state at temperatures above 100 °C. The stable crystal structure at room temperature is *P6₃mc*, where each $[(CH_2CH_3)_4N]^+$-cation is tetrahedrally coordinated by four $[FeBrCl_3]^-$-anions. Not having any mirror planes perpendicular the c-axis, this structure is polar and has a piezoelectric coefficient of approximately 6 pC/N that can be observed on single crystals. This number is comparable and even larger than that of other commercially significant wurtzite structured piezoelectric materials such as aluminum nitride (AlN), gallium nitride (GaN) and zinc oxide (ZnO).[11,12] Multiple phase transitions occur below and above room temperature, mainly owed to the size of the cation with its flexible alkyl-chains.[7,8] Studies have shown that it is possible to grow large single crystals, synthesized through slow evaporation of aqueous solutions.

2.1. Objective

Having a promising set of mechanical and electrochemical properties that could possibly be further enhanced and manipulated, the $[(CH_3)_4N][FeBrCl_3]$ - $[(CH_2CH_3)_4N][FeBrCl_3]$ solid solution system is worth investigating more closely. This material group offers the possibility of low energy synthesis with readily available chemicals that do not pose a serious toxicological danger. Since only little work that has been done on these materials, some promising properties that can certainly be further tweaked and enhanced could be revealed. The wide variety of possibilities available through solid solution synthesis offers the potential to a whole new set of materials with interesting combinations of properties. With sustainability in mind, the experimental work focused on finding an easy and reliably synthesis route that does not require high temperatures or harmful solvents. A crystallization from aqueous solution was found to have the greatest potential, with the possibility of tweaking the properties of the final product through different crystallization parameters. The obtained samples were investigated using a range of tools to get a comprehensive overview over their general behavior.

Plastic properties, high temperature phases and purity were determined by DSC measurements. Since electrical properties depend heavily on the crystal structure, powder x-ray diffraction (powder-XRD) was performed. Scanning electron microscopy and optical microscopy were the primary tools utilized to get information about the morphology of samples, a property that was heavily influenced by the synthesis route. The electrical behavior of the samples was determined through a number of dielectric, ferroelectric and piezoelectric measurements. Combining all these measurements allowed us to get a good understanding of the material, its properties and how the physicochemical properties are influenced by the material itself.

3. Background

3.1. Crystallization from solution

Obtaining specific electrical properties from a material requires control about its crystal structure, which can most easily be achieved by a crystallization from solution. In addition to the ability of controlling crystal shape, size and size distribution, this approach also yields pure product, since a crystal grown from an imperfect solution will automatically have less impurities. Crystallization itself is the solidification of a homogeneous particle in which the constituents are arranged periodically and can occur from melts, solutions and vapors. To achieve crystallization from a solution supersaturation is necessary, both for the nucleation and growth of crystals. Nucleation occurs when small numbers of ions, atoms or molecules arrange until they have sufficient excess surface energy to form a new phase. This is initialized by mechanical impact, seed crystals, foreign nuclei, the walls of the container or varieties in the concentration, caused by inhomogeneous stirring, surface evaporation or temperature gradients. Crystal growth can be understood as a combination of diffusion of the solute and a surface reaction. If they are both energetically favored, the solid will grow from the solution, with the main driving force being supersaturation. Many parameters like temperature, impurities, agitation and solvent determine the nucleation and crystallization rate as well as the ratio of the two.[13] Due to an increasing need for advanced materials with very defined characteristics, the field of “crystal engineering” has seen a rapid increase in popularity in recent years. Many physicochemical attributes can be explained by stochiometric composition and structure. Both of these properties, as well as many others can be manipulated by working with a system consisting of a solid solution. This approach allows for the continual fine-tuning of specific properties, such as chemical stability, piezoelectricity, photochromism and hardness as well as developing a whole new set of combination of properties.

One of the basic principles, Vagard's law, has long been known to exist for metal alloys but also applies to molecular crystals. The lattice parameters of a crystal change linearly with the number of substituted sites, at least for small changes. In other instances, the crystal structure can change in a discontinuous way, resulting in a jump of conductivity or para-/ferromagnetic states. The mixed crystal can also force the material in a structure different from both parent components.[4]

3.2. Solubility in the $[(CH_2CH_3)_4N][FeBrCl_3]$ - $[(CH_3)_4N][FeBrCl_3]$-system

While both $[(CH_2CH_3)_4N][FeBrCl_3]$ and $[(CH_3)_4N][FeBrCl_3]$ seem very similar at first, some key properties differentiate them from each other. This is caused by their different crystal structures at room temperature. When being crystallized from solution, the individual ions are homogeneously mixed. Since the anion is the same in both compositions and the cations have the same charge, the crystallization of a solid solution in which one of the species determines the crystal structure is quite likely. The ionic radii of the $[(CH_2CH_3)_4N]^+$- and $[(CH_3)_4N]^+$-cation are 3.85 and 3.22 Å, respectively.[14] Considering this, it is more likely that a substitutional solid solution is formed, meaning that sites in the lattice are replaced by the minority cation. The ethyl-chains of the $[(CH_2CH_3)_4N]^+$-cation have some degree of flexibility, allowing it to fit into the smaller lattice positions of the $[(CH_3)_4N]^+$-structure, making it hard to predict whether or when a solubility limit is reached. Phase transition temperatures and solubility are similar, making the formation of a solid solution reasonable. Assuming that a sample crystallizes in a single structure, there comes a point of the minority cation at which the transition to the other crystal phase becomes more energetically stable. This region around the phase transition between two different solid crystals has been studied at length and is known as a morphotropic phase boundary (MPB).

A morphotropic phase boundary is a phenomenon that has been studied in the past to improve physical properties of a material. When combining two materials which can form a solid solution there is a phase transition from one phase A, enriched with B to phase B, enriched with A. At this point, there is a non-linear increase in multiple physical properties, which can be utilized to design materials with very defined and enhanced properties. This phase transition is approximately independent of temperature, meaning that it is depicted as a vertical line in a temperature-composition phase diagram.[15] No research has been conducted on the phase diagram of the $[(CH_2CH_3)_4N][FeBrCl_3]$ and $[(CH_3)_4N][FeBrCl_3]$ system. Since the two end-members of the system are only different in the length of their alkyl-chains, there is a possibility of them forming a solid solution, at least across a portion of the composition range. In case

there is solubility of one of the cations in the lattice of the other phase, there will be a saturation limit at which place a miscibility gap or a morphotropic phase boundary occurs. Since ferroelectric and piezoelectric properties are impacted significantly my minority phases and impurities, clean, homogenous and dry samples are required to expect reliable measurements.

3.3. Plastic crystals

The plastic phase is a mesophase, that is a hybrid phase in between the solid and the liquid state of a material, as seen in Figure 1.

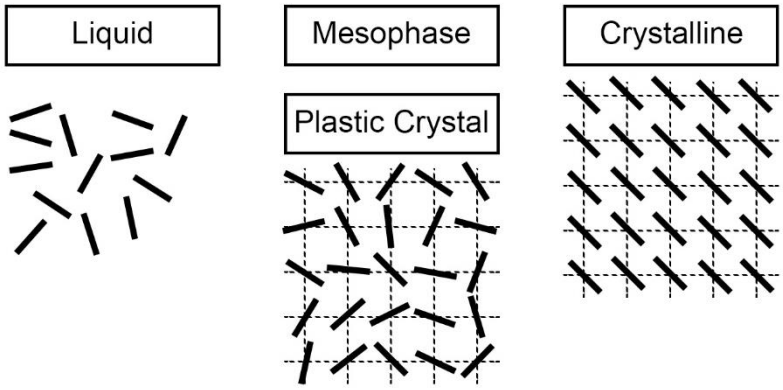

Figure 1: Visualization of the freedom of movement of molecules within different phases.

Long range order and a specific crystallographic point and space group based on the crystal symmetry are present, on the basis of the centre of mass of the individual ions. Therefore, the compound as a whole behaves like a solid. The molecules themselves have a lot of rotational freedom, which is more likely with molecules that possess an approximately globular structure. This phenomenon allows for the migration of lattice defects, which is the reason why these materials are plastically deformable, unlike traditional, brittle crystals. Additionally, the volume occupied by rotating molecules exceeds the values of similarly shaped, but rigid structures, resulting in weaker and more isotropic bonding and therefore higher deformability. Typical crystal structures of plastic crystals belong to the highly symmetric cubic crystal system, a result of the spherical shape of the molecular building blocks. Most of these materials have a defined and fully rigid crystal structure at lower temperatures. The plastic phase, with its short-range disorder is only reached via one or multiple solid-solid phase transitions, before reaching the liquid phase. This also explains the low entropy of melting typical for plastic crystals. When heated up to the plastic phase and then mechanically deformed, the material exhibits deformation without breaking.[6] A wide range of ions or ionic molecules can be used to produce these kinds of crystals, accounting for the vast number of possible properties, such

as ion conductivity or ferroelectricity. Plastic properties are highly desired in electronic devices, because they eliminate the problem of poor contact between electrodes and electrolyte upon volume changes due to thermal expansion or chemical reactions and easier manufacturing of parts.[16]

3.4. Introduction to selected electrical properties

Many electromechanical properties are in some ways or another a result of the structure of a material. From the basic principles of electrical conductivity in metals because of their bond structure to the permittivity, which is determined by the crystal structure of a material. Based on the nature of the materials studied in this project, dielectric behavior, piezoelectricity and ferroelectricity are discussed in more detail below.

3.4.1. Electric Polarization

The underlying concept resulting for pyro-, ferro- and piezoelectric properties of materials is their response to a change in temperature, an external electrical field or mechanical stress. When being inserted into a field, electrons and nuclei within a bulk material rearrange, forming dipoles, or existing molecular dipoles orient themselves along the lines of the field. One can distinguish between electronic, ionic and orientation polarization and effects caused by heterogeneity at grain boundaries. When an electric field is present, any material within the field lines displays a shift of the electron cloud relative to the nucleus. This effect might be very small, and only lasts as long as the field is applied. Ionic polarization can be found in materials with ions organized in a crystal lattice. In an electric field, the anions and cations are moved from their rest position, therefore creating dipoles. Orientation polarization is only present in materials with permanent dipoles, which reorient themselves if a field is applied. Depending on the type of polarization and the specific properties of the material, the relaxation frequency determines the maximum frequency of the applied field that can be used to induce the effect. This is the time it takes for a polarized sample to return to its unpoled ground state.[17]

3.4.2. Dielectric Materials

Any material that is inserted into an electric field shows some kind of dielectric response, but only some have an effect large enough to be functional as dielectric materials. For this to work the material must be electrically insulating. Dielectrics with permanent dipoles are not polarized as long as there is no external electric field. All dipoles are randomly oriented, cancelling each other out. Upon application of a field, the dipoles align along the lines of the electric field, therefore producing a macroscopically measurable polarization. In non-polar dielectrics, the dipoles are generated once an electric field is applied by displacing ions within

a crystal structure or by distorting the electron positions around the nuclei of atoms. A very common application of dielectrics is the use in capacitors. A high dielectric constant allows a material to store more charge per volume, making high dielectric materials such as $BaTiO_3$ effective millimeter and micrometer sized capacitors, a market now worth $6 billion (USD) annually.[1,17] Other devices include LCD-screens and semiconductors.

3.4.3. Ferroelectricity

Ferroelectricity is a well-studied and understood phenomenon which is used in many applications ranging from capacitors to memory devices. The basic attribute of a crystal to have ferroelectric properties is a non-centrosymmetric (acentric) point-group. 11 of the 32 crystal classes have a centre of symmetry which means they are not polar and do not possess specific electrical properties. Having a center of symmetry means that there is an inversion operation for every atom of the unit cell. 20 of the remaining 21 point-groups display charge separation on the faces of the crystal when a stress is applied, because they are acentric. This effect is called direct piezoelectricity, a linear material property that can also be used to physically deform a crystal by exposing it to an electric field (converse piezoelectric effect).[18] 10 of these 20 non-centrosymmetric classes have an unique polar axis, meaning that there are two points that are unmoved by all symmetry operations. These polar point groups exhibit spontaneous polarization along that axis. Since this effect is temperature dependent, the flow of charges on the surface can be measured with changes in temperature. This is an effect of the change in dipole moment caused by the change in temperature or stress. These 10 polar classes are therefore called pyroelectric classes. If a material exhibits electric polarization even after the electric field is turned off it is called ferroelectric. The structure of $PbTiO_3$, a typical ferroelectric material, is displayed in Figure 2. The crystal can change between two or more orientational states while maintaining the same crystal structure. The polarization of a ferroelectric does not change linearly with the applied electric field, which results in a characteristic hysteresis loop, as seen in Figure 3.

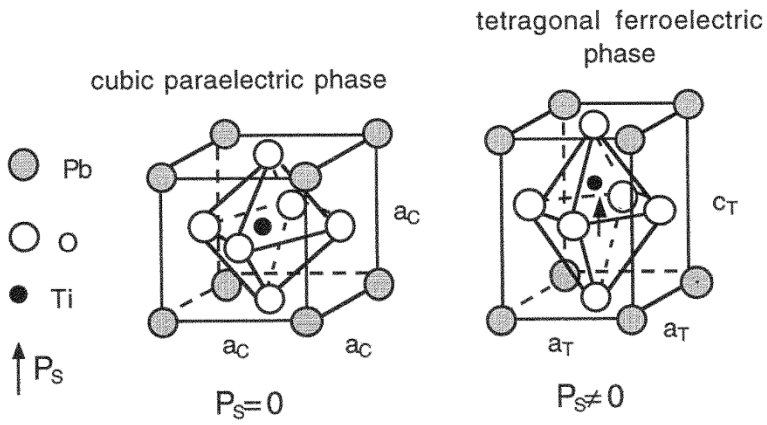

Figure 2: $PbTiO_3$, which has a perovskite ABO_3 structure, has a cubic paraelectric and a tetragonal ferroelectric phase.[19]

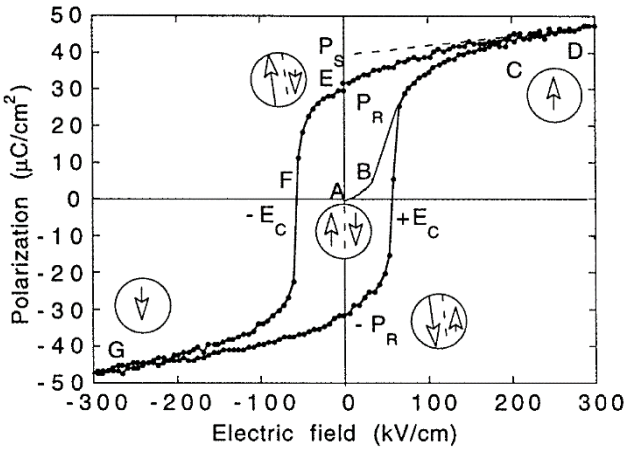

Figure 3: Experimental polarization – electric field (P-E) loop, with the arrows showcasing the orientation of the polarization state. The loop was measured on a (111)-oriented 1.3 µm thick sol-gel $Pb(Zr_{0.45}Ti_{0.55})O_3$ film. (Experimental data courtesy of D.V. Taylor)[19]

When starting from point A, an increase in the applied field results in a linear increase to point B in the dielectric polarization and no domain switching occurs. At a certain field, domain switching causes a rapid increase in the polarization, which continues until switching saturation occurs and the polarization levels off at point C. The polarization increases linearly at even higher fields, but all domains are aligned and oriented. When the applied field is removed, the polarization decreases because not all domains stay perfectly aligned after an initial linear loss. The polarization at the point where the electric field is zero is called remanent polarization P_r. Applying a field in the other direction causes the domains to switch into the opposite direction, but with a large hysteresis. The point at which the field is strong enough to remove all the polarization (point F) is called coercive field (E_c). The hysteresis loop is symmetrical, and the same procedure happens in the other direction.

In most ferroelectrics, the highest symmetry phase which still results in polarization is called prototype phase. The spontaneous polarization usually decreases with increasing temperature, up to the Curie point T_c. There are some known examples of ferroelectrics with increasing polarity as a function of increasing temperature. Without an external electric field, the different orientations of the polarization cancel each other out, resulting in an overall unpolarized material. Small volumes with the same polarization are called domains. They can be categorized according to which crystallographically allowable polarization direction they possess with respect to adjacent domains.[20] Perhaps the most important distinction between different domains is that of ferroelectric (180°) and ferroelastic (non-180°), as when switched by an external electric field the former contributes only to the polarization response of a material while the latter contributes to both the polarization and strain. The name "ferroelectric" derives from its similar properties to ferromagnetic materials, even though ferrous materials do not play a particularly important role in ferroelectrics. The crystal structure of all ferroelectrics contains a permanent dipole. All ferroelectrics are also piezoelectric.[21] Despite large numbers of studies on ferroelectric materials, only few of them focus on the properties of plastic crystals. More research is needed to investigate the fundamental behavior and underlying mechanisms of these new ferroelectric materials.

3.4.3.1. Challenges of organic and molecular ferroelectrics

Even though large numbers of organic or hybrid organic crystals have been synthesized, only a small portion of them are considered to be ferroelectric.[22] A highly common system depicting ferroelectricity in inorganic solids is a lattice consisting of permanent dipoles. This spontaneous polarization can be reoriented when an external field is applied, producing macroscopic ferroelectric behaviour. The switch from para- to ferroelectric state is called a disorder-order transition. Some prominent examples include metal oxides such as $Pb[Zr_xTi_{1-x}]O_3$, $BaTiO_3$, $PbTiO_3$. Some organic materials show similar structures, like the polymer PVDF (poly(vinylidene difluoride)) or Thiourea. It forms a molecular crystal which has ferroelectric properties at low temperatures.[23] The TEMPO (2,2,6,6-tetramethyl-1-piperidinyloxy) free radical is an organic ferroelectric at room temperature, because of its polar molecules. Only few other low-molecular organic materials have been found with ferroelectric behaviour, due to multiple reasons. The polar dipoles often cancel each other out, producing an overall paraelectric material. Additionally, the energy barrier necessary to switch the orientation of the molecules in the lattice needs to be low. This is a challenge for polymers, in which the steric hinderance of reorientation leads to large coercive fields.

3.4.4. Piezoelectricity

The Greek word *piezo*, meaning "pressure" is used to describe this electromechanical effect that can be found in many organic and inorganic materials. J. Curie and P. Curie first described this effect in 1880 when they discovered a linear relationship between mechanical stress and strain on one hand and electric field and displacement on the other. When a pressure is applied to a piezoelectric, electricity is generated, resulting in the direct piezoelectric effect. The converse piezoelectric effect describes the deformation of a material when a voltage is applied. Applications of this effect include electromechanical transducers, ultrasonic generators, radio frequency and microwave filters, sensors and actuators.[24]

Without applying pressure, positive and negative charges within a single crystal lattice are organized in a way that the material as a whole in uncharged. The same goes for a material consisting of permanent dipoles, for example a molecular crystal. They are organized as domains, with specific allowable polarization directions of the same crystal structure. Dipoles within one domain are aligned, but different domains can have different orientations so that there is no net polarization on a macroscopic level. For this reason, for a polycrystalline piezoelectric material to be technologically useful it must be either textured so that different grains and domains have approximately the same orientation, or it must be ferroelectric, so that the domains can be reoriented after the material is synthesized. Mechanical deformation of a piezoelectric unit cell causes the atomic positions to shift slightly, inducing dipoles and a disassociation of the centers of positive and negative charge. This results in a polarization of the structure, because the sum of the positive and negative charges does not coincide anymore. The same goes for the dipoles, where the domains align in one direction when a field is applied. In an ordered lattice, neighbouring opposite polarized units cancel each other out, except on the surface, where charges appear. The resulting electric field is the transformation from mechanical to electrical energy. In polycrystalline materials, there are grains with different crystallographic orientations. The domains within these grains cannot be completely aligned through polarization, resulting in a piezoelectric effect of zero.

Piezoelectric materials are inherently anisotropic because the polarization only works along specific axis of the crystal lattice and domains. Therefore, it is very important to determine the axis along which the polarization has the biggest effect on the material.

For practical applications, the piezoelectric material is usually poled, resulting in a net polarization even after the electric field is turned off. This behavior is inherent to ferroelectrics, meaning only they can be poled. Along with that, the material also experiences a change in

dimensions, more specifically an elongation between the electrodes of the applied poling voltage and shrinkage perpendicular to that axis. The material changes its dimensions and polarity whenever an external voltage smaller than the poling voltage is applied. It elongates further, if the polarity is the same as the poling voltage and shrinks if it is opposite. The polarization and the strain of the material follow the P-E and S-E curves, respectively. In reverse piezoelectric effect can also be observed, resulting in a charge if the material is exposed to compressive or tensile loads. Depending on the material, the change in the dimensions might result in an overall change of the volume. Sometimes tough, the expansion and contraction cancel each other out, resulting in a net volume change of zero.[17]

The piezoelectric charge coefficient d_{ij} is one of the key parameters used to quantitatively categorize piezoelectric materials. It is defined as the strain produced when applying a certain charge, or vice versa. The anisotropic properties of poled ferroelectrics need to be taken into account. Conventionally, poled axis is denoted as the 3-axis (z), with the 1- and 2-axes being perpendicular. The d_{33}-coefficient is therefore measured along the poled axis.[25]

Piezoelectrics have a wide variety of applications, ranging from actuators and sensors to medical applications and possible energy harvesting possibilities is the future. The spark in a gas lighter results from a piezoelectric crystal that is compressed and produces a charge.[26] Quartz watches exploit the piezoelectric properties of α-quartz to measure the time.

3.4.5. Application

Ferroelectric materials can be used for memory storage since their induced polarization state remains stable over time and can be reversed or removed with an electric field, making them capable of ternary bit memory, holding a 1, 0 or -1 state. They are also used in capacitors, because many metal oxide ferroelectrics also exhibit high dielectric constants (relative permittivity), the largest commercial use being $BaTiO_3$ in multilayer ceramic capacitors (MLCCs).[1,27] The piezoelectric effect is widely exploited in sensors and actuators where mechanical stress is transferred into electricity (direct piezoelectric effect) and vice versa (the converse piezoelectric effect). Piezoelectrics based on the PMN-PT ($Pb(Mg_{1/3}Nb_{2/}3)O3$-$PbTiO_3$) system could dramatically revolutionize medical imaging[28] while AlN is being used in smartphones as a high-performance acoustic filter.[29] Infra-red detectors use the pyroelectric effect. By doping ferroelectrics with electron donors, one can achieve a semiconductor that has a large change in resistivity when being heating past the Curie-temperature. The positive temperature coefficient of resistance (PTCR) is used in devices to prevent overheating.

3.5. Similarities and differences between $[(CH_2CH_3)_4N][FeBrCl_3]$ and $[(CH_3)_4N][FeBrCl_3]$

A big advantage of the investigated system is the similarity of the chemical footprint of the two pure components, $[(CH_2CH_3)_4N][FeBrCl_3]$ and $[(CH_3)_4N][FeBrCl_3]$. By synthesizing solid solutions of these two compounds, no additional elements are introduced into the material. Compared to other methods for tailoring the properties of conventional metal oxide ferroelectrics, such as doping with additional elements, this route does not increase the number of elements used and thus makes reusing and recycling parts a lot easier and keeps the environmental footprint small. Previous studies on both $[(CH_2CH_3)_4N][FeBrCl_3]$ and $[(CH_3)_4N][FeBrCl_3]$ have shown that the size of the cation has a big impact on the physicochemical properties. Molecular kinetics, such as the dynamic rotation of the cation, as well as the size difference between cation and anion or the charge distribution in the cation cause $[(CH_2CH_3)_4N][FeBrCl_3]$ to crystallize in a different crystallographic structure at room temperature. This has a direct influence on the properties.

3.6. Aqueous synthesis at low temperature – an ecological and economic approach

Currently the most technologically significant ferroelectric and piezoelectric materials are metal oxides and nitrides, such as $BaTiO_3$ and PZT, and most are produced as bulk ceramics. These ceramics require high manufacturing temperatures of 1000 °C or more. The raw materials also require milling prior to heat treatment to ensure a dense and homogeneous final product. These requirements result in a large energy footprint for these materials. Moreover, additional elements are often added to the compositions to tailor the properties for specific applications, resulting in a final product containing rare, costly or critical elements that are very difficult or impossible to recover at the end of the materials useful life. As a result, the electroceramics that are produced industrially today lack sustainability.[30] The plastic crystals focused on in this study, based on the $[(CH_3)_4N]_x[(CH_2CH_3)_4N]_{1-x}[FeBrCl_3]$ system can be synthesized at temperatures below 100 °C, only using water as a solvent and without any byproducts through evaporation crystallization. This type of crystal growth is used industrially on a large scale, and the production of sodium chloride and sucrose in this way accounts for over 50 % of the worldwide production of commercially utilized crystals. For polycrystalline materials, the parts are pressed at temperatures of 150 °C.

4. Experimental Methods

All samples in this study were produced by crystallization from solution before being pressed into disks that could be used for electrical measurements. A range of methods was employed to analyze the structure, thermodynamic, electrical and electromechanical properties and monitor the material at each step of the synthesis process.

4.1. Crystallization from solution

All samples presented in this work were prepared from iron(III)chloride $FeCl_3 \cdot 6H_2O$ (Sigma-Aldrich, 99 %) and either tetramethylammonium bromide $[(CH_3)_4N]Br$ (Sigma-Aldrich, 98 %), tetraethylammonium bromide $[(CH_2CH_3)_4N]Br$ (Sigma-Aldrich, 99 %) or a combination of both. 11 different compositions were produced, $[(CH_2CH_3)_4N][FeBrCl_3]$, $[(CH_3)_4N][FeBrCl_3]$ and $[(CH_2CH_3)_4N]_x[(CH_3)_4N]_{1-x}[FeBrCl_3]$ (x = 0.1, 0.2, 0.3,…0.9). The precursors were weighed out in stochiometric amounts on a Sartorius Entris® scale. The starting compounds were dissolved in different solvents (deionized water, ethanol (VWR, ≥99.8 %), methanol (Sigma-Aldrich, ≥99.8 %) and acetone (VWR, ≥99 %, technical)) before mixing the solutions.

Three different approaches were employed to achieve a crystallization from solution by evaporation. Depending on the method used, either large single crystals (0.5 to 5 mm^2) or small, powder-like crystals (<0.5 mm^2) were produced.

1. Evaporation was achieved with a hot plate set to a temperature below the boiling point of the solvent using a thermocouple. Depending on the solvent, it took about 5-8 h until all the liquid is gone. No stirrer was used to mix the solution.
2. A smaller crystal size was achieved by attaching a circular flask with the combined solutions to a rotary evaporator (Büchi Rotavapor® R-210, Büchi vacuum controller V-850, Büchi vacuum pump V-700, Büchi heating bath B-491) and removal of liquid using a heated water bath, vacuum and rotation of the flask. The evaporation process was stopped once approximately 20 vol% of the initial liquid remained in the reaction flask. The product, having a solubility, crystallized first while non-stochiometric precursors and impurities remained dissolved. The reaction mixture was vacuum filtrated through a paper filter to extract the solid product.
3. Lastly, crystals were produced by slow evaporation at room temperature. The dissolved precursors were combined in a shallow crystallizing bowl, making sure that the dilution was high enough not to promote immediate precipitation. The solutions were mixed with a magnetic stirrer for 15 minutes before letting the liquid evaporate at room temperature without agitation until all the solvent was gone, using Al-foil to cover the

mixture. Depending on the solvent and the evaporation rate, determined approximately by the number of holes in the Al-foil cover, this took up to 7 days.

Solid product obtained by each method was dried in a vacuum oven (Binder VD23) at 50 °C for at least 8 h. All samples were stored in closed glass vials in a desiccator.

4.2. Pressing of samples into disks

The synthesized samples were pressed into disks using a heated press (CARVER bench top model 3856 manually heated press). The powders were ground up using a mortar and pestle before pressing to produce a more homogeneous product. About 0.2 g of sample were deposited in between two sheets of steel (5x5 cm), covered by aluminum foil or Teflon film. The sandwich was then placed in the press, which is preheated. A pressure of 1 t was applied for 15 minutes. Without adjusting the applied force, the pressure dropped by about 0.5 t until the process was done, because of the plastic deformation of the sample. Afterwards, the sample was retrieved from the press. The edges of the samples did not densify, remained brittle and needed to be removed with tweezers, since the powders were laterally not enclosed. They were stored in plastic bags in a desiccator.

Samples were produced at temperatures ranging from 100 to 200 °C. To determine the best conditions, the samples were evaluated based on their optical appearance, thickness and mechanical stability while handling them. Based on these criteria, all mixed compositions as well as $[(CH_2CH_3)_4N][FeBrCl_3]$ were pressed at 140 °C and 1 t for 15 min while $[(CH_3)_4N][FeBrCl_3]$ was pressed at 150 °C and 1 t for 15 min. $[(CH_3)_4N][FeBrCl_3]$ was pressed at higher temperatures because of previous work done on that composition. $[(CH_3)_4N][FeBrCl_3]$, synthesized slowly, was pressed using the same conditions but without grinding the sample. Instead, a piece of agglomerated crystals of about 0.2 g was pressed directly, using Teflon foil as a liner. Aluminum foil was used for powdered samples. The thickness of samples ranged from 280 to 430 µm, measured using digital calipers. Photos of all compositions can be seen in Figure 4.

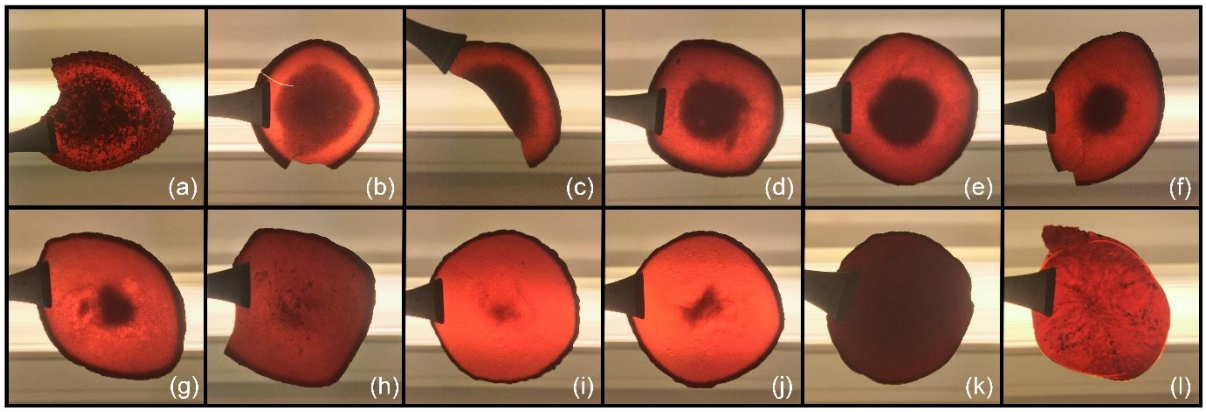

Figure 4: Photos of samples after pressing. (a) $[(CH_2CH_3)_4N][FeBrCl_3]$, (b) $[(CH_2CH_3)_4N]_{0.9}[(CH_3)_4N]_{0.1}[FeBrCl_3]$, (c) $[(CH_2CH_3)_4N]_{0.8}[(CH_3)_4N]_{0.2}[FeBrCl_3]$, (d) $[(CH_2CH_3)_4N]_{0.7}[(CH_3)_4N]_{0.3}[FeBrCl_3]$, (e) $[(CH_2CH_3)_4N]_{0.6}[(CH_3)_4N]_{0.4}[FeBrCl_3]$, (f) $[(CH_2CH_3)_4N]_{0.5}[(CH_3)_4N]_{0.5}[FeBrCl_3]$, (g) $[(CH_2CH_3)_4N]_{0.4}[(CH_3)_4N]_{0.6}[FeBrCl_3]$, (h) $[(CH_2CH_3)_4N]_{0.3}[(CH_3)_4N]_{0.7}[FeBrCl_3]$, (i) $[(CH_2CH_3)_4N]_{0.2}[(CH_3)_4N]_{0.8}[FeBrCl_3]$, (j) $[(CH_2CH_3)_4N]_{0.1}[(CH_3)_4N]_{0.9}[FeBrCl_3]$, (k) $[(CH_3)_4N][FeBrCl_3]$ fast crystallization, (l) $[(CH_3)_4N][FeBrCl_3]$ slow crystallization.

4.2.1. Electrode deposition

To prepare the samples for electrical measurements, gold electrodes were sputtered onto opposite sides of the pressed disks with a coater (Edwards Sputter Coater S150B). Argon atmosphere and a sputtering time of 45 s on each side were used. The circular electrodes were produced with masks of 3.2 mm or 4 mm diameter.

4.3. Powder X-ray diffraction (powder-XRD)

Structural analysis was performed at multiple stages of the synthesis. Using a “back-loader” sample holder, powder X-ray diffraction (powder-XRD) was performed on a Bruker D8 Focus with a Cu anode, selecting the K_α line. Samples were measured in a 2θ-range from 5° to 65° in 30 min with a 0.6 mm divergence slit. Initial analysis was performed with Bruker DIFFRAC.EVA software, before fitting the diffractograms using Bruker DIFFRAC.SUITE TOPAS software. Crystallographic Information Files (.cif) were obtained from literature and the Cambridge crystallographic data center.[6,9] The *Amm2* structure ($[(CH_3)_4N][FeBrCl_3]$) was modified by adding two bromines to the chlorine-positions with an occupancy of 0.125, while reducing the occupancy of Cl to 0.875. The structures were fitted to the obtained data using Rietveld refinement. The background functions, Lattice parameters, microstructure crystal size L and sample displacements were refined first. To further improve the fit of the model, preferred orientation analysis was performed using the Spherical Harmonics and March Dollase function.

4.4. Morphology

Optical microscopy (Bruker Alicona InfiniteFocusSL) was used to investigate the morphology of large crystals. Smaller, powder-like samples were studied using a scanning electron microscope (SEM) (Hitachi S-3400N). A piece of carbon tape was stuck to a cylindrical sample stub before depositing some of the dried crystals. The sample holder was then placed into the vacuum chamber to take SEM-images.

4.5. Differential scanning calorimetry (DSC)

Phase transition temperatures were determined by Differential Scanning Calorimetry (DSC), using a NETZSCH STA 449 F3 Jupiter device. The weight of the crucibles and samples was determined with a METTLER TOLEDO AE163 scale. 4 – 5 mg of sample were used for the measurement. A synthetic air mix at 50 ml/min was used for gas flow and nitrogen was used as a protective gas.

Reusable aluminum oxide crucibles were used for the NETZSCH STA 449 F3 Jupiter. An empty crucible was used as a reference. The temperature program starts at room temperature, heating up to 260 °C at 10 K/min, before cooling back down at the same rate. A plateau of 30 min at the maximum temperature was added. Each sample was measured at least twice back to back, investigating the effect of the thermal history.

4.6. Dielectric measurements

A dielectric analysis setup, comprising of Novocontrol Alpha-A analyzer, Novocontrol HVB 4000 high voltage test interface, Novocontrol BDS 1200 sample cell, Novocontrol ZG4 test interface, TREK MODEL 623B high voltage power amplifier and Novocontrol WinDETA software was used to measure a range of selected parameters. This was done on pressed samples with deposited electrodes, either while varying the frequency from 0.05 - 10^6 Hz or while changing the temperature from 25 - 170 °C at a limited frequency range (1000 - 10^6 Hz).

4.7. Electric field hysteresis measurements

Samples of different compositions were subjected to an external electric field while monitoring parameters like the polarization, current density and strain. This was done on an Aixacct ferroelectric test system with a TREK 10 kV amplifier and a SIOS laser interferometer. Only pressed samples with gold electrodes deposited on either side can be measured in this setup. The disks were inserted into the measuring cell and submerged in silicone oil. The frequency for all measurements was set to 10 Hz with a triangular wave form to achieve a super coercive response. All samples were measured using the same sequence of cycles, starting off with a leakage current measurement from 0 to ±10 kV/cm. These current-voltage measurements were

performed in 1 kV/cm steps on both increasing and decreasing field. Data is recorded after 1, 10, 30 and 60 seconds. Afterwards, the electric field was increased by intervals of 10 kV/cm until failure or the maximum field is reached. The current range was adjusted throughout in order to stay within the detection limits of the system. Unipolar strain loops were performed at 180 kV/cm to determine the high-field d_{33}-coefficient as well as a frequency dependent study, measuring the sample at 1, 5, 10, 50 and 100 Hz.

4.7.1. Low-field d_{33} measurements

Low-field d_{33} measurements were performed on a number of samples, both single crystals and pressed disks of different compositions. A Berlincourt piezometer (APC YE2730A) was used to measure piezoelectric coefficients with an oscillating load of 0.25 N at a frequency of 110 Hz. All samples were measured in both directions.

5. Results and discussion

5.1. Study of synthesis

5.1.1. Solubility of precursors and products

A range of solvents were considered for the crystallization of the $[(CH_2CH_3)_4N]_x[(CH_3)_4N]_{1-x}[FeBrCl_3]$-system. According to literature, multiple solvents have been used to synthesize $[(CH_3)_4N][FeBrCl_3]$, $[(CH_2CH_3)_4N][FeBrCl_3]$ and similar compositions, namely water, methanol, ethanol and acetone. [6,7,8,9,10,31,32,33,34]

Precursors and synthesized products were mixed in both room temperature and hot solvent (at the respective boiling point) and investigated visually, resulting in Table 1. 20 mg of each sample was mixed with 0.5 ml of solvent in an eprouvette. The mixture was then heated up in a water bath, if the sample did not dissolve at room temperature. The samples were categorized after visual inspection into soluble, partially soluble and insoluble.

Table 1: Solubility of precursors and products (red: insoluble, orange: partially soluble, green: soluble) in a range of cold (room temperature, 25 °C) and hot (respective boiling point) solvents.

		H_2O (cold)	H_2O (hot)	acetone (cold)	acetone (hot)	EtOH (cold)	EtOH (hot)	MeOH (cold)	MeOH (hot)
precursors	$FeCl_3 \cdot 6H_2O$								
	$[(CH_3)_4N]Br$								
	$[(CH_2CH_3)_4N]Br$								
products	$[(CH_3)_4N][FeBrCl_3]$								
	$[(CH_2CH_3)_4N][FeBrCl_3]$								
	$[(CH_2CH_3)_4N]_{0.9}[(CH_3)_4N]_{0.1}[FeBrCl_3]$								
	$[(CH_2CH_3)_4N]_{0.8}[(CH_3)_4N]_{0.2}[FeBrCl_3]$								
	$[(CH_2CH_3)_4N]_{0.7}[(CH_3)_4N]_{0.3}[FeBrCl_3]$								
	$[(CH_2CH_3)_4N]_{0.6}[(CH_3)_4N]_{0.4}[FeBrCl_3]$								
	$[(CH_2CH_3)_4N]_{0.5}[(CH_3)_4N]_{0.5}[FeBrCl_3]$								
	$[(CH_2CH_3)_4N]_{0.4}[(CH_3)_4N]_{0.6}[FeBrCl_3]$								
	$[(CH_2CH_3)_4N]_{0.3}[(CH_3)_4N]_{0.7}[FeBrCl_3]$								
	$[(CH_2CH_3)_4N]_{0.2}[(CH_3)_4N]_{0.8}[FeBrCl_3]$								
	$[(CH_2CH_3)_4N]_{0.1}[(CH_3)_4N]_{0.9}[FeBrCl_3]$								

Differences in polarity of the solvents determine the solubility of the different compounds, therefore effecting the precipitation rate and the crystal morphology.[35] $[(CH_3)_4N]Br$ and $[(CH_2CH_3)_4N]Br$ were partially soluble or insoluble in acetone, making it useless for the crystallization of a mixed crystal. $[(CH_3)_4N]Br$ did not dissolve in ethanol, making this solvent only useful for potential recrystallization. All precursors were at least partially soluble in methanol, but precipitated immediately upon mixing, because the products were only partially soluble in room temperature methanol. This crystallization was very simple and fast but provides little control over the reaction. Water dissolved both the precursors and the products easily. When using it as a solvent, the reaction could be controlled via the evaporation rate of the solvent.

Based on the preliminary solubility experiments, only water was eligible for room temperature synthesis of the whole composition range because all precursors dissolved well. Any other solvent could lead to the formation of multiphase products or not reacted precursors since their solubility was very different. Despite the possibility of dissolving precursors at elevated temperatures, the discrepancy in the solubility of the cation-precursors made the formation of a multi-phase product very likely. Therefore, water was chosen as the solvent for all

compositions containing both methyl- and ethyl-groups. When considering environmental and economic aspects of the synthesis, water is also the best choice.

5.1.2. Effect of the solvent on the morphology

The effect of the solvent on the morphology and crystal structure was investigated with SEM-imaging and powder-XRD analysis. Particular focus was given to compositions in which the solvent determines whether precipitation occurs upon mixing of the solutions or once liquid is removed through evaporation.

5.1.2.1. $[(CH_2CH_3)_4N][FeBrCl_3]$

When crystallizing $[(CH_2CH_3)_4N][FeBrCl_3]$ from diluted solutions of methanol and ethanol, fine orange particles precipitated upon mixing, because the product was insoluble in both solvents in contrast to the precursors, as seen in Table 1.

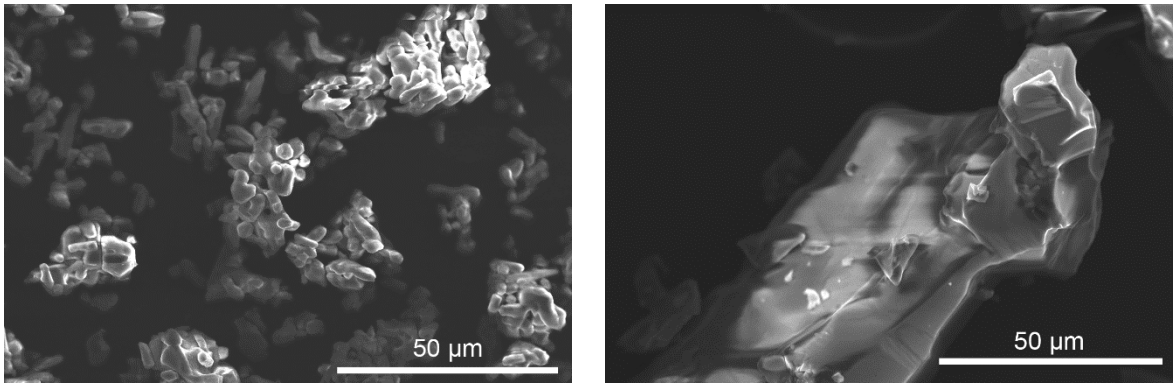

(a) (b)

Figure 5: SEM of $[(CH_2CH_3)_4N][FeBrCl_3]$, crystallized in ethanol (a) and methanol (b) after drying.

Both solvents produced irregularly shaped crystals, but with very different grain size. Using methanol promoted the growth of larger crystals, while crystals produced in ethanol agglomerated to form smaller, porous particles. Methanol, being more polar than ethanol, possibly stabilized the dissolved ions in the solutions for longer, causing fewer nucleation sites when crystallization set in. This could result in larger crystals, compared to ethanol, as seen in Figure 5. $[(CH_2CH_3)_4N][FeBrCl_3]$ was also more soluble in methanol.

Crystallization from aqueous solution occurred through evaporation of water. A fine powder was obtained that consists of irregularly shaped agglomerated crystals of different sizes. The morphology of crystals precipitated in water was similar to the other solvents, when looking at the SEM image (Figure 6). Smaller crystals agglomerated to form larger irregularly shaped particles.

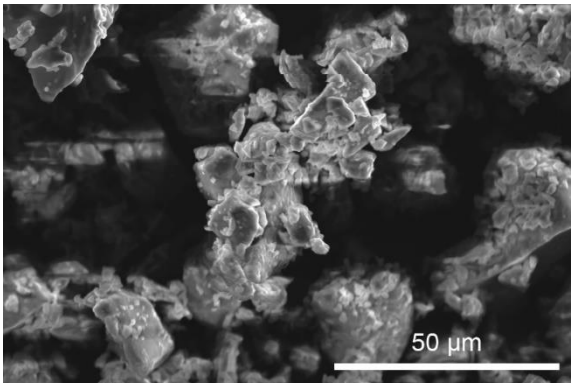

Figure 6: SEM of $[(CH_2CH_3)_4N][FeBrCl_3]$, crystallized in water after drying.

Powder X-ray diffractograms obtained from $[(CH_2CH_3)_4N][FeBrCl_3]$, produced from water, methanol or ethanol showed no differences, as seen in Figure 7. Crystal structure and purity seemed to be unaffected by the solvent used. No residues of water could be detected in the powder-XRD, indicating that the drying procedure worked sufficiently. This was aided by the precipitation as fine particles.

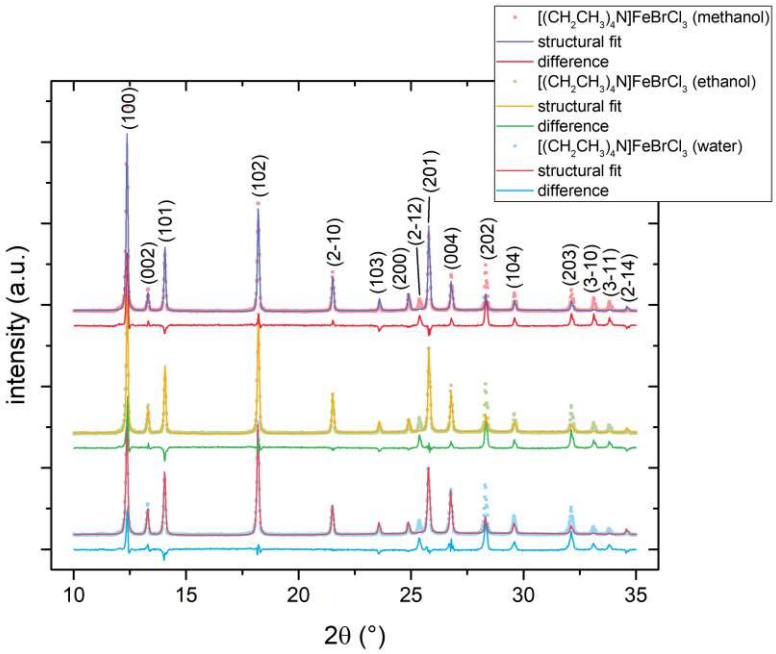

Figure 7: Powder-XRD of $[(CH_2CH_3)_4N][FeBrCl_3]$, crystallized in water, ethanol or methanol. The structural fit is based on $P6_3mc$ crystal structure profile.

5.1.2.2. $[(CH_3)_4N][FeBrCl_3]$ and $[(CH_2CH_3)_4N]_x[(CH_3)_4N]_{1-x}[FeBrCl_3]$

$[(CH_3)_4N]Br$ was insoluble or badly soluble in acetone, methanol and ethanol, therefore no study on the effect of the solvent on $[(CH_3)_4N][FeBrCl_3]$ could be performed. A similar problem arose for the solid solution of $[(CH_2CH_3)_4N]_x[(CH_3)_4N]_{1-x}[FeBrCl_3]$. Elevated

temperatures and increased amounts of methanol were necessary to perform a comparison of specific compositions.

5.1.2.3. $[(CH_2CH_3)_4N]_{0.8}[(CH_3)_4N]_{0.2}[FeBrCl_3]$

The effect of the solvent on the morphology could be clearly seen when comparing samples of $[(CH_2CH_3)_4N]_{0.8}[(CH_3)_4N]_{0.2}[FeBrCl_3]$, crystallized in water to the same composition, crystallized in methanol. Since both $[(CH_3)_4N]Br$ and product were badly soluble in methanol, an alternative synthesis route was employed. Fine needles precipitated immediately once the diluted starting solutions were combined. The mixture was heated up on a hot plate while stirring to dissolve the product again and then slowly cooled down before evaporating the liquid at room temperature over the course of several days. Needles of up to 4 cm in length and 1-2 mm in diameter were retrieved (Figure 8a). The aqueous sample was crystallized by slow evaporation of the solvent at room temperature and took several days, producing agglomerates of facetted crystals as well as some larger (up to 6 mm) single crystals (Figure 8b). This was also reflected in the powder-XRD, as seen in Figure 10.

(a) (b)

Figure 8: $[(CH_2CH_3)_4N]_{0.8}[(CH_3)_4N]_{0.2}[FeBrCl_3]$, crystallized slowly in methanol (a) and water (b).

Figure 9: Optical microscopy of $[(CH_2CH_3)_4N]_{0.8}[(CH_3)_4N]_{0.2}[FeBrCl_3]$, crystallized slowly in methanol.

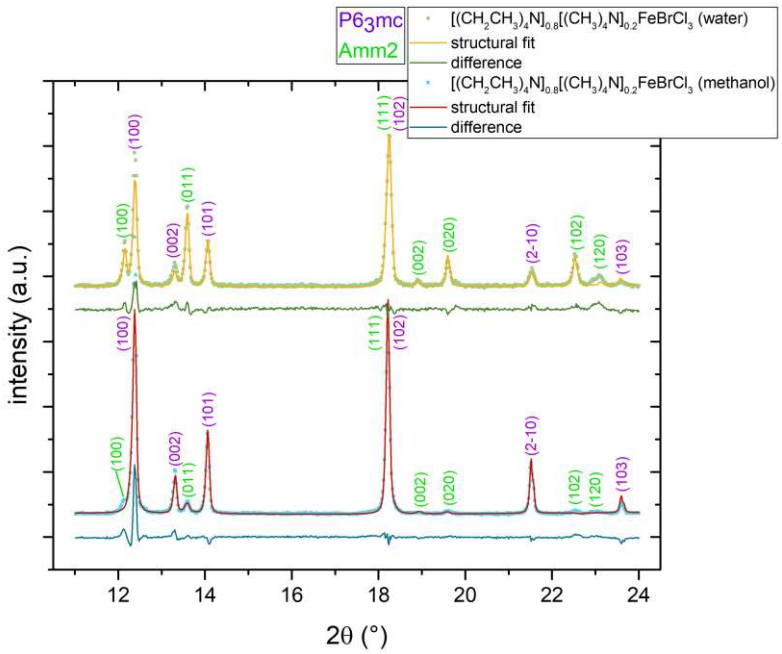

Figure 10: Powder XRD of $[(CH_2CH_3)_4N]_{0.8}[(CH_3)_4N]_{0.2}[FeBrCl_3]$, crystallized slowly in methanol and water. The structural fit is based on the $P6_3mc$ and Amm2 crystal structure profiles.

When crystallizing $[(CH_2CH_3)_4N]_{0.8}[(CH_3)_4N]_{0.2}[FeBrCl_3]$ by evaporation of the solvent, methanol was more likely to produce a solid solution, compared to water. This was visible in the powder-XRD (Figure 10), where peaks belonging to the *Amm2* minority phase were more present in the sample synthesized in water. Using methanol as a solvent, crystallization of the product set in as soon as the solutions were combined, and the thermodynamically unstable solid solution was formed (Figure 9). By choosing the right solvent and the right crystallization speed, dictated by the evaporation rate, one could fine tune the composition of the final product.

5.1.3. Effect of precursor concentration on morphology

The concentrations of the precursor solutions determine whether precipitation occurred upon mixing or not. Crystallization was promoted by evaporation, if the concentration is too low for product to form. This had potential effects on the crystallinity and morphology, as investigated on selected compositions below.

5.1.3.1. $[(CH_3)_4N][FeBrCl_3]$

The effect of the initial concentration of the precursor solutions on the morphology was investigated on $[(CH_3)_4N][FeBrCl_3]$ using water. A saturated solution (5.75 mol/L) of $[(CH_3)_4N]Br$ was prepared, as well as a saturated solution of $FeCl_3 \cdot 6H_2O$ (10 mol/L). Combining the solutions resulted in immediate precipitation of the product at room temperature.

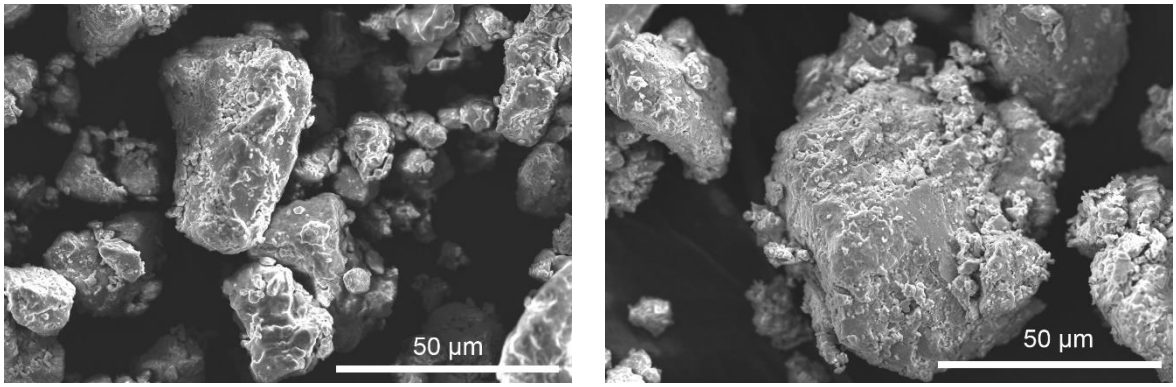

(a) (b)

Figure 11: SEM of $[(CH_3)_4N][FeBrCl_3]$ crystallized in concentrated (a) and diluted (b) aqueous solutions after drying.

This method produced fine, loose particles that could be easily dried. When conducting the same experiment using diluted concentrations ($[(CH_3)_4N]Br$ and $FeCl_3 \cdot 6H_2O$: 3.16 mol/L), precipitation set in once the solubility limit of the product was reached by evaporating the solvent. The differences in the crystal morphology between samples produced in diluted or concentrated solutions can be seen in Figure 11. The particle size of immediately precipitated samples from concentrated solutions was smaller, possibly due to a shorter nucleation stage. The crystals were of irregular, but more rounded shape, compared to $[(CH_2CH_3)_4N][FeBrCl_3]$. They appeared to have a rough surface and a wide range of crystallite sizes. Powder-XRD of crushed up particles showed a similar degree of crystallinity for both methods, as seen in Figure 12.

$[(CH_3)_4N][FeBrCl_3]$ made from diluted solutions had two small, additional peaks (13.25° and 15.96°) in the diffractogram that did not belong to the fitted structure (*Amm2*). The peak at 15.96° belonged to $[(CH_3)_4N]Br$, indicating leftover precursor in the sample. The uncontrolled and fast crystallization from concentrated solutions did not show any signs of secondary phases.

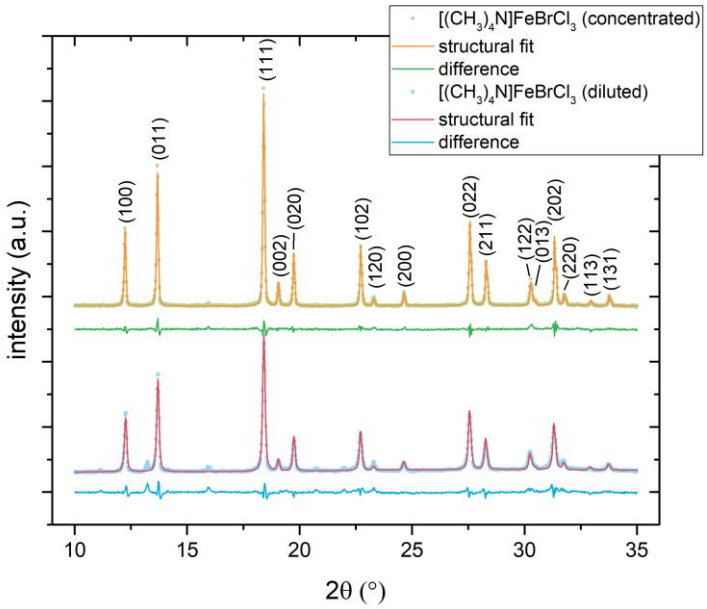

Figure 12: Powder-XRD of [$(CH_3)_4N$][$FeBrCl_3$], crystallized in concentrated and diluted aqueous solutions. The structural fit is based on the Amm2 crystal structure profile.

5.1.3.2. [$(CH_2CH_3)_4N$][$FeBrCl_3$]

Since [$(CH_2CH_3)_4N$]Br dissolved in methanol, ethanol and water, concentrated solutions of all solvents were prepared. Dissolving [$(CH_2CH_3)_4N$]Br in minimal amounts resulted in a 4.9 mol/L methanolic, 1.8 mol/L ethanolic solution and a 10 mol/L aqueous solution. When combining them with a 10 mol/L solution of $FeCl_3 \cdot 6H_2O$ in methanol, water or ethanol respectively, an immediate reaction occurred, turning the whole reaction mixture into a viscous slurry. [$(CH_2CH_3)_4N$][$FeBrCl_3$], precipitated in concentrated solutions, seemed to crystallize into very small crystals (>100 µm), which made filtration and drying difficult.

The same samples were produced in diluted concentrations using 1.4 mol/L aqueous solutions, 0.7 mol/L ethanolic and 0.54 mol/L methanolic solutions of [$(CH_2CH_3)_4N$]Br and $FeCl_3 \cdot 6H_2O$. Only the aqueous solution did not precipitate right away, because [$(CH_2CH_3)_4N$][$FeBrCl_3$] was badly soluble in methanol and insoluble in ethanol. Crystallization of the aqueous solution was promoted by evaporating the solvent. The synthesis in water, methanol and ethanol produced fine, loose particles that could easily be filtrated and dried.

Crystal shape, surface and appearance were very similar when comparing the SEM images (Figure 13) of [$(CH_2CH_3)_4N$][$FeBrCl_3$], produced in a diluted or concentrated solutions. While the size of individual crystals seemed very similar as well, agglomeration took place in the concentrated solutions. This was particularly apparent in the samples made from ethanol and

methanol, because of immediate precipitation once the precursors were combined. Small crystals did not have enough room to grow individually, stuck together and formed agglomerations, potentially trapping solvent and making drying more difficult.

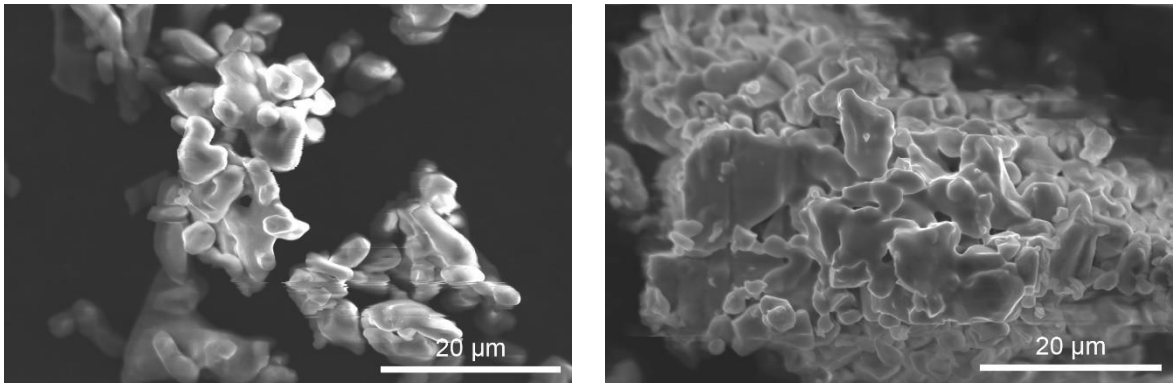

(a) (b)

Figure 13: SEM images of $[(CH_2CH_3)_4N][FeBrCl_3]$, crystallized in diluted (a) and concentrated (b) ethanolic solutions after drying.

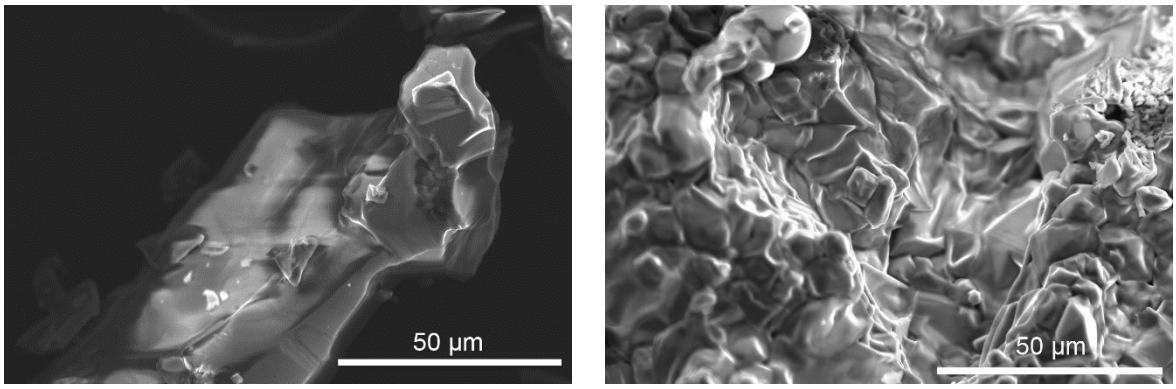

(a) (b)

Figure 14: SEM of $[(CH_2CH_3)_4N][FeBrCl_3]$, crystallized in diluted (a) and concentrated (b) methanolic solutions after drying.

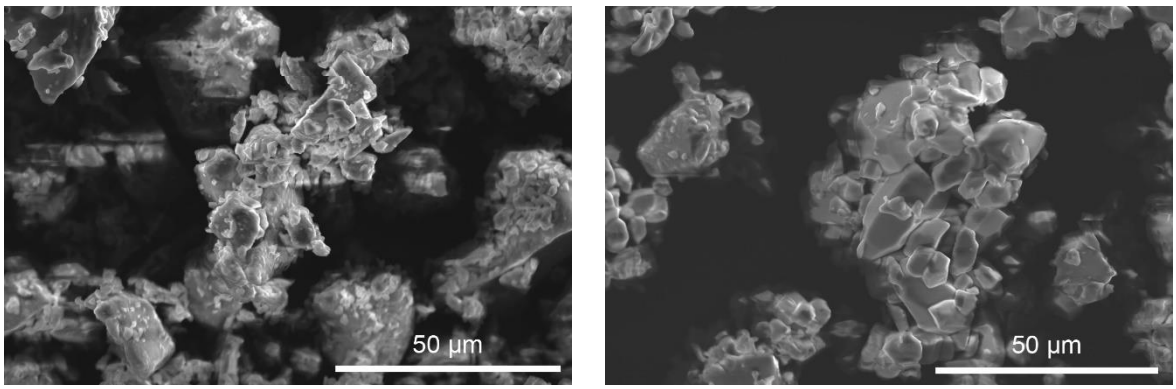

(a) (b)

Figure 15: SEM of $[(CH_2CH_3)_4N][FeBrCl_3]$, crystallized in diluted (a) and concentrated (b) aqueous solutions after drying.

5.1.4. Effect of crystallization rate on morphology

To investigate the effect of agitation and the rate of evaporation on the crystallization, a sample made from aqueous solutions was synthesized using three different methods. When using a rotary evaporator, solvent was removed quickly through the combination of vacuum and elevated temperature while spinning the reaction flask to increase mixing. The same composition was crystallized on a hot plate, set to 70 °C without stirring. Lastly, another approach was taken by evaporating the solvent at room temperature over the course of several days without agitation.

5.1.4.1. $[(CH_2CH_3)_4N][FeBrCl_3]$

The macroscopic crystal morphology of samples of $[(CH_2CH_3)_4N][FeBrCl_3]$ using a hot plate or rotary evaporator was very similar. Both methods produced fine, small particles that could easily be dried. They were of irregular shape and size and agglomerated to form larger particles. This showed that the ongoing mixing during evaporation that took place in the rotary evaporator did not have a great impact on the final product. An SEM image of these samples can be seen in Figure 16a. The slow evaporation method produced a mixture of smaller crystals that agglomerate easily (Figure 16b) as well as large single crystals up to 10 mm in length (Figure 17, 18). The ratio of small to large single crystals could be estimated based on Figure 19. The small crystals were very facetted and structured compared to the fast crystallization. Two crystal morphologies were observed in the larger crystals and were dependent on the crystallographic direction of growth with respect to the bottom of the glass dish in which they were grown. Crystals with clearly hexagonal geometry occur when the crystals grew with the c lattice direction perpendicular and the a and b lattice directions parallel to the bottom of the glass dish, as seen in Figure 17a and 18a. Rectangular crystal geometries were observed when the crystals grew with the c lattice parameter parallel to the bottom of the glass dish. This can be seen in Figure 17b and 18b.

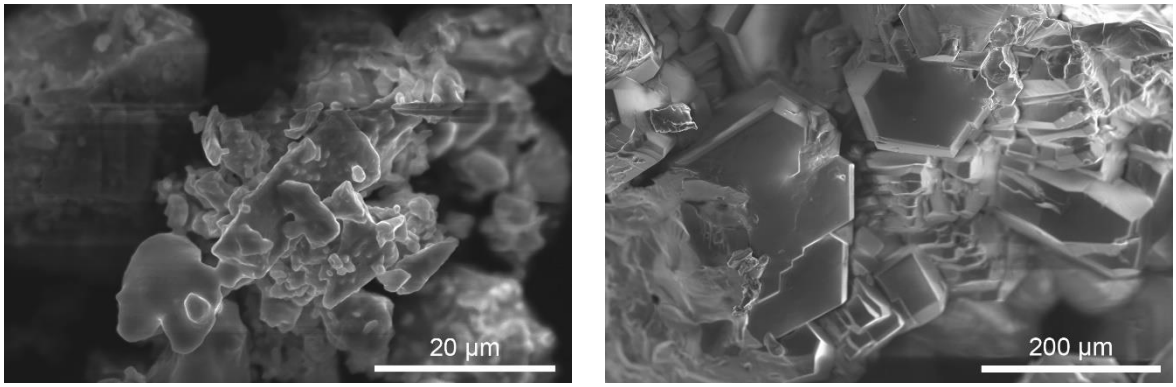

(a) (b)

Figure 16: SEM of $[(CH_2CH_3)_4N][FeBrCl_3]$ in water, crystallized fast (a) and slowly (b).

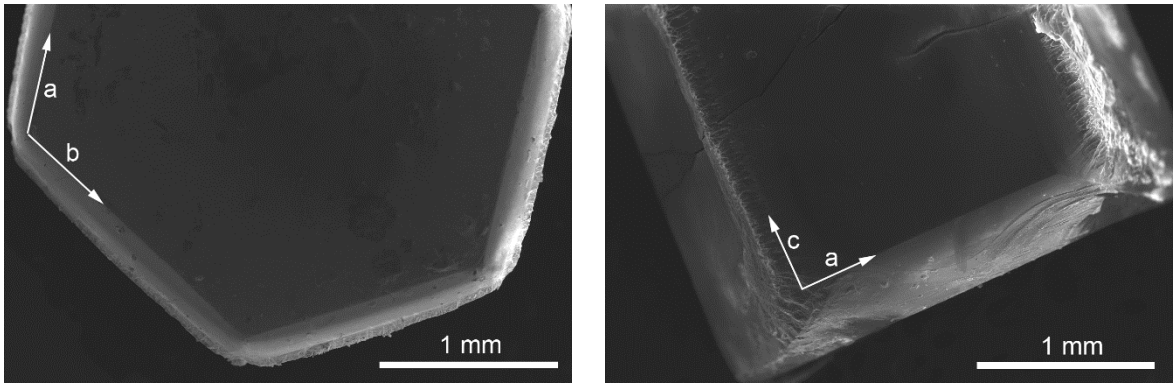

(a) (b)

Figure 17: SEM images of single crystals of $[(CH_2CH_3)_4N][FeBrCl_3]$ in water, crystallized slowly. Two different crystal shapes are present, (a) and (b).

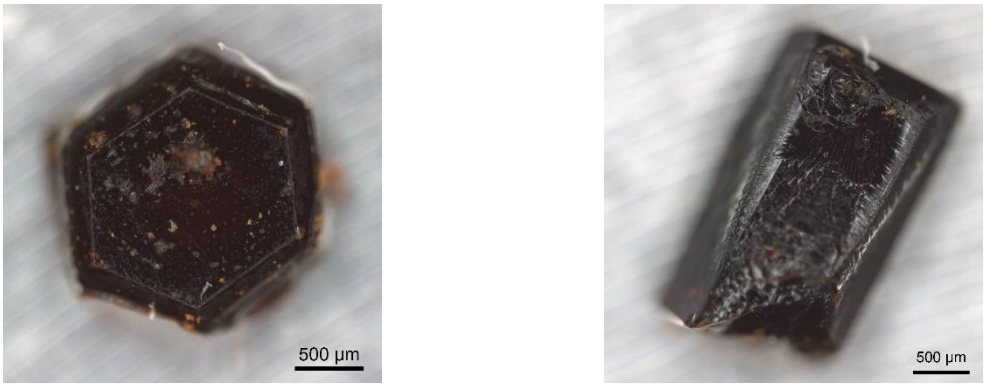

(a) (b)

Figure 18: Optical microscope images of single crystals of $[(CH_2CH_3)_4N][FeBrCl_3]$ in water, crystallized slowly. Two different crystals shapes are present, (a) and (b).

Figure 19: $[(CH_2CH_3)_4N][FeBrCl_3]$, slowly crystallized in water.

Powder-XRD analysis of slow and fast crystallization of $[(CH_2CH_3)_4N][FeBrCl_3]$ revealed no significant differences, as seen in Figure 20. Both samples were phase pure, when fitting the stable room temperature structure, *$P6_3mc$*, as suggested in literature for $[(CH_2CH_3)_4N][FeBrCl_3]$.

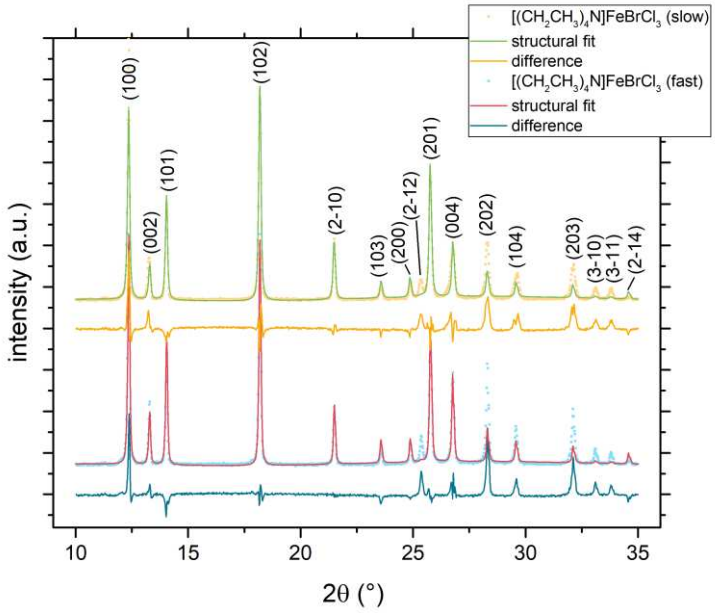

Figure 20: Comparison of powder-XRD of $[(CH_2CH_3)_4N][FeBrCl_3]$ in water, crystallized slowly and fast. The structural fit is based on the $P6_3mc$ crystal structure profile.

5.1.4.2. $[(CH_3)_4N][FeBrCl_3]$

Evaporation of a solution of $[(CH_3)_4N][FeBrCl_3]$ took longer because a thin layer of crystals formed on the surface, trapping the liquid. This can be seen in Figure 21. Underneath, facetted growth of rectangular shape could be observed, with the crystals assembling into large agglomerates, as seen in Figure 22. They were collected to dry and then pressed into disks for electrical measurements.

Figure 21: $[(CH_3)_4N][FeBrCl_3]$, slowly crystallized in water.

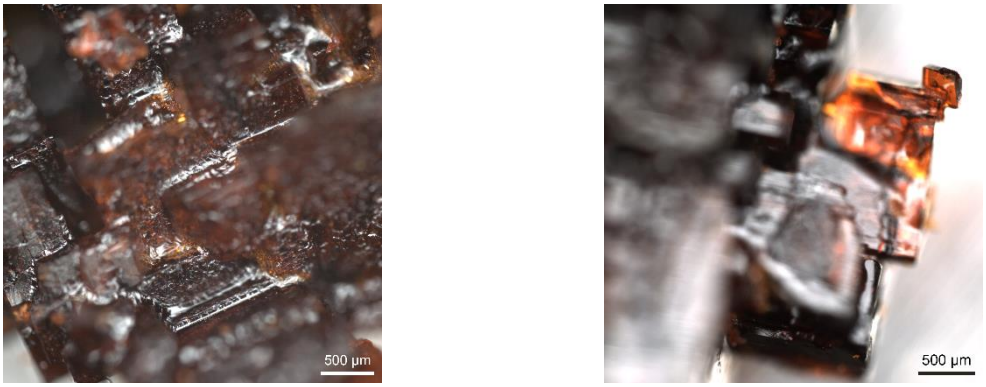

Figure 22: Optical microscopy images of $[(CH_3)_4N][FeBrCl_3]$, slowly crystallized in water.

Comparing powder-XRD of $[(CH_3)_4N][FeBrCl_3]$, crystallized either slowly or quickly, showed that reflections matched well, as seen in Figure 23. The peaks in the diffractogram taken from a sample that was crystallized slowly were less sharp. This broadening of the peaks is an indication for a smaller amount of crystallinity in the sample, possibly caused by the addition of the amorphous layer on the surface of the sample.

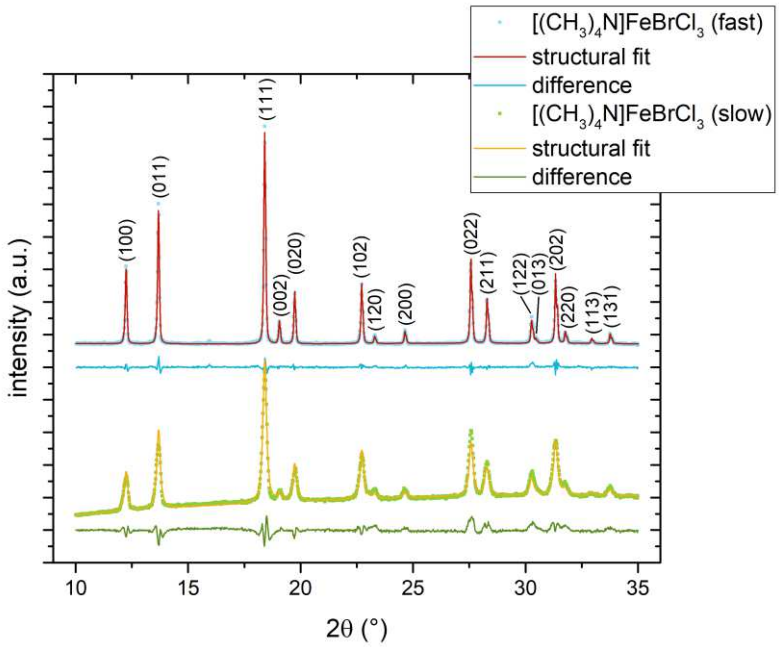

Figure 23: Comparison of powder-XRD of [(CH₃)₄N][FeBrCl₃] in water, crystallized slowly and fast. The structural fit is based on the Amm2 crystal structure profile.

5.1.4.3. [(CH₂CH₃)₄N]₀.₈[(CH₃)₄N]₀.₂[FeBrCl₃]

Slow crystallization experiments were also performed on other compositions, like $[(CH_2CH_3)_4N]_{0.8}[(CH_3)_4N]_{0.2}[FeBrCl_3]$. This mixed composition showed a phase separation in the powder-XRD compared to the fast crystallization methods, as seen in Figure 24. The pattern of $[(CH_2CH_3)_4N]_{0.8}[(CH_3)_4N]_{0.2}[FeBrCl_3]$, produced by fast crystallization, was in good agreement with *P6₃mc*, the crystal-structure of $[(CH_2CH_3)_4N][FeBrCl_3]$. This method may prevent phase separation and favor the formation of a kinetically stabilized solid solution. The same composition, crystallized through evaporation at room temperature, separated into two separate phases, *P6₃mc* ($[(CH_2CH_3)_4N][FeBrCl_3]$) and *Amm2* ($[(CH_3)_4N][FeBrCl_3]$). Giving the system time to crystallize slowly potentially caused $[(CH_2CH_3)_4N][FeBrCl_3]$ and $[(CH_3)_4N][FeBrCl_3]$ to grow as separate phases, which might be more thermodynamically stable. $[(CH_2CH_3)_4N][FeBrCl_3]$ and $[(CH_3)_4N][FeBrCl_3]$ have different solubilities, so by giving the system time to separate, one of the compositions could crystallize first.

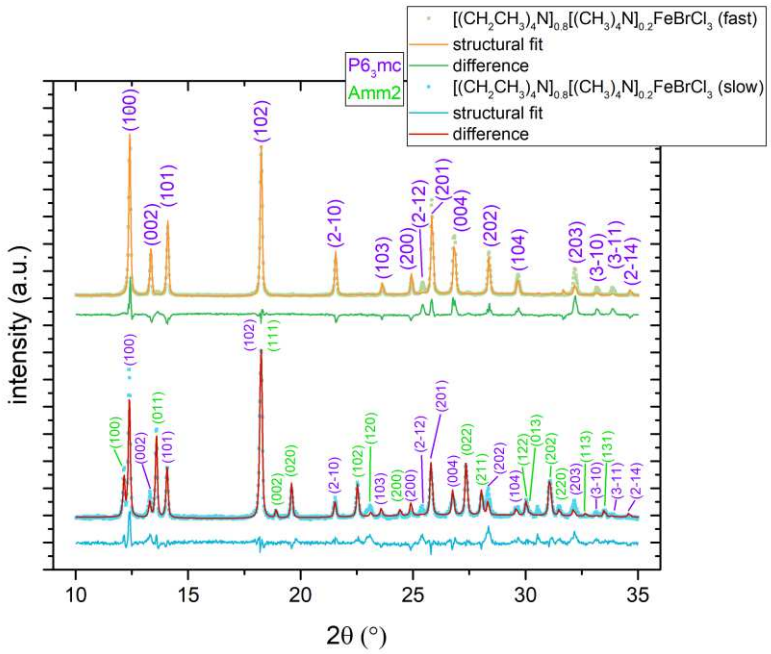

Figure 24: Powder-XRD of $[(CH_2CH_3)_4N]_{0.8}[(CH_3)_4N]_{0.2}[FeBrCl_3]$, crystallized in water slowly and fast. The structural fit is based on the Amm2 and $P6_3mc$ crystal structure profiles.

5.1.4.4. $[(CH_2CH_3)_4N]_{0.9}[(CH_3)_4N]_{0.1}[FeBrCl_3]$

The same could be observed for $[(CH_2CH_3)_4N]_{0.9}[(CH_3)_4N]_{0.1}[FeBrCl_3]$, as seen in Figure 25. The metastable formation of a solid solution was repressed by slow crystallization, giving the system time to split into the two main phases, *$P6_3mc$* and *Amm2*.

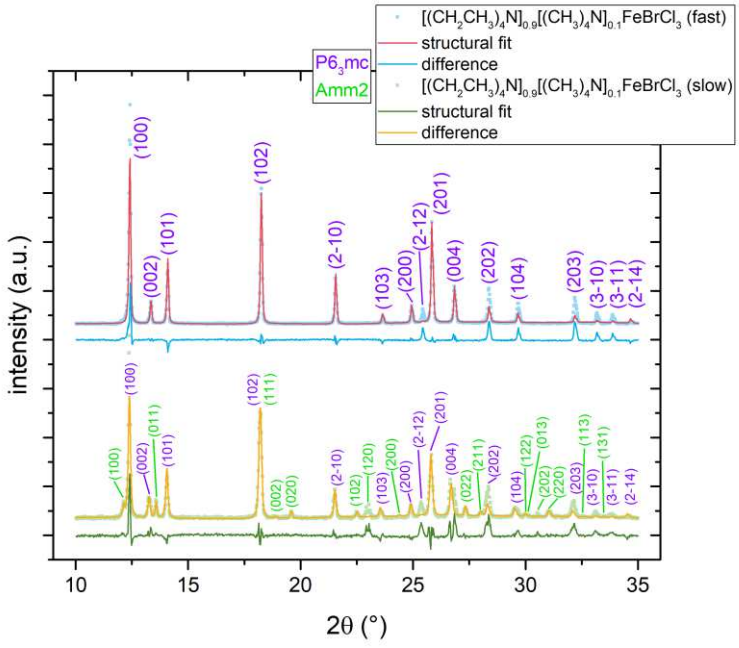

Figure 25: Powder-XRD of $[(CH_2CH_3)_4N]_{0.9}[(CH_3)_4N]_{0.1}[FeBrCl_3]$, crystallized in water slowly and fast. The structural fit is based on the Amm2 and $P6_3mc$ crystal structure profiles.

Because of the similarity of the two starting materials, $[(CH_2CH_3)_4N][FeBrCl_3]$ and $[(CH_3)_4N][FeBrCl_3]$, there is a region in their combined phase diagram in which they crystallize as one phase with the minor compound dissolved in the structure of the major constituent. The amount of solubility seems to depend on the crystallization rate.

Both $[(CH_2CH_3)_4N]_{0.9}[(CH_3)_4N]_{0.1}[FeBrCl_3]$ and $[(CH_2CH_3)_4N]_{0.8}[(CH_3)_4N]_{0.2}[FeBrCl_3]$ crystallized in a fashion similar to pure $[(CH_2CH_3)_4N][FeBrCl_3]$, suggesting that the majority crystal phase is still *P6₃mc*. The sample containing 10 mol% CH_3-substitution groups formed more single crystals >2 mm than the one containing 20 mol%, as seen in Figure 26. While this observation could be based on the different compositions of the samples, it could also be caused by slightly different lab conditions, resulting in a slower crystallization rate and therefore different crystal sizes.

(a) (b)

Figure 26: $[(CH_2CH_3)_4N]_{0.8}[(CH_3)_4N]_{0.2}[FeBrCl_3]$ (a) and $[(CH_2CH_3)_4N]_{0.9}[(CH_3)_4N]_{0.1}[FeBrCl_3]$ (b), slowly crystallized in water.

5.2. Structural study of the $[(CH_2CH_3)_4N]_x[(CH_3)_4N]_{1-x}[FeBrCl_3]$ system

Powder-XRD analysis was employed to investigate the crystal structure as a function composition for the solid solution system. The main goal was to identify the structural phases present in each composition and determine if there was any solubility of the organic cations in the respective structures. Crystal structure profiles of $[(CH_3)_4N][FeBrCl_3]$ and $[(CH_2CH_3)_4N][FeBrCl_3]$ from literature[6,9] were fitted to confirm the structure. Substitution of the differently sized cations in their respective parent structures or the inclusion of ions at interstitial positions were expected to cause the structure to expand or contract and thus, structural fitting with Rietveld refinement was used to determine changes in the lattice parameters as a function of composition.

5.2.1. $[(CH_2CH_3)_4N][FeBrCl_3]$ and $[(CH_3)_4N][FeBrCl_3]$

Powder-XRD analysis was conducted on dried samples of $[(CH_3)_4N][FeBrCl_3]$ and $[(CH_2CH_3)_4N][FeBrCl_3]$ (Figure 27, 28). An overview over the cell parameters of $[(CH_3)_4N][FeBrCl_3]$ and $[(CH_2CH_3)_4N][FeBrCl_3]$ and the quality of the fit of the respective structures (*Amm2* and *P6₃mc*) is given in Table 2.

Table 2: Lattice parameters and R_{wp} of $[(CH_3)_4N][FeBrCl_3]$ and $[(CH_2CH_3)_4N][FeBrCl_3]$.

	$[(CH_3)_4N][FeBrCl_3]$	$[(CH_2CH_3)_4N][FeBrCl_3]$
space-group	*Amm2*	*P6₃mc*
a (Å)	7.2195	8.2634
b (Å)	8.9869	8.2634
c (Å)	9.3055	13.320
V (Å^3)	603.75	787.70
R_{wp}	2.78	9.15

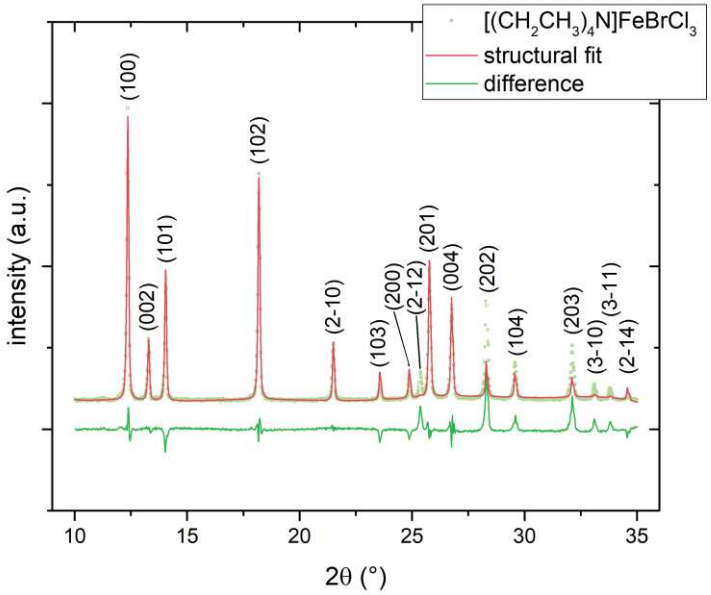

Figure 27: Powder-XRD of $[(CH_2CH_3)_4N][FeBrCl_3]$, with the room temperature phase P6₃mc fitted. Displayed are the measured points, the calculated fit and the mismatch between the two. Peaks are labelled according to their (hkl)-value.

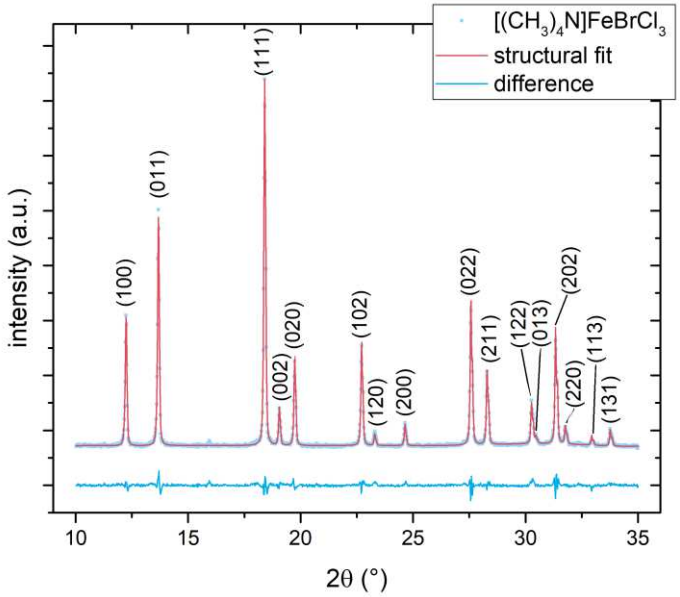

Figure 28: Powder-XRD of $[(CH_3)_4N][FeBrCl_3]$ with the room temperature phase Amm2 fitted. Displayed are the measured points, the calculated fit and the mismatch between the two. Peaks are labelled according to their (hkl)-value.

Based on the fit of the models it can be confirmed that $[(CH_3)_4N][FeBrCl_3]$ and $[(CH_2CH_3)_4N][FeBrCl_3]$ were synthesized as a single phase material with the expected space groups, *Amm*2 and *P6₃mc*, respectively. Three dimensional models of these space groups were constructed in VESTA (Figure 29). Hydrogen atoms are neglected for improved presentation.

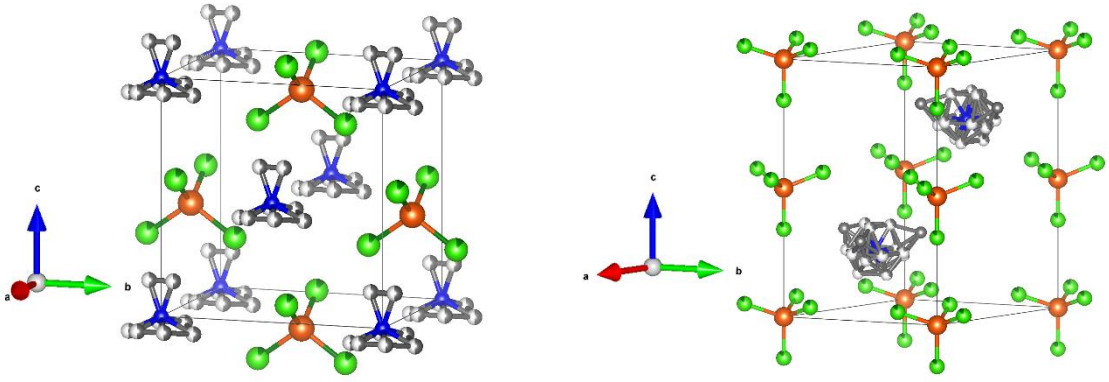

(a) (b)

Figure 29: Models of the crystallographic space groups Amm2 (a) and P6₃mc (b), constructed in VESTA. Visible atoms are iron (orange), chlorine/bromine (green), nitrogen (blue), carbon (grey)

5.2.2. Structural changes in $[(CH_2CH_3)_4N]_x[(CH_3)_4N]_{1-x}[FeBrCl_3]$

SEM images and powder-XRD of a set of samples covering the whole system of $[(CH_2CH_3)_4N]_x[(CH_3)_4N]_{1-x}[FeBrCl_3]$ (x = 0 – 1) were compared. Compositions were prepared in 10 mol% intervals across the composition range, i.e. 10, 20, 30, 40 mol%…etc. Structural

changes as a function of composition were expected to produce new electrical properties different from $[(CH_2CH_3)_4N][FeBrCl_3]$ and $[(CH_3)_4N][FeBrCl_3]$.

Water was chosen to be the most useful solvent, both in terms of its ability to dissolve all the precursors as well as the environmental aspects of developing a green synthesis route. The most reasonable approach to produce those samples was the use of a rotary evaporator, because of the rate at which samples can be produced, its reliability and the fact that faster crystallization rates were more likely to kinetically stabilize the metastable solid solution phases of the composition.

The crystal morphology of the whole system was heavily influenced by the composition. The SEM images clearly showed that individual crystals agglomerated heavily, an effect most likely caused by the fast crystallization rate. Compositions containing low amounts of $[(CH_2CH_3)_4N]^+$-cations consisted of mostly hexagonal prisms (Figure 30). This structure resembled the unit cell of the *P6₃mc* structure of $[(CH_2CH_3)_4N][FeBrCl_3]$ even though it contained only a small fraction of this precursor. With increasing amounts of $[(CH_2CH_3)_4N]^+$-cations, fewer highly facetted crystals appeared and the overall morphology became more irregular, both in terms of crystal morphology and size. This can be seen in Figures 31-33. Agglomeration remained a trend throughout the whole range.

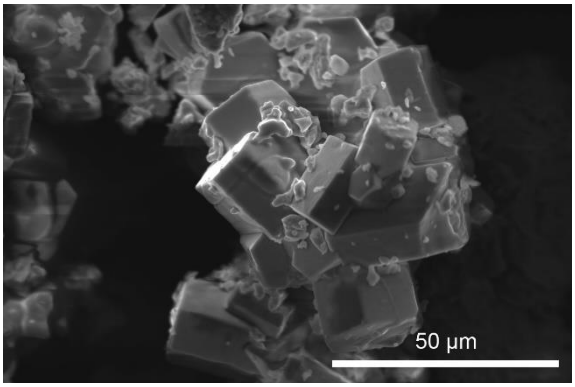

Figure 30: SEM image of $[(CH_2CH_3)_4N]_{0.1}[(CH_3)_4N]_{0.9}[FeBrCl_3]$

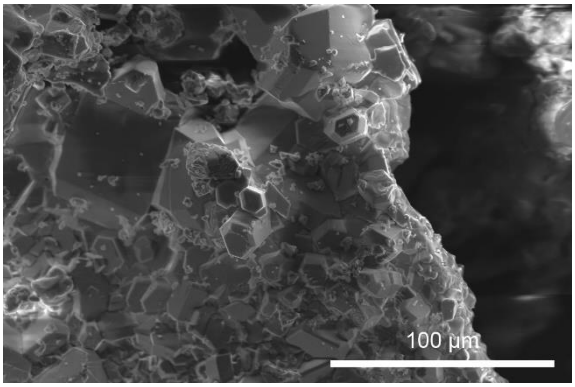

Figure 31: SEM image of $[(CH_2CH_3)_4N]_{0.2}[(CH_3)_4N]_{0.8}[FeBrCl_3]$

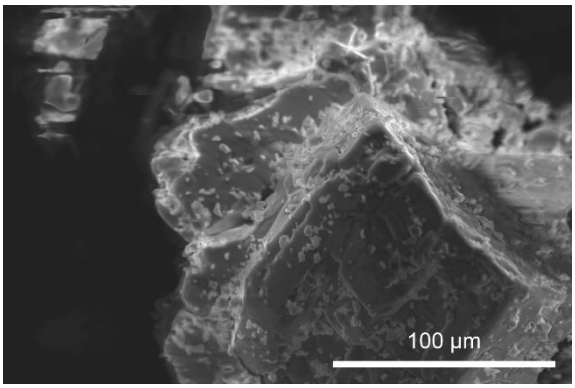

Figure 32: SEM image of $[(CH_2CH_3)_4N]_{0.8}[(CH_3)_4N]_{0.2}[FeBrCl_3]$

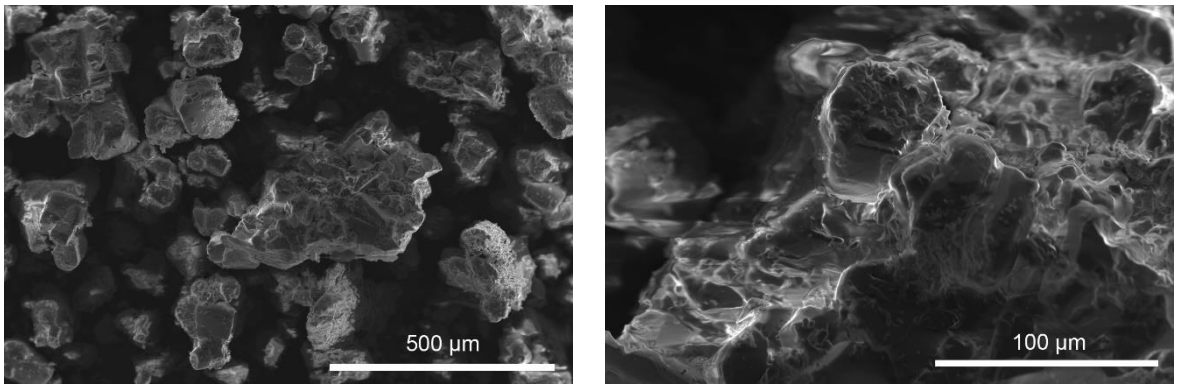

Figure 33: SEM images of $[(CH_2CH_3)_4N]_{0.9}[(CH_3)_4N]_{0.1}[FeBrCl_3]$

Comparing the powder-XRD data (Figure 34) revealed that any peaks associated with the hexagonal *P6₃mc*-structure, which is the stable room temperature phase of $[(CH_2CH_3)_4N][FeBrCl_3]$, were more intense in the diffractogram belonging to $[(CH_2CH_3)_4N]_{0.9}[(CH_3)_4N]_{0.1}[FeBrCl_3]$. There were no peaks that belonged only to the *Amm2*-space group, which was the stable structure of the minority solid solution end member $[(CH_3)_4N][FeBrCl_3]$. Some of the peaks overlapped, like the (100)-peak at 12.36°, or the (111)-peak (*Amm2*) and (102)-peak (*P6₃mc*) at 18.37°, making it difficult to determine the exact contribution of the individual structures to the overall diffractogram. Additional peaks,

which belonged to the *Amm2*-space group were present in the diffractogram of $[(CH_2CH_3)_4N]_{0.1}[(CH_3)_4N]_{0.9}[FeBrCl_3]$, showing that a larger fraction of the sample had crystallized with that structure. The overlapping of peaks and the different intensities of the reflections of the two main structures made it difficult to give accurate determinations about whether single phase materials were synthesized or not and the fraction of each individual phase in the case of a multiphase material, but an attempt will be made to quantify phase fractions in section 5.2.3.

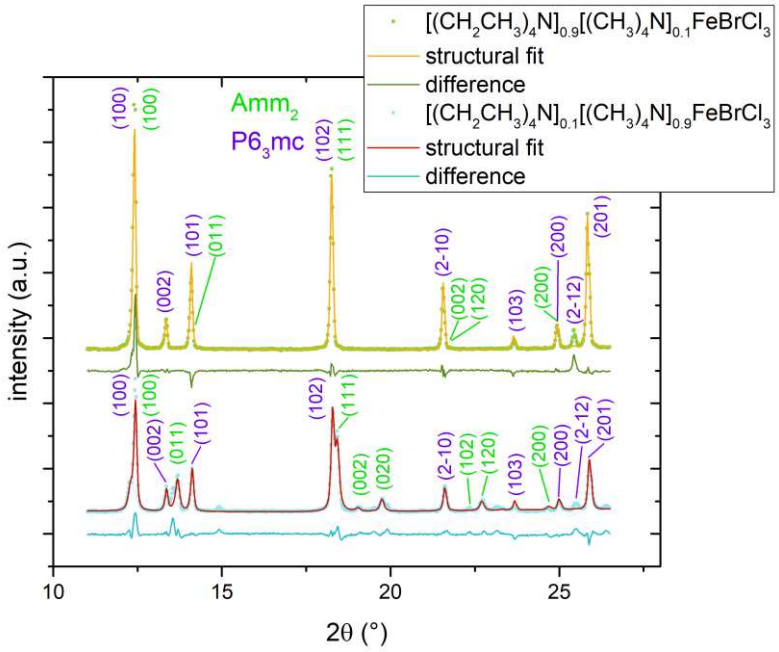

Figure 34: Powder-XRD of $[(CH_2CH_3)_4N]_{0.9}[(CH_3)_4N]_{0.1}[FeBrCl_3]$ and $[(CH_2CH_3)_4N]_{0.1}[(CH_3)_4N]_{0.9}[FeBrCl_3]$. The structural fit is based on $P6_3mc$ and Amm2 crystal structure profiles.

5.2.3. Changes in the crystal structure as a function of the composition

From a structural point of view, the addition of a smaller cation ($[(CH_3)_4N]^+$) into the *$P6_3mc$* lattice of the $[(CH_2CH_3)_4N][FeBrCl_3]$ crystal was expected to cause a decrease of the lattice parameters and the unit cell volume. This was investigated by comparing the powder-XRD data of the $[(CH_2CH_3)_4N]_x[(CH_3)_4N]_{1-x}[FeBrCl_3]$ samples prepared form aqueous solutions. At a certain point in the composition, the lattice was expected to switch to the *Amm2* space group of $[(CH_3)_4N][FeBrCl_3]$, dissolving larger $[(CH_2CH_3)_4N]^+$-cations. Changes in the crystal structure were measured by fitting both space groups of $[(CH_3)_4N][FeBrCl_3]$ and $[(CH_2CH_3)_4N][FeBrCl_3]$ to all samples of the whole composition range. This was done in two steps, fitting the structures separately. The lattice parameters of the newly refined models for *Amm2* and *$P6_3mc$* were plotted as a function of composition resulting in Figure 35 and 36.

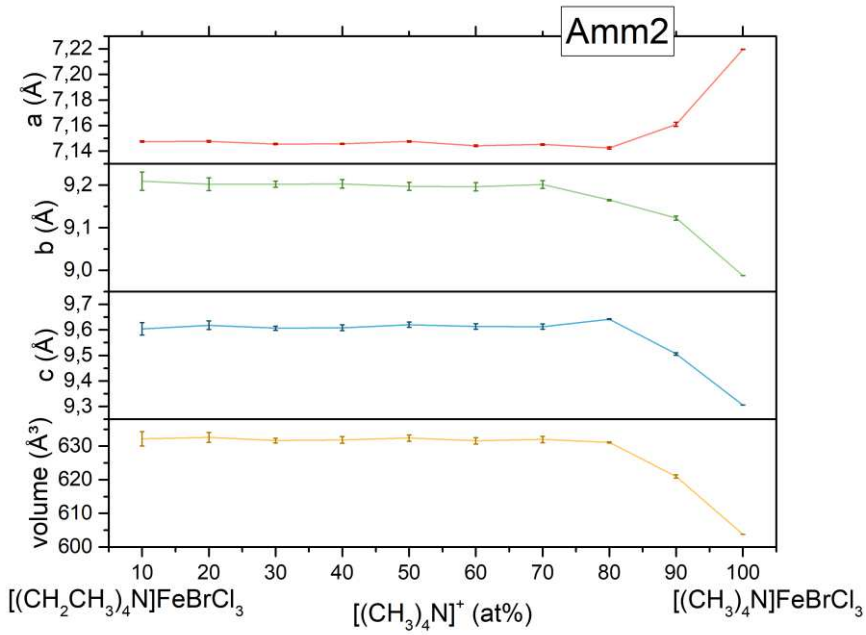

Figure 35: Lattice parameter and unit cell volume of the material with space group Amm2 as a function of composition.

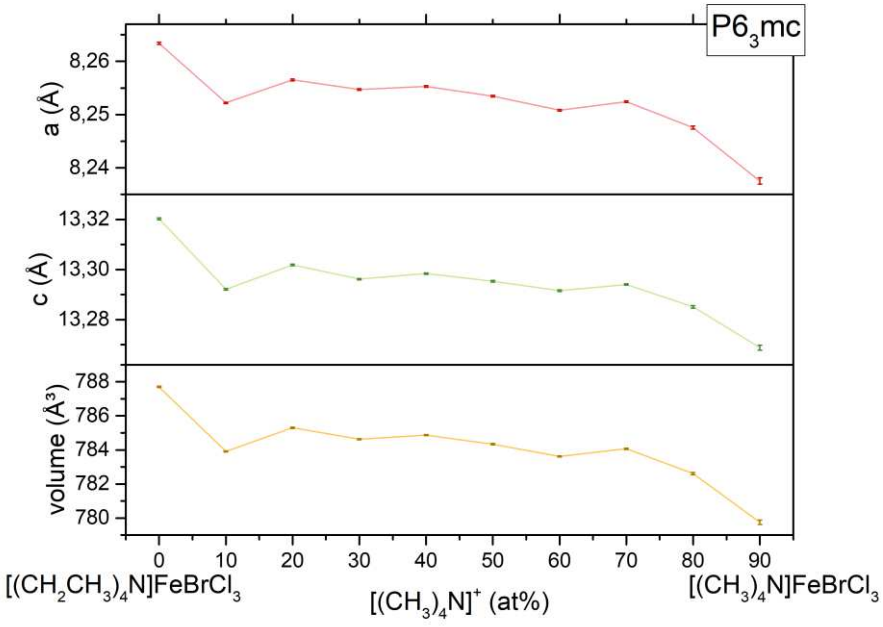

Figure 36: Lattice parameter and unit cell volume of the material with space group P6₃mc as a function of composition.

When investigating the evolution of the *Amm2* space group over the composition range, there was a clear change in the lattice parameters and total unit cell volume as a function of composition. The b and c lattice parameters increased by up to approximately 2 and 3 %

respectively when adding up to 20 mol% $[(CH_2CH_3)_4N]^+$ into the composition. However, the a lattice parameter decreased by approximately 0.7 % in the same compositional range. This resulted in a total unit cell volume increase of around 5 %. The lattice parameter change and total volume expansion suggested that there is some solid solubility of the larger $[(CH_2CH_3)_4N]^+$-cation in the *Amm2* structure at the cation site in substitution of $[(CH_3)_4N]^+$.

The parameters of the *P6₃mc* space group of $[(CH_2CH_3)_4N][FeBrCl_3]$ decreased gradually, as expected when substituting the smaller $[(CH_3)_4N]^+$ for the larger $[(CH_2CH_3)_4N]^+$ cation in the lattice. At around 80 mol% $[(CH_3)_4N]^+$ the parameters and the cell volume decreased more rapidly, suggesting that a lot of the $[(CH_3)_4N]^+$-cations were dissolved. This coincides with the findings on the *Amm2* structure. Determining the cell parameters of the minority phase (*P6₃mc* in the $[(CH_3)_4N][FeBrCl_3]$-rich part of the phase diagram and vice versa) was difficult, because of peak overlap and lower percentages of the respective phases which lead to low XRD peak intensities.

To visualize this, both space groups were fitted to each of the compositions made and the relative phase percentages were determined. The results can be seen in Figure 37. By following the phase percentages as a function of composition multiple observations were made. Firstly, following previous findings, the amount of *P6₃mc* increased drastically to 40 – 50 wt% once 10 – 20 mol% of $[(CH_2CH_3)_4N]^+$-cations were added. This large portion of *P6₃mc* suggested that when added in small amounts to the $[(CH_3)_4N]^+$ rich composition, the $[(CH_2CH_3)_4N]^+$ had very low solubility, instead precipitating as a separate phase. For samples containing 30 – 70 mol% $[(CH_3)_4N]^+$ the phase percentage plateaued, maintaining an almost consistent ratio of *Amm2* : *P6₃mc*, at about 25 : 75. A slight trend was visible, suggesting that the amount of *P6₃mc* increased slightly by adding $[(CH_2CH_3)_4N]^+$. This suggested a compositional region of relatively consistent metastability between the phases. The lack of a consistent change in the phase percentages with composition in this region indicated that the system did not follow a lever rule as observed in many binary phase systems.

$[(CH_2CH_3)_4N]_{0.8}[(CH_3)_4N]_{0.2}[FeBrCl_3]$ and $[(CH_2CH_3)_4N]_{0.9}[(CH_3)_4N]_{0.1}[FeBrCl_3]$ consisted of up to 70 wt% *Amm2*, (Figure 37). This could be the result to a change in the phase metastability at high $[(CH_2CH_3)_4N]^+$ percentages. However at these compositions a high amount of larger $[(CH_2CH_3)_4N]^+$ ions would need to be present in the *Amm2* structure, which might be expected to increase the lattice parameters relative to *Amm2* end member structure. As a congruent change in the lattice parameters for the *Amm2* structure at these compositions

was not observed it is possible that the overlap of XRD peaks for these compositions caused increased error in the fits and inaccuracies in the ratio of the structures present. The overall accuracy of this approach was limited due to the overlap of diffraction peaks related to each structure, however, the phase percentages determined from Rietveld refinement provide a useful phase estimate.

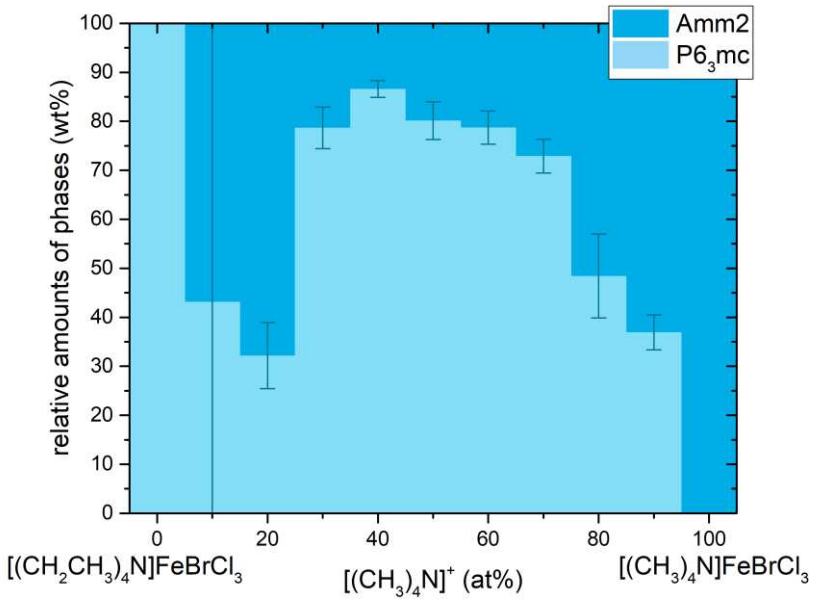

Figure 37: Relative amounts of phases as a function of composition of the $[(CH_2CH_3)_4N]_x[(CH_3)_4N]_{1-x}[FeBrCl_3]$-system.

5.2.4. Effect of pressing on the lattice parameters and crystal structure

When pressing disks from the obtained powders, the samples were subjected to 1 t of pressure and temperatures of up to 150 °C. Under these conditions, $[(CH_3)_4N][FeBrCl_3]$ transitioned into the high temperature plastic phase, $Pm\bar{3}m$, and $[(CH_2CH_3)_4N][FeBrCl_3]$ was close to the phase transition temperature into the plastic phase. The effect that this heating cycle had on the samples was investigated by comparing powder-XRD of samples before and after pressing them into disks. The pressed samples were ground up using a mortar and pestle, just like the dried powder, to make the results as comparable as possible. The results can be seen in Figure 38 and 39.

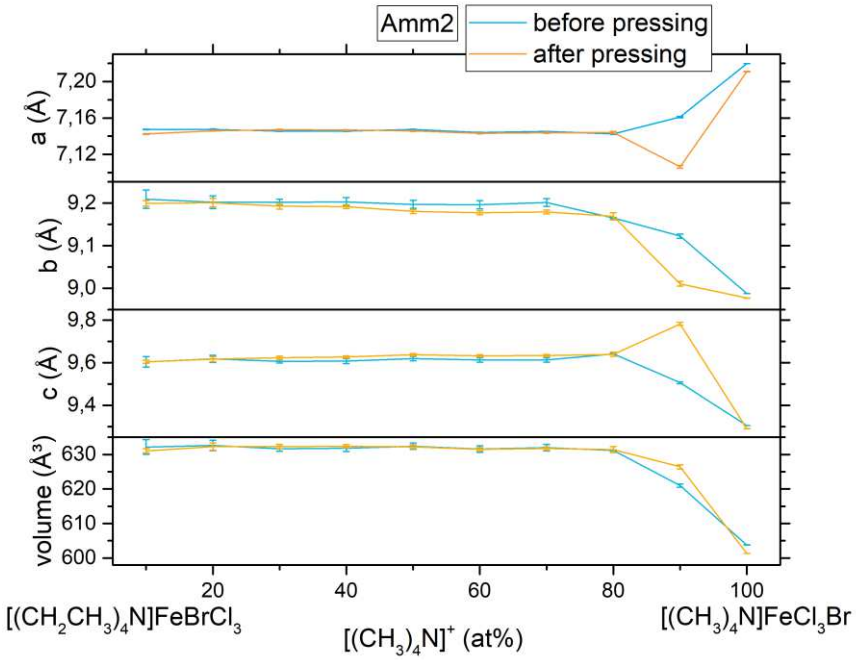

Figure 38: Lattice parameter and unit cell volume of the material with space group Amm2 as a function of composition before and after pressing the samples into disks.

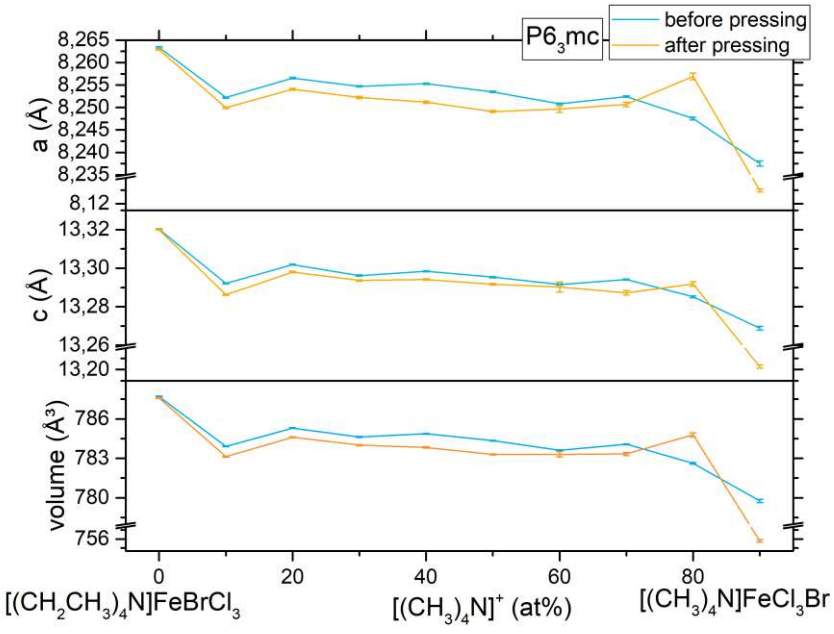

Figure 39: Lattice parameter and unit cell volume of the material with space group $P6_3mc$ as a function of composition before and after pressing the samples into disks.

Analysis of the *Amm2* space group revealed no significant changes between the crystallized and pressed samples from 0 –to 80 mol% $[(CH_3)_4N]^+$-cations (Figure 38). While being pressed, a certain degree of reorientation of the crystallites in the plastic phase might occur, possibly

causing some of the peak intensities to shift slightly and a small change in the unit cell parameters. The unit cell volume of $[(CH_2CH_3)_4N]_{0.1}[(CH_3)_4N]_{0.9}[FeBrCl_3]$ increased during pressing, owed to the increase in the lattice parameter c. The two other parameters a and b decreased while pressing but did not compensate for the elongation along the c-axis. The distortion of the unit cell could be a result of the pressure and heat applied. Elevated temperatures could also promote further interdiffusion of the two cations, resulting in an expansion of the unit cell of the smaller *Amm2* structure. Consisting of 90 mol% $[(CH_3)_4N]^+$-cations, plastic deformation was very prominent, because the sample was heated up to well above the phase transition temperature. Unit cell parameters of $[(CH_3)_4N][FeBrCl_3]$ did not change during pressing of the sample.

Lattice parameter values and unit cell volume were consistently smaller for the *P6₃mc* space group after pressing, except for $[(CH_2CH_3)_4N]_{0.2}[(CH_3)_4N]_{0.8}[FeBrCl_3]$ (Figure 39). The diffusion of smaller $[(CH_3)_4N]^+$-cations that were more mobile at 150 °C could explain these results. At 80 mol% $[(CH_3)_4N]^+$-cations, lattice parameters and unit cell volume were larger after pressing and at 90 mol% $[(CH_3)_4N]^+$-cations, the values were a lot lower than before pressing, compared to the rest of the compositions. Consisting of mostly $[(CH_3)_4N]^+$-cations, a large part of both of these compositions was exposed to temperatures well above the phase transition to the plastic phase, potentially causing a lot of additional diffusion. Elevating the temperature could also cause the solid solution in the sample to break down. This could explain the increase in the lattice parameters of the *P6₃mc* structure of $[(CH_2CH_3)_4N]_{0.2}[(CH_3)_4N]_{0.8}[FeBrCl_3]$, but this might also be the result of fit error that becomes high when there are only small amounts of a phase were present.

5.2.5. Comparison of $[(CH_2CH_3)_4N]_x[(CH_3)_4N]_{1-x}[FeBrCl_3]$ to a physical mixture

Determining the lattice parameters and phase percentages of mixed compositions from powder-XRD data posed a challenge, mainly due to considerable peak overlap. To verify the structural observations, a comparative powder-XRD study was done on samples of $[(CH_2CH_3)_4N][FeBrCl_3]$ and $[(CH_3)_4N][FeBrCl_3]$, mixed in physical weight percentage ratio's the same as those of $[(CH_2CH_3)_4N]_{0.2}[(CH_3)_4N]_{0.8}[FeBrCl_3]$ and $[(CH_2CH_3)_4N]_{0.8}[(CH_3)_4N]_{0.2}[FeBrCl_3]$. Differences between the powder-XRD profiles of the solid solution and the physical mixture could be used to identify features that indicate solubility of each cation in the structure of the opposite end member. The clear difference between the diffractograms of the physical mixtures and the solid solution confirmed that the two phases

did not crystallize separately with the chemical stoichiometry of the end member, but did indeed exhibit some solubility of the organic cations, as seen in Figure 40.

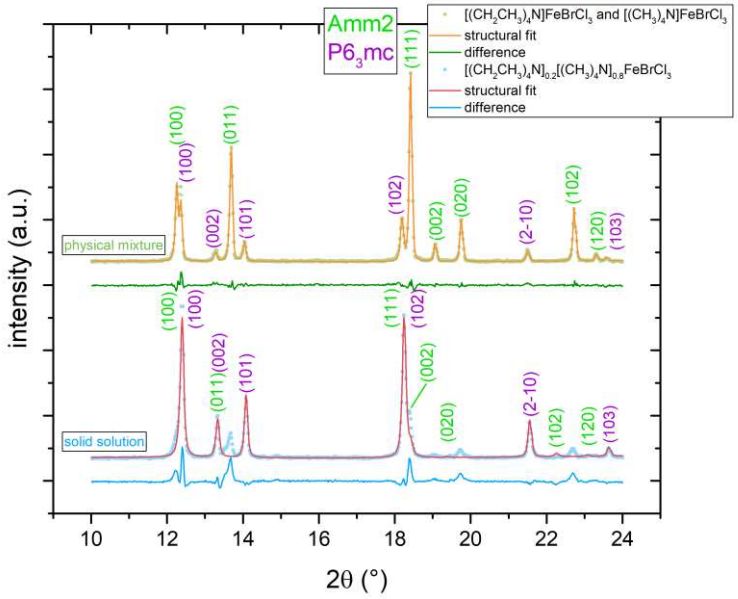

Figure 40: Powder-XRD of $[(CH_2CH_3)_4N]_{0.2}[(CH_3)_4N]_{0.8}[FeBrCl_3]$, compared to a physical mixture of 20/80 wt% $[(CH_2CH_3)_4N][FeBrCl_3]$ and $[(CH_3)_4N][FeBrCl_3]$. The structural fit is based on $P6_3mc$ and Amm2 crystal structure profiles.

In the diffractogram of the physical mixture, all peaks could be assigned to one of the structures, *$P6_3mc$* or *Amm2*. Intensities of peaks belonging to the *Amm2* phase were larger, indicating that more crystals with the *Amm2* crystal structure were present. However, in the diffractogram of $[(CH_2CH_3)_4N]_{0.2}[(CH_3)_4N]_{0.8}[FeBrCl_3]$, the peaks shifted and overlapped in a different way. Peak positions assigned to the minority phase *$P6_3mc$* were more evident, even though the amount in the initial mixture is only 20 %. This could indicate that large amounts of the sample were forced to crystallize in the *$P6_3mc$* structure.

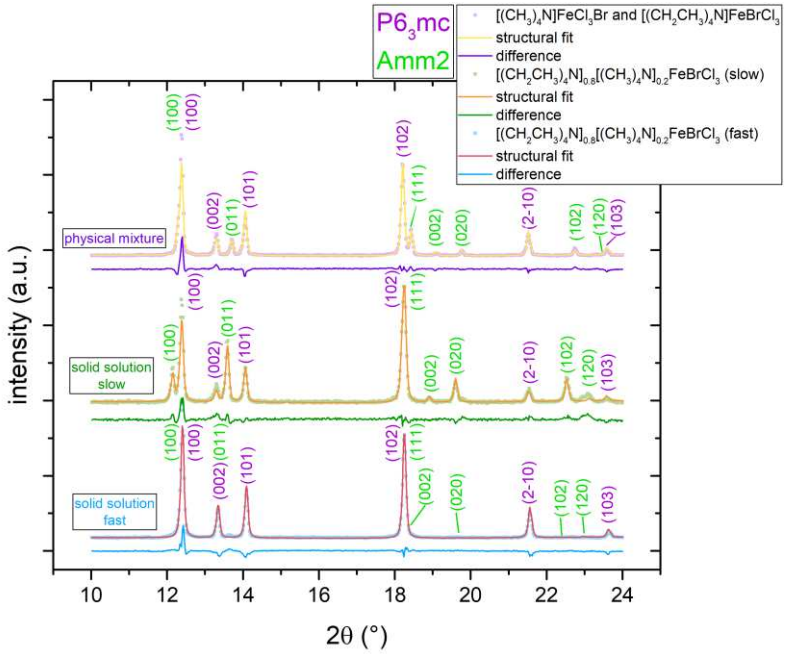

Figure 41: Powder-XRD of $[(CH_2CH_3)_4N]_{0.2}[(CH_3)_4N]_{0.8}[FeBrCl_3]$, crystallized at two different rates, compared to a physical mixture of 80/20 wt% $[(CH_2CH_3)_4N][FeBrCl_3]$ and $[(CH_3)_4N][FeBrCl_3]$. The structural fit is based on $P6_3mc$ and Amm2 crystal structure profiles.

Powder-XRD of samples with the composition $[(CH_2CH_3)_4N]_{0.2}[(CH_3)_4N]_{0.8}[FeBrCl_3]$ were also compared to the physical mixture representing the same ratio of different cations (Figure 41). This composition was crystallized in two different ways, firstly quickly in a rotary evaporator and secondly slowly over the course of several days through room temperature evaporation. While the diffractogram of the slowly crystallized sample still contained all peaks belonging to both space groups of the pure components, the sample that was crystallized more rapidly was missing most peaks belonging to the *Amm2* phase. The development of a solid solution is probably a thermodynamically unstable product and therefore unfavored over the co-precipitation of two separate phases, given enough time to crystallize. This could be further promoted by different solubilities of the precursors in water. Forcing fast precipitation of the product through elevated temperatures and vacuum caused the formation of the kinetically favored solid solution, as seen in the XRD where no peaks belonging to the *Amm2* structure remained.

5.2.6. Effect of the pressing process on the crystal structure

Samples were pressed to investigate plasticity and formability in the plastic mesophase and to prepare flat, thin samples with suitable dimensions for electrical measurements. Powder-XRD was conducted before and after pressing to study possible changes in the phase assemblage and

crystal structure. Pressed disks were ground up with a mortar and pestle before measuring them to get comparable results.

While being in the plastic phase, reactions in the $[(CH_2CH_3)_4N]_x[(CH_3)_4N]_{1-x}[FeBrCl_3]$-system could induce further dissolution of the cations or phase separation. Since the plastic phase transition is associated to a high energy barrier and a large hysteresis, there is also a possibility of samples remaining in a high temperature phase after cooling to room temperature. This could possibly be prevented by controlling the cooling rate of the pressing.

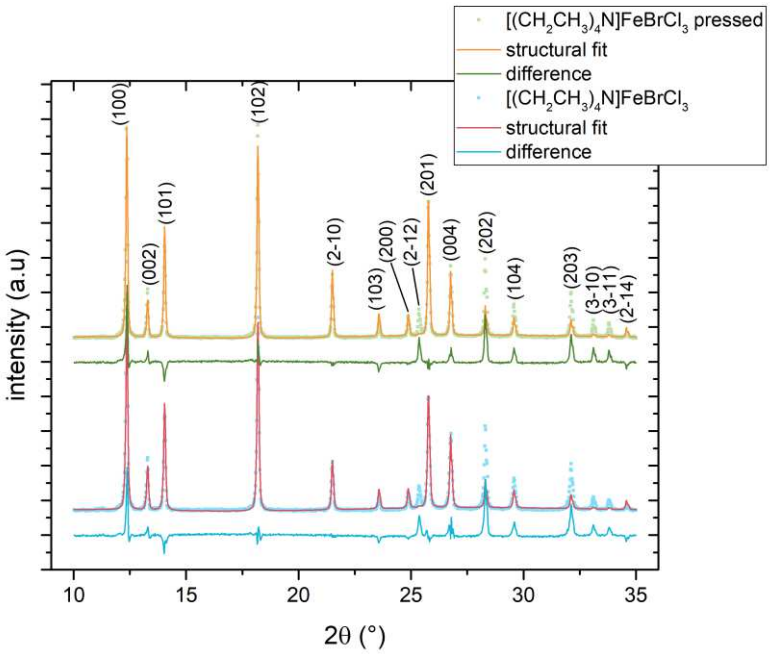

Figure 42: Powder-XRD of $[(CH_2CH_3)_4N][FeBrCl_3]$ before and after hot pressing. This process (1 t and 140 °C) does not seem to have an effect on the crystallinity of the samples. The structural fit is based on $P6_3mc$ crystal structure profile.

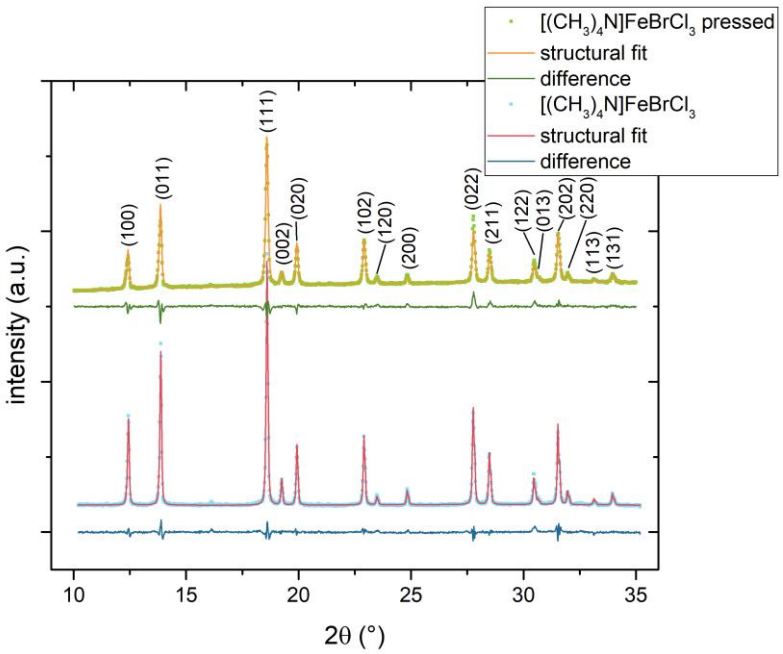

Figure 43: Powder-XRD of [(CH₃)₄N][FeBrCl₃] before and after hot pressing. This process (1 t and 150 °C) does not seem to have an effect on the crystallinity of the sample. The structural fit is based on Amm2 crystal structure profile.

Comparing the powder-XRD confirmed that the crystallinity and crystal structure of $[(CH_2CH_3)_4N][FeBrCl_3]$ and $[(CH_3)_4N][FeBrCl_3]$ does not change during pressing (Figure 42 and 43). Powder-XRD before and after pressing looked almost identical in both cases, and the *P6₃mc* and *Amm2* structure, respectively fitted well. The crystal structure of the mixed compositions $[(CH_2CH_3)_4N]_x[(CH_3)_4N]_{1-x}[FeBrCl_3]$ remained the same after pressing, as seen in Figure 44. Fitting the *P6₃mc* and *Amm2* crystal structure profiles was in good agreement with the data.

While no additional peaks appear that would suggest the formation of a new phase, some smaller peaks disappeared after pressing. The largest one was the peak at 13.7°, along with some other, smaller peaks, apparent in Figure 44. While only one composition was displayed here ($[(CH_2CH_3)_4N]_{0.5}[(CH_3)_4N]_{0.5}[FeBrCl_3]$), this was true for all samples. The reflection at 13.7° was characteristic for the (011) reflection of the *Amm2* crystal structure. When comparing powder-XRD of different compositions before pressing, the intensity of this peak decreased with increasing amounts of ethyl-groups added, supporting the hypothesis that it belonged to the *Amm2* phase.

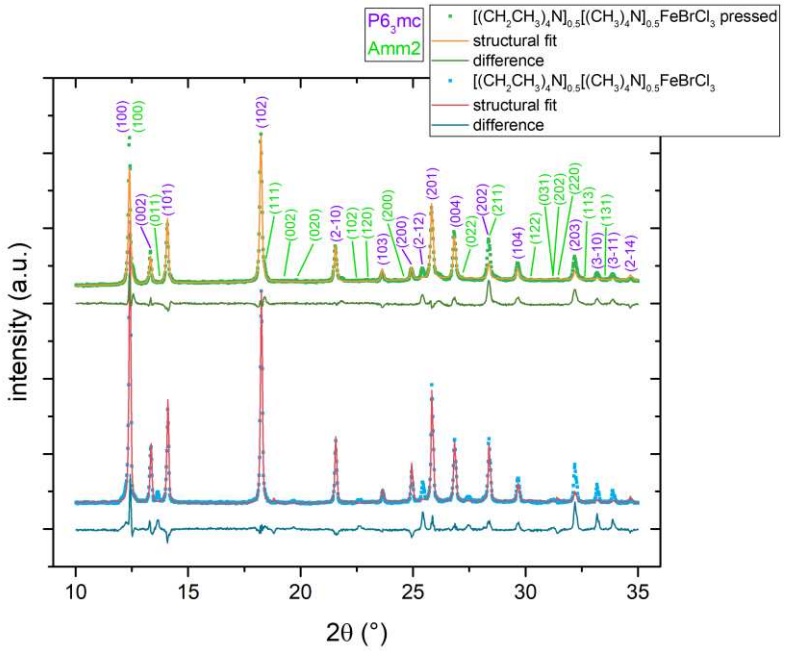

Figure 44: Powder-XRD of $[(CH_2CH_3)_4N]_{0.5}[(CH_3)_4N]_{0.5}[FeBrCl_3]$ before and after hot pressing. Some small peaks (most notably at 13.7°) disappear while pressing, which means that structural changes take place. The structural fit is based on the $P6_3mc$ and Amm2 crystal structure profiles.

Figure 45 displays the ratio of the disappearing (011)-peak to one of the most intense peaks of the *Amm2*-phase, the (111) reflection as a function of composition. The intensity of the (111)-peak is combined with the (102)-peak of *P6₃mc*, because they overlap. In the diffractogram of $[(CH_2CH_3)_4N]_{0.9}[(CH_3)_4N]_{0.1}[FeBrCl_3]$, the peak was not visible. The peak intensity increased with growing $[(CH_3)_4N]^+$-content, and rose sharply at $[(CH_2CH_3)_4N]_{0.2}[(CH_3)_4N]_{0.8}[FeBrCl_3]$ and more. Since the phase transition of $[(CH_3)_4N][FeBrCl_3]$ occurred at a lower temperature, it is possible that during pressing, further reactions took place, increasing the amount of dissolved methyl-groups in the *P6₃mc* lattice of the $[(CH_2CH_3)_4N][FeBrCl_3]$ crystals, which made peaks associated to the *Amm2* structure disappear.

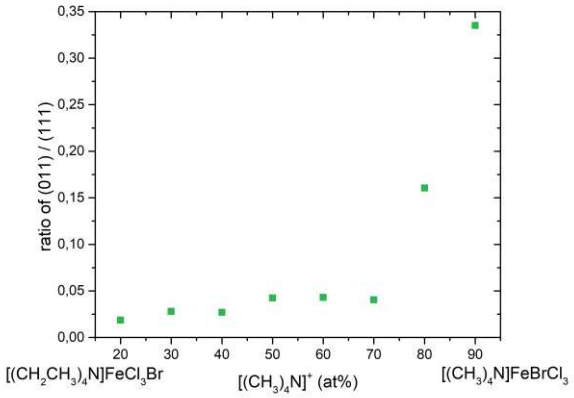

Figure 45: Ratio of the intensity of the disappearing (011)-peak to the combined (111)-peak of the Amm2 and (102)-peak of $P6_3mc$ phase as a function of the composition.

5.2.7. Differential scanning calorimetry

5.2.7.1. Phase transition as a function of composition

Differential scanning calorimetry (DSC) was performed on samples of all compositions of $[(CH_2CH_3)_4N]_x[(CH_3)_4N]_{1-x}[FeBrCl_3]$ (x = 0 – 1). The observed phase transitions, represented by positive and negative peaks in the DSC profiles, provide information about changes in the physical properties as a function of the composition of the samples. An excerpt of the DSC data is plotted in Figure 46 and 47, displaying the phase transitions upon heating and cooling on the first cycle. This study focused on the main phase transition of the system, that is the transition to the plastic phase or mesophase, which was accompanied by a large structural and entropy change. The background was removed from the data in all Figures.

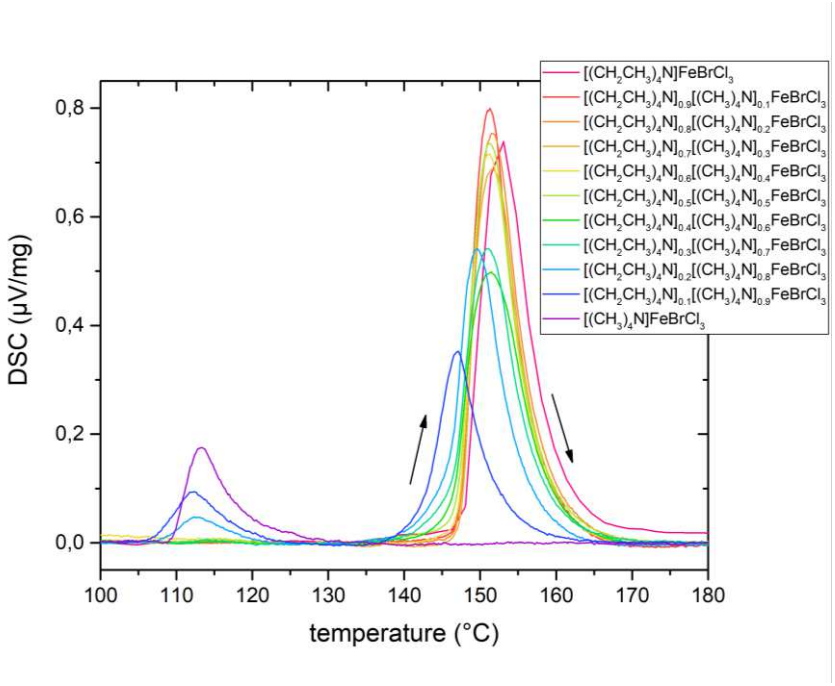

Figure 46: Excerpts of the DSC of $[(CH_2CH_3)_4N]_x[(CH_3)_4N]_{1-x}[FeBrCl_3]$ (x = 0 – 1), measured from 25 to 260 °C at 10 K/min upon heating. Depicted is the main phase transition on the first cycle.

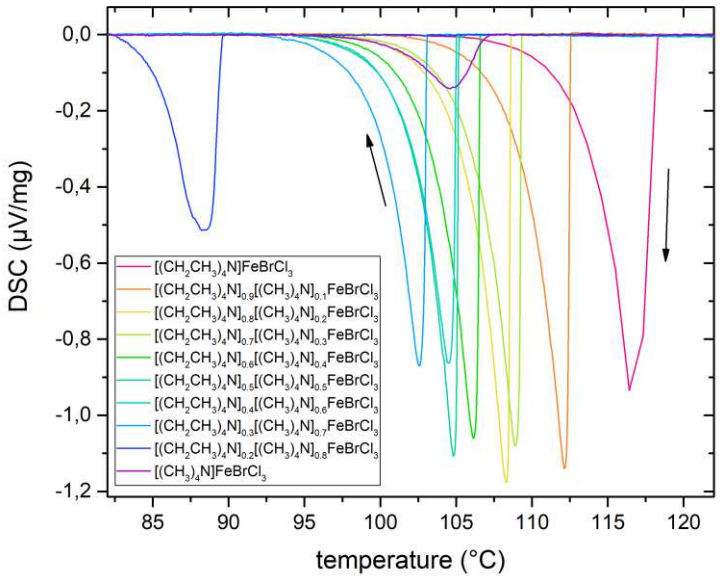

Figure 47: Excerpts of the DSC of $[(CH_2CH_3)_4N]_x[(CH_3)_4N]_{1-x}[FeBrCl_3]$ (x = 0 – 1), measured from 25 to 260 °C at 10 K/min upon cooling. Depicted is the main phase transition on the first cycle.

The plastic phase transition of $[(CH_2CH_3)_4N][FeBrCl_3]$ had a much larger peak intensity, compared to $[(CH_3)_4N][FeBrCl_3]$, indicating that a larger change in the free energy (enthalpy) of the system on transition occurred. It is worth noting that the $[(CH_3)_4N][FeBrCl_3]$ system

undergoes a total of four phase transitions as a function of temperature prior to the mesophase transition.[6] It might therefore be reasonable to suggest that the free energy of the system prior to mesophase transition was higher than that of the $[(CH_2CH_3)_4N][FeBrCl_3]$ system, thus explaining why the free energy change during the transition was less. As these transitions exhibited varying degrees of hysteresis (temperature difference on heating and cooling parts of the thermal cycle) both heating and cooling regimes were studied separately.

Due to the presence of two plastic crystal phases, one for each of the two end member compositions of the solid solution, compositions of $[(CH_2CH_3)_4N]_x[(CH_3)_4N]_{1-x}[FeBrCl_3]$ have potential to show two distinct peaks.

Phase transition temperatures in many solid solution systems vary as a function of temperature, this is seen in the binary phase diagrams of many metals and metal oxide solid solutions.[36] Therefore, the phase transition temperatures as a function of composition were studied in order to provide evidence to support the solubility of the cations in the opposite structure. On heating, samples containing 10 – 50 mol% $[(CH_3)_4N]^+$-cations exhibited only one peak that occurs slightly below the transition temperature of $[(CH_2CH_3)_4N][FeBrCl_3]$ at 153 °C. Compositions of
60 – 70 mol% $[(CH_3)_4N]^+$-cations also showed this peak but with a significantly lower intensity, while compositions 80 and 90 mol% $[(CH_3)_4N]^+$-cations showed two peaks consistent with both the *Amm2* and the *P6₃mc* transition.

In the 60 – 70 mol% $[(CH_3)_4N]^+$-cation compositions the reduced peak intensity was possibly related to a reduced enthalpy of transition. This is supported by the fact that the powder-XRD study suggests all compositions from 30 – 70 mol% $[(CH_3)_4N]^+$-cation had similar phase fractions. In the 80 and 90 mol% $[(CH_3)_4N]^+$-cation compositions on the other hand there were clearly two phase transition visible, corresponding to the $[(CH_2CH_3)_4N][FeBrCl_3]$ and $[(CH_3)_4N][FeBrCl_3]$ mesophase transitions. Thus, the peak intensities were also influenced by the mass of material undergoing the transition. Due to the fact that all compositions up to 90 mol% $[(CH_3)_4N]^+$ had a distinct peak very close the phase transition of the $[(CH_2CH_3)_4N][FeBrCl_3]$ based *P6₃mc* structure to the plastic mesophase, it can be assumed that there was limited solubility of the larger $[(CH_2CH_3)_4N]^+$ cation in the $[(CH_3)_4N][FeBrCl_3]$ based structure and therefore the presence of $[(CH_2CH_3)_4N]^+$ had a strong influence on the phase composition of the system. This observation is supported by the powder-XRD data.

On heating, there was very little change in the phase transition temperatures as a function of composition, suggesting limited solubility of the different cations in their reciprocal solvent structures (Figure 48a). For the $[(CH_3)_4N][FeBrCl_3]$ based *Amm2* structure, little hysteresis was observed between the phase transition temperature on heating and cooling which this was also the case on cooling. However, for the $[(CH_2CH_3)_4N][FeBrCl_3]$ based *P6₃mc* structure the mesophase transition exhibited large (40 °C) hysteresis on heating and cooling. Significant and systematic change in the phase transition temperature was observed as a function of composition.

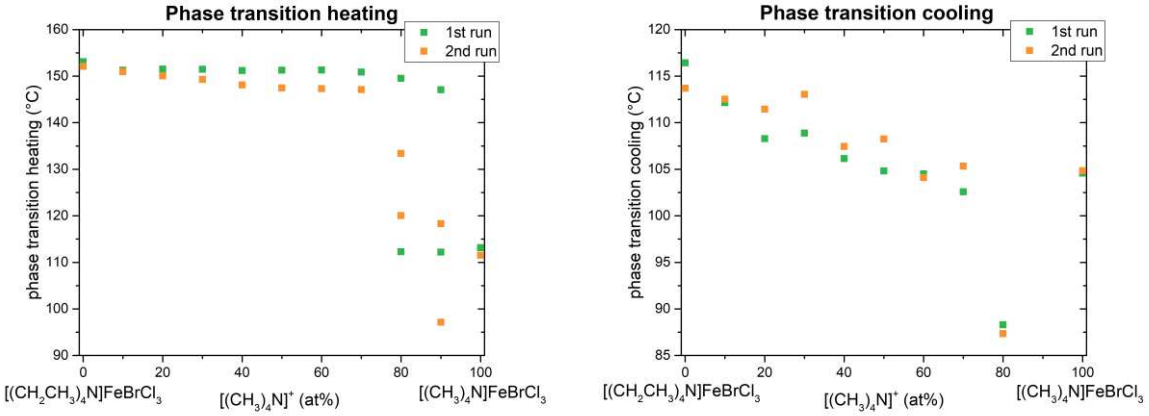

(a) (b)

Figure 48: Detected phase transition temperatures of the whole composition range of $[(CH_2CH_3)_4N]_x[(CH_3)_4N]_{1-x}[FeBrCl_3]$ upon heating (a) and cooling (b) as a function of composition.

Figure 48b is an overview over the phase transitions upon cooling on the first run of each sample. No peak could be detected for $[(CH_2CH_3)_4N]_{0.1}[(CH_3)_4N]_{0.9}[FeBrCl_3]$ down to 80 °C. This might be caused by the plastic nature of the structure, favoring super-cooled phase transitions. Starting from $[(CH_2CH_3)_4N][FeBrCl_3]$, with a phase transition at 116 °C, the switch to the low temperature structure happened at continuously lower temperatures when increasing the amount of $[(CH_3)_4N]^+$-cations in the sample. This trend went up to 70 mol% $[(CH_3)_4N]^+$, with all transitions having about the same peak intensity. This suggests that they described the transition of the $[(CH_2CH_3)_4N]$-rich phase. $[(CH_2CH_3)_4N]_{0.2}[(CH_3)_4N]_{0.8}[FeBrCl_3]$ had a much lower transition temperature, compared to the other samples. $[(CH_2CH_3)_4N]_{0.1}[(CH_3)_4N]_{0.9}[FeBrCl_3]$ and $[(CH_2CH_3)_4N]_{0.2}[(CH_3)_4N]_{0.8}[FeBrCl_3]$ had at least two phase-transitions upon heating, but fewer could be detected when being cooled down. The second transition, belonging to the $[(CH_3)_4N]$-rich phase, could happen at temperatures lower than 80 °C, which were not recorded on the measurement. The other explanation could be the

fact that both transitions happened at the same time, with the high-temperature transition being supercooled and initiated once the other phase transition happened.

All detectable phase transitions were plotted in Figure 48, for two runs performed on each sample measured back to back. Phase transition temperatures upon heating remain almost constant between $[(CH_2CH_3)_4N][FeBrCl_3]$ and $[(CH_2CH_3)_4N]_{0.3}[(CH_3)_4N]_{0.7}[FeBrCl_3]$, as mentioned above. A small decrease in transition temperature could indicate that only very little amounts of the $[(CH_3)_4N]^+$-ions dissolved in the *P6₃mc* structure, leaving it largely unchanged. This would mean that $[(CH_3)_4N][FeBrCl_3]$ crystallized separately and the phase transition was too small to be detected or happened at a temperature lower than 80 °C. On the second run, phase transition temperatures were generally lower, suggesting that heating up the samples up to 260 °C had an impact on the structure.

There are perhaps three main possibilities for changes in the transition temperatures between the first and second heating cycles. First, the heating cycle might remove volatile components from the structure, such as residual water. Second, the structure might change via the movement of defects like dislocations and vacancies. Third, the compositional gradient between different phases in the material might drive some diffusion and therefore compositional change. The phase transitions in $[(CH_3)_4N][FeBrCl_3]$ and $[(CH_2CH_3)_4N][FeBrCl_3]$ were not affected by thermal history, their phase transitions were almost exactly the same on the first and second run. This suggests that the changes between the first and second run of the other compositions were caused by structural change (defects) or compositional changes (diffusion) and were not related to the evaporation of volatile compounds.

5.2.7.2. Phase transition hysteresis

All samples display a large hysteresis in their phase transitions, as seen in Figure 49. This phenomenon could be explained by the plastic properties of the high temperature phase, allowing for a supercooled structure below the theoretical phase transition. Phase transition hysteresis of $[(CH_2CH_3)_4N][FeBrCl_3]$ was more than 35 °C, and increased with increasing amounts of $[(CH_3)_4N]^+$ added. The hysteresis reached its highest value at $[(CH_2CH_3)_4N]_{0.1}[(CH_3)_4N]_{0.9}[FeBrCl_3]$ with over 60 °C. $[(CH_3)_4N][FeBrCl_3]$ had almost no hysteresis. The hysteresis decreased on the second run, with an overall increase in the difference between the first and second round. The trend was reversed on the cooling part of the cycle. Almost all phase transitions of the second run took place at higher temperatures than on the first one.

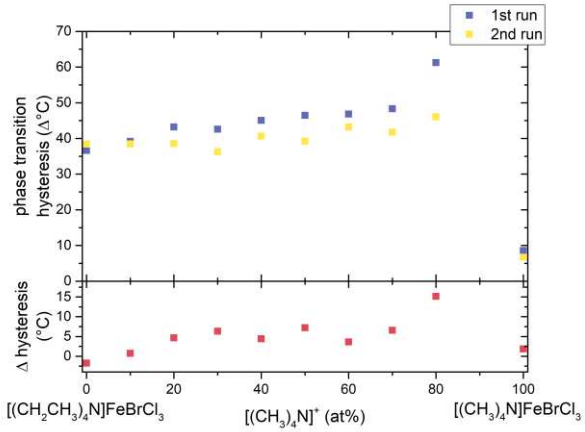

Figure 49: Phase transition hysteresis of the first and second run as a function of composition and the change in the hysteresis between first and second run.

5.2.7.3. Comparative DSC of mixed composition with physical mixture

A comparative study was performed on $[(CH_2CH_3)_4N]_x[(CH_3)_4N]_{1-x}[FeBrCl_3]$ and compared to data measured on a sample of $[(CH_2CH_3)_4N][FeBrCl_3]$ and $[(CH_3)_4N][FeBrCl_3]$, mixed in the same ratio. This way, data supporting the formation of a solid solution could be obtained. All samples were measured twice back to back to investigate the effect of past heating cycles on the phase transitions. The main phase transitions are displayed in Figure 50-52.

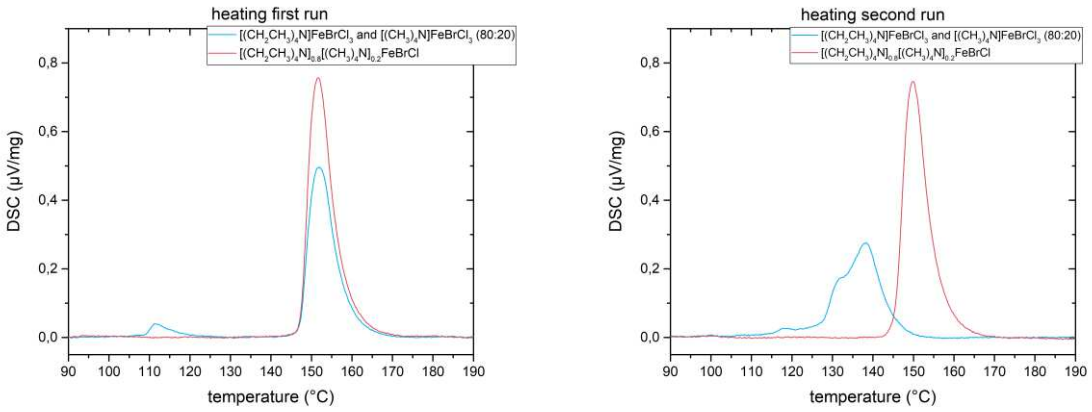

(a) (b)

Figure 50: DSC plot of $[(CH_2CH_3)_4N]_{0.8}[(CH_3)_4N]_{0.2}[FeBrCl_3]$ compared to a physical mixture of $[(CH_3)_4N][FeBrCl_3]$ and $[(CH_2CH_3)_4N][FeBrCl_3]$ in the same ratio, upon heating on the first (a) and second (b) run.

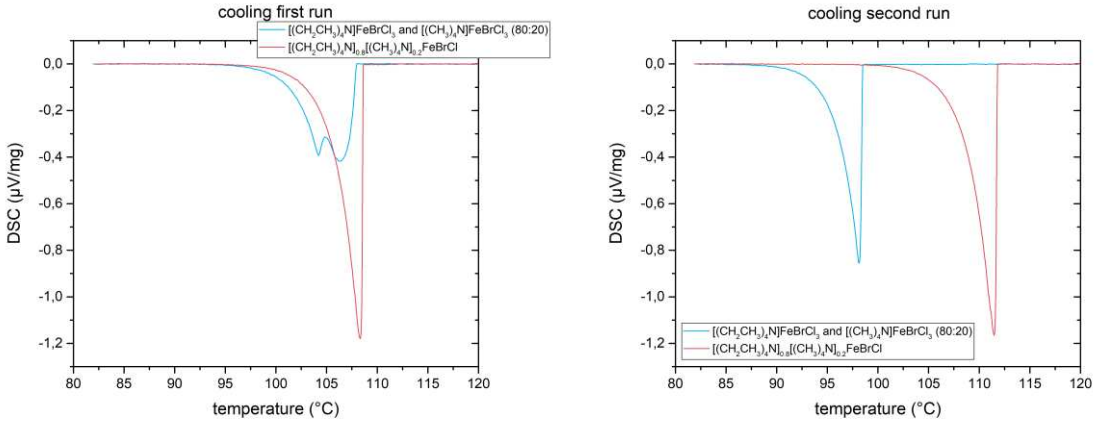

(a) (b)

Figure 51: DSC plot of $[(CH_2CH_3)_4N]_{0.8}[(CH_3)_4N]_{0.2}[FeBrCl_3]$ compared to a physical mixture of $[(CH_3)_4N][FeBrCl_3]$ and $[(CH_2CH_3)_4N][FeBrCl_3]$ in the same ratio, upon cooling on the first (a) and second (b) run.

$[(CH_2CH_3)_4N]_{0.8}[(CH_3)_4N]_{0.2}[FeBrCl_3]$ had only one very distinctive peak on heating and cooling for both the first and second run, as seen in Figure 50 and 51. The phase transition upon heating dropped from 152 °C to 150 °C between first and second run while increasing from 108 °C to 112 °C upon cooling.

Both phase transitions of $[(CH_2CH_3)_4N][FeBrCl_3]$ and $[(CH_3)_4N][FeBrCl_3]$ could be seen in the sample containing the physical mixture. In the first heating cycle the peak at 112 °C belonged to $[(CH_3)_4N][FeBrCl_3]$, and fit almost perfectly to a separately measured sample of $[(CH_3)_4N][FeBrCl_3]$. $[(CH_2CH_3)_4N]_{0.8}[(CH_3)_4N]_{0.2}[FeBrCl_3]$ did not have a corresponding peak at the same position, indicating that only small amounts of the *Amm2*-structure were present. The system is sensitive enough to detect the phase transition of the $[(CH_3)_4N][FeBrCl_3]$-rich phase even if it only accounts for 20 % of the overall composition, because it could be detected in the physical mixture.

Two overlapping peaks were also visible upon cooling of the physical mixture, both happening at 105 °C. At this temperature $[(CH_3)_4N][FeBrCl_3]$ transitioned back to the low temperature *Cmcm* phase.[6] The phase transition of $[(CH_2CH_3)_4N][FeBrCl_3]$ should happen at much higher temperatures, but was probably supercooled and initiated by the other phase transition.

The area of the peak of $[(CH_3)_4N][FeBrCl_3]$ upon heating was much smaller compared to $[(CH_2CH_3)_4N][FeBrCl_3]$. On the cooling part of the cycle, the peaks seemed to be roughly of the same size. This could mean that more of the $[(CH_3)_4N][FeBrCl_3]$-structure was formed at elevated temperatures. It could be assumed that the pure components reacted at elevated

temperatures, which also explains the shift and overlap of the peaks upon heating on the second run performed. When being cooled down, there was only one distinctive peak, lower than on the first run and lower than $[(CH_2CH_3)_4N]_{0.8}[(CH_3)_4N]_{0.2}[FeBrCl_3]$. This confirms that the synthesized materials reacted at elevated temperatures, making it important to take previous temperature changes into account. The difference in the position, shape and number of peaks also proved the partial formation of a solid solution of $[(CH_2CH_3)_4N]_{0.8}[(CH_3)_4N]_{0.2}[FeBrCl_3]$.

$[(CH_2CH_3)_4N]_{0.2}[(CH_3)_4N]_{0.8}[FeBrCl_3]$ had two peaks upon heating, corresponding to the phase transitions of the $[(CH_3)_4N][FeBrCl_3]$- and $[(CH_2CH_3)_4N][FeBrCl_3]$-rich phases, as seen in Figure 52a. Similar peaks were observed for the physical mixture of $[(CH_2CH_3)_4N][FeBrCl_3]$ and $[(CH_3)_4N][FeBrCl_3]$. The relative area of the peaks is very different though, suggesting that the ratio of $[(CH_3)_4N][FeBrCl_3]$- and $[(CH_2CH_3)_4N][FeBrCl_3]$-rich phase had been shifted towards larger amounts of $[(CH_2CH_3)_4N][FeBrCl_3]$-solid solution in $[(CH_2CH_3)_4N]_{0.2}[(CH_3)_4N]_{0.8}[FeBrCl_3]$.

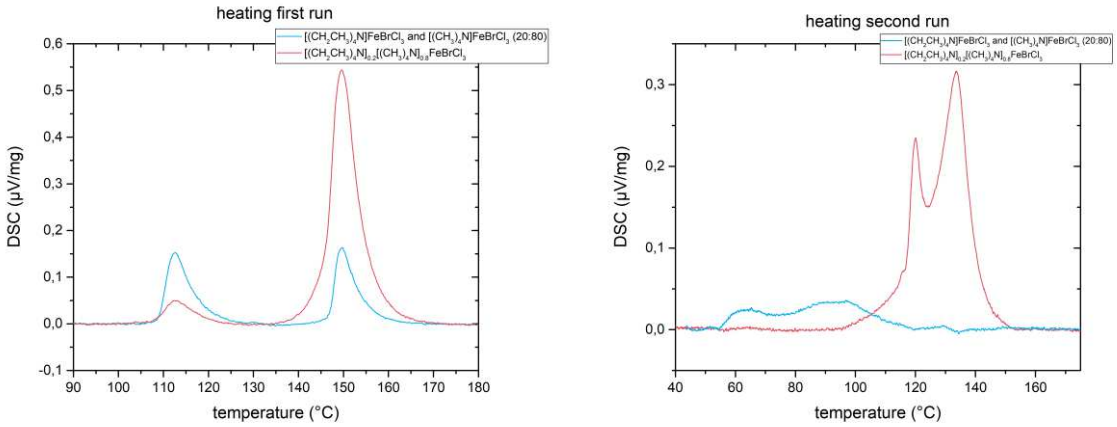

(a) (b)

Figure 52: DSC plot of $[(CH_2CH_3)_4N]_{0.2}[(CH_3)_4N]_{0.8}[FeBrCl_3]$ compared to a physical mixture of $[(CH_3)_4N][FeBrCl_3]$ and $[(CH_2CH_3)_4N][FeBrCl_3]$ in the same ratio, upon heating on the first (a) and second (b) run.

Both samples changed significantly on the second heating cycle. $[(CH_2CH_3)_4N]_{0.2}[(CH_3)_4N]_{0.8}[FeBrCl_3]$ had a phase transition at 120 °C and 133 °C, both very different from the phase transitions at 112 °C and 150 °C on the first run. The physical mixture containing 20 % $[(CH_2CH_3)_4N][FeBrCl_3]$ and 80 % $[(CH_3)_4N][FeBrCl_3]$ had two very broad and overlapping peaks, corresponding to two phase transitions at lower temperatures. No phase transition was recorded down to 80 °C when cooling the physical mixture back down to room

temperature. This observation proves that the thermal history of a sample might greatly influence its properties.

5.3. Electrical properties

Ferroelectric hysteresis, electrical conductivity, dielectric spectroscopy and piezoelectric electromechanical measurements were conducted on each composition of the solid solution to observe the relationship between composition and functional properties. The end members of the solid solution $[(CH_3)_4N][FeBrCl_3]$ and of $[(CH_2CH_3)_4N][FeBrCl_3]$ are ferroelectric and piezoelectric respectively, while all compositions will exhibit a characteristic dielectric response and electrical conductivity, which is why these measurements were chosen for the study. The aim of the electrical measurements was to identify trends as a function of composition and suggest compositional regions of the phase diagram that may be of interest for further investigation.

5.3.1. Hysteresis behavior of $[(CH_3)_4N][FeBrCl_3]$

Polarization – electric field (P-E) loops were obtained from a range of samples of different compositions and synthesis routes in order to identify compositions that were ferroelectric and how the synthesis influenced this property. The electric field hysteresis loop shape provides a fingerprint of the ferroelectric behavior of a material for both quantitative and qualitative analysis of the ferroic response.

First, two different samples of $[(CH_3)_4N][FeBrCl_3]$, prepared by the slow and fast crystallization method, were measured using the same measurement conditions. The results can be seen in Figure 53 and Figure 54.

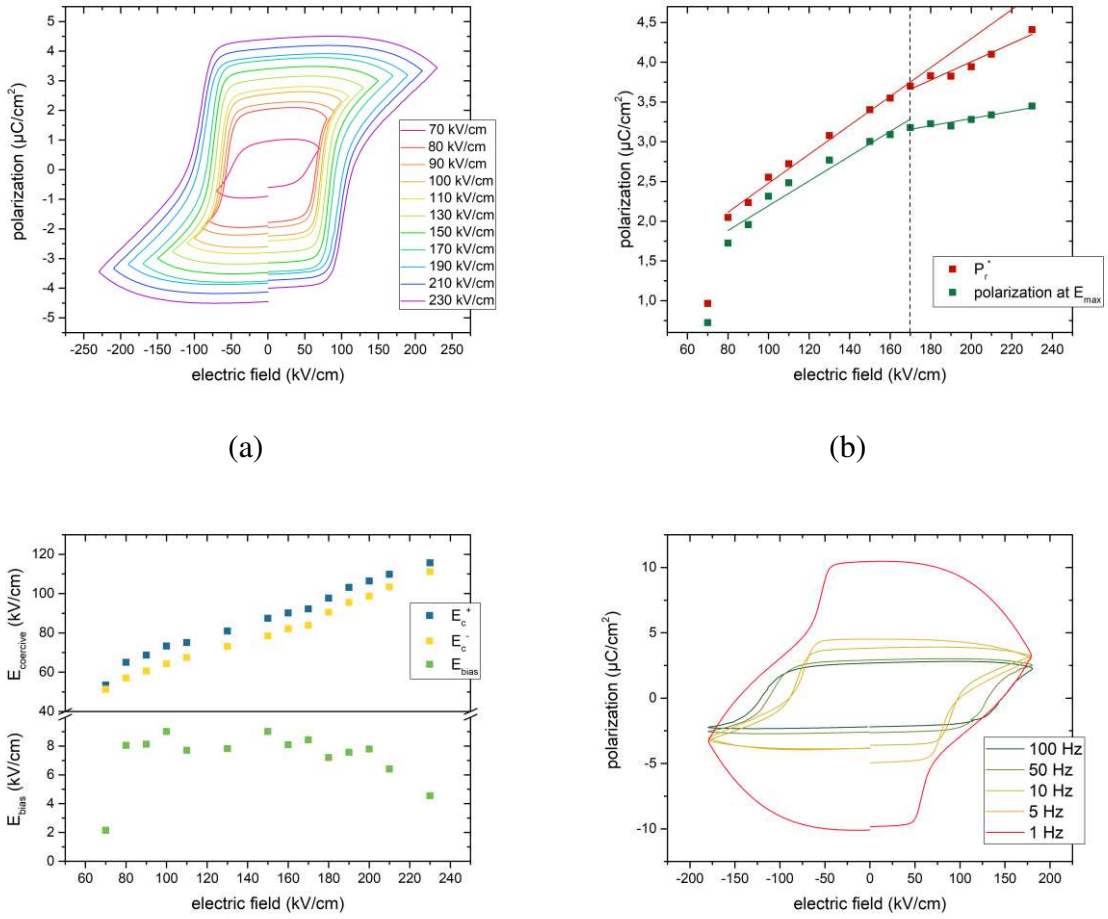

Figure 53: (a) Polarization-electric field loops of $[(CH_3)_4N][FeBrCl_3]$ (fast crystallization in rotary evaporator) at different maximum fields from 70-230 kV/cm. (b) Apparent remanent polarization P_r^* and polarization at E_{max} as a function of the maximum electric field applied. (c) Coercive filed E_c and bias of the coercive field E_{bias} as a function of the maximum electric field applied. (d) Polarization-electric field loops of $[(CH_3)_4N][FeBrCl_3]$ at different frequencies at 180 kV/cm maximum electric field.

Figure 53a - d shows data from hysteresis measurements conducted with electric fields between 70 and 230 kV/cm for the crystals produced by fast crystallization. At 70 kV/cm the polarization – electric field loop already showed clear hysteresis indicative of ferroelectric polarization switching in the material (Figure 53a). A large increase in polarization at 80 kV/cm marked the threshold field necessary to induce significant amounts of domain switching. The loops continued to open gradually with increasing electric fields up to 230 kV/cm, remaining square, consistent with a strong ferroelectric response, with only minor signs of electrical leakage near the maximum electric field points of each field cycle. The polarization remained very stable in each cycle while the electric field was reducing from the maximum or minimum back to zero. This resulted in high values for the remanent polarization (P_r), which is the

polarization measured when the electric field is 0 kV/cm. The maximum field amplitude of 230 kV/cm was the maximum field that could be applied by the experimental setup.

The remanent polarization is often used to quantify the ferroelectric properties of a material and is a measure of how many ferroelectric and ferroelastic domains remain aligned after the electric field has been removed. However, leakage currents can also contribute to the P_r and artificially increase this value. The apparent remanent polarization P_r^* combines the effects that ferroelectric, ferroelastic domains and leakage have on the polarization. Polarization at the maximum electric field should be higher than the P_r as it contains contributions from all switched domains and the dielectric polarization of the material (usually a much smaller contribution). Back switching of unstable domains as the electric field is reduced usually causes the P_r to be lower than the polarization at E_{max}. As a result, comparing the polarization at maximum electric field and the remanent polarization together can provide insight into the amount of domain back switching and leakage current contributions, hence Figure 53b plots these two values as a function electric field amplitude. Polarization remained very stable while reducing the electric field. The behaviour of both remanent polarization and polarization at maximum field were similar as a function of electric field, with the P_r^* being moderately higher, which indicated a small contribution from electrical leakage to the hysteresis loop and likely very little domain back switching. This meant that the switched domains were stable. P_r^* increased almost linearly up to 230 kV/cm with a maximum remanent polarization of 4.41 $\mu C/cm^2$. The polarization at maximum electric field increased linearly up to about 170 kV/cm, before continuing in a linear fashion, but with a smaller slope. The change in gradient likely reflects that fewer new domains were switched with each field increase beyond 170 kV/cm and thus there was a kind of saturation of domain switching. The different trend of P_r and P_r* as a function of electric field was caused by the leakage current that becomes larger at high fields.

The coercive field (E_c) is the field that needs to be applied to bring the polarization down to zero once a material has been poled in the opposite direction (Figure 53c). E_c increased linearly with increasing field strength. At a maximum field of 230 kV/cm, the coercive field was 115 kV/cm. It could be measured on both sides of the hysteresis loop and is equal and opposite in an ideal ferroelectric. The difference between E_c in positive and negative electric field directions is said to be the result of internal electric fields within the material usually caused by oriented charged defects and is called the internal bias electric field (E_{bias}). $[(CH_3)_4N][FeBrCl_3]$ had a bias towards E_c^+, meaning that the coercive field in the positive

direction was slightly higher than in the negative one. It was about 8 kV/cm for fields of 80-210 kV/cm. At very high fields, the bias decreased slightly, going down to about 5 kV/cm at 230 kV/cm. Point defects like $V^{\bullet}_{[FeBrCl3]}$ and $Br^{'}_{[FeBrCl3]}$ could form a complex in the $[(CH_3)_4N][FeBrCl_3]$ lattice. These defects could be oriented preferentially while the samples were pressed. A decrease of the E_{bias} at high fields could indicate that the defect orientation was mobile under high electric fields.

Lastly, a measurement at different frequencies (1-100 Hz) was conducted at 180 kV/cm (Figure 53d). The apparent remanent polarization as well as the coercive field increased with decreasing frequency, while the polarization at the maximum electric field applied remained stable. Frequencies down to 5 Hz resulted in a relatively stable ferroelectric hysteresis loop. At 1 Hz, leakage contributions made up a large part of the loop. This measurement showed that ferroelectric switching occurred at frequencies up to 100 Hz and possibly even higher.

The current density of the samples was measured simultaneously to the polarization and revealed the expected shape typical for a ferroelectric (Figure 54a). When increasing the electric field from zero there was a maximum in the current density at the point at which the bulk of the domains are switched, which corresponded with the coercive field. With ferroelectrics with high electrical leakage currents there is usually a second current peak at the maximum and minimum electric fields caused by non ohmic contributions to electrical conductivity. This effect was absent from the fast crystallized $[(CH_3)_4N][FeBrCl_3]$.

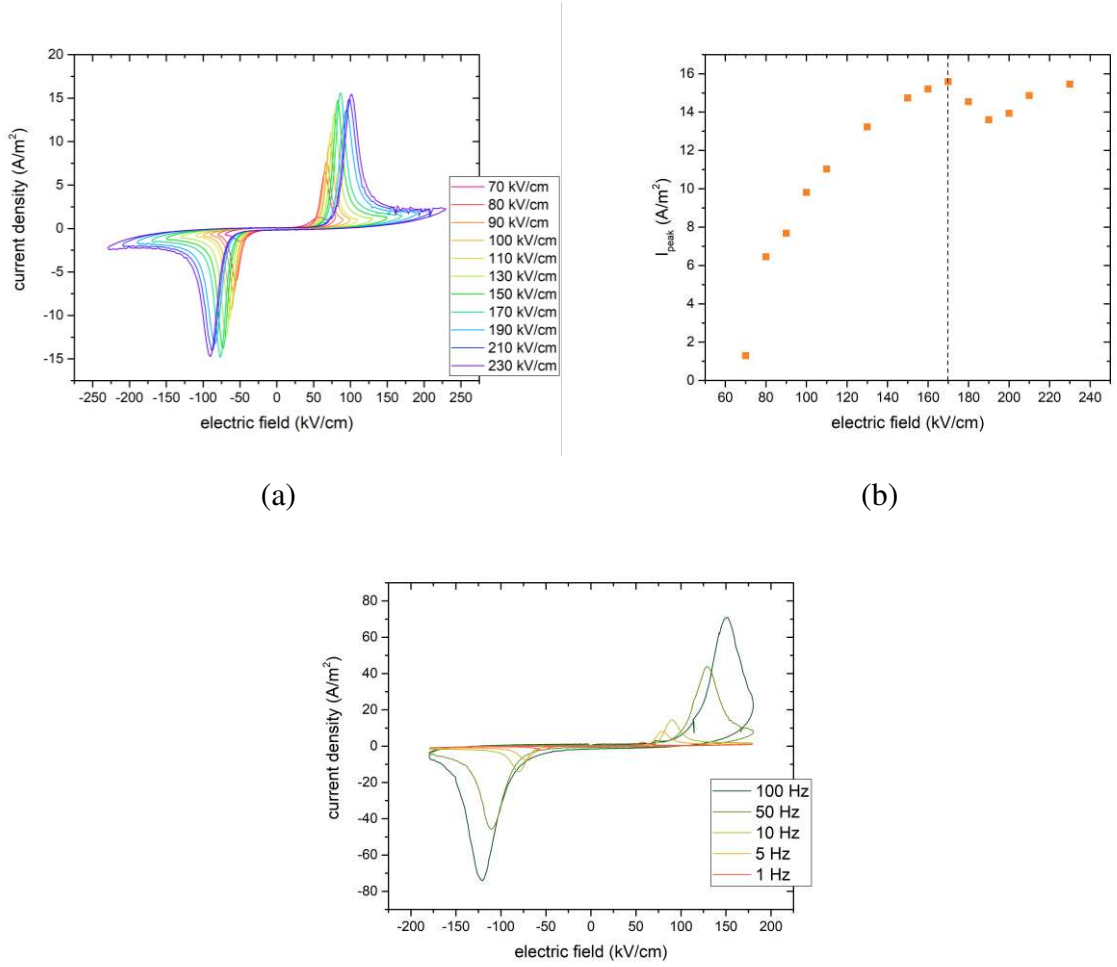

(a) (b)

(c)

Figure 54: (a) Current density-electric field loops of $[(CH_3)_4N][FeBrCl_3]$ (fast crystallization in rotary evaporator) at different maximum fields from 70-230 kV/cm. (b) Peak current density I_{peak} as a function of the maximum electric field applied. (c) current density-electric field loops of $[(CH_3)_4N][FeBrCl_3]$ at different frequencies at 180 kV/cm maximum electric field.

The maximum current density achieved in one loop, I_{peak}, is the most important parameter that can be extracted from this measurement as it reflects the charge produced during domain switching. It is plotted in Figure 54b where the positive maximum of the loop is shown. It increased up to 16 A/m^2 at 170 kV/cm and higher, but dropped down to 13.5 A/m^2 at 190 kV/cm.

The frequency dependent study (Figure 54c) at 180 kV/cm shows that the peak current density increased with the frequency. When comparing this Figure to Figure 53d, the peak occurred at the point of strong change in polarization, which happened at lower electric fields for low frequencies.

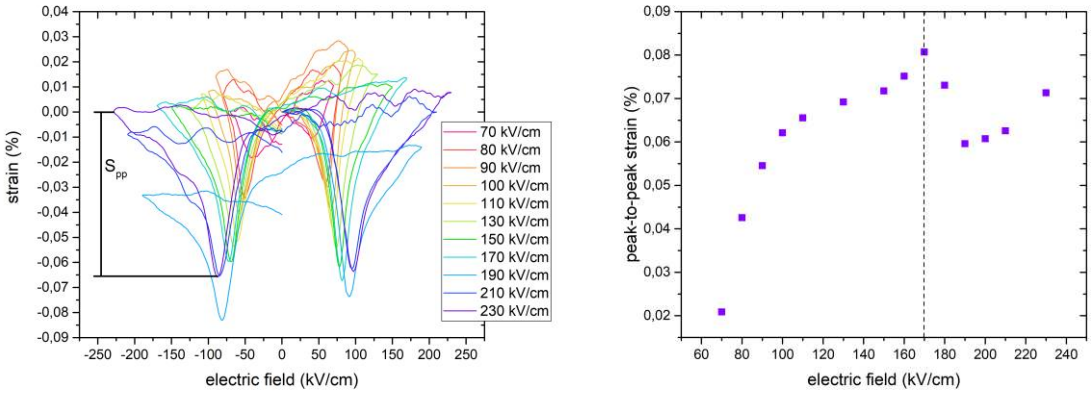

(a) (b)

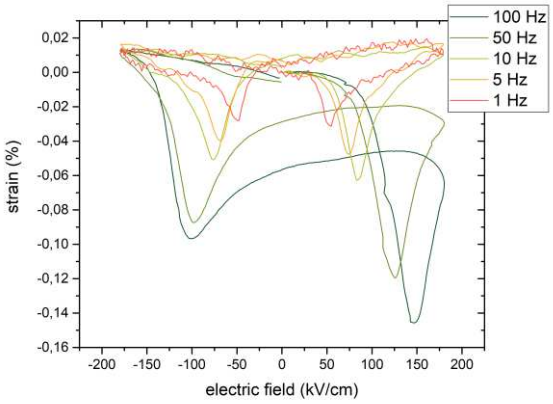

(c)

Figure 55: (a) Strain-electric field loops of $[(CH_3)_4N][FeBrCl_3]$ (fast crystallization in rotary evaporator) at different maximum fields from 70-230 kV/cm. (b) Peak-to-peak strain (S_{pp}) as a function of the maximum electric field applied. (c) strain-electric field loops of $[(CH_3)_4N][FeBrCl_3]$ at different frequencies at 180 kV/cm maximum electric field.

Lastly, the strain was measured by laser interferometry simultaneously as the polarization and current during electric field application. The butterfly-shaped curve of the polarization loop once again is typical for a ferroelectric (Figure 55a). Strain occurs during the application of electric field to the ferroelectric due to three main factors. Firstly the reorientation of ferroelastic (non 180°) domains, secondly due to domain wall movement, and thirdly due to the converse piezoelectric effect.[19] Starting from an arbitrary zero position, the crystal seemingly contracts due to the converse piezoelectric effect when a field is applied. At the point at which the applied field is strong enough to induce domain switching the lattice starts to expand. The strain tapers off towards the maximum applied field once switching saturation occurs. Upon reversal of the field, the strain is being reduced, and, once the field in the opposite direction is big enough, causes the lattice to contract again. $[(CH_3)_4N][FeBrCl_3]$ was very stable

in this regard, loosing almost none of its strain until the coercive field is reached. This was in accordance to the P-E loop, in which the polarization did not decrease until the field is already reversed.

One of the characteristic values obtained from strain-loops was the peak-to-peak strain S_{pp}, which is plotted in Figure 55b for different electric fields. It followed a similar pattern as the peak current density, reaching its maximum strain at 0.08 % at 170 kV/cm. The strain at higher fields was slightly lower.

The peak-to-peak strain was also affected by the frequency of the measurement. At 180 kV/cm, the strain achieved at 1 Hz is about 0.4 % and increased to about 0.11 % at 100 Hz. The butterfly-shaped strain-loops became asymmetrical at high frequencies, this indicated the frequency dependence of domain switching in the materials showing that at 100 Hz the rate of field increase was too fast for the domain switching to keep up, thus the domains did not have time to reverse during the application of bipolar electric fields.

The same measurements were conducted on a slowly crystallized sample of the same composition, $[(CH_3)_4N][FeBrCl_3]$, to investigate the effect of crystallization rate on the electrical properties. The results can be seen in Figure 56-58.

This sample also had typical ferroelectric properties based on the polarization – electric field (P-E) loop, as seen in Figure 56a. The bloated shape was different to the fast crystallization method, indicating different electrical behavior, especially at high fields. The polarization continued to increase after the maximum electric field was reached, which is caused by leakage current.[37] Since the sample was thinner than the one made by fast crystallization, higher electric fields (260 kV/cm) could be applied before reaching the limit of the experimental setup without any degradation.

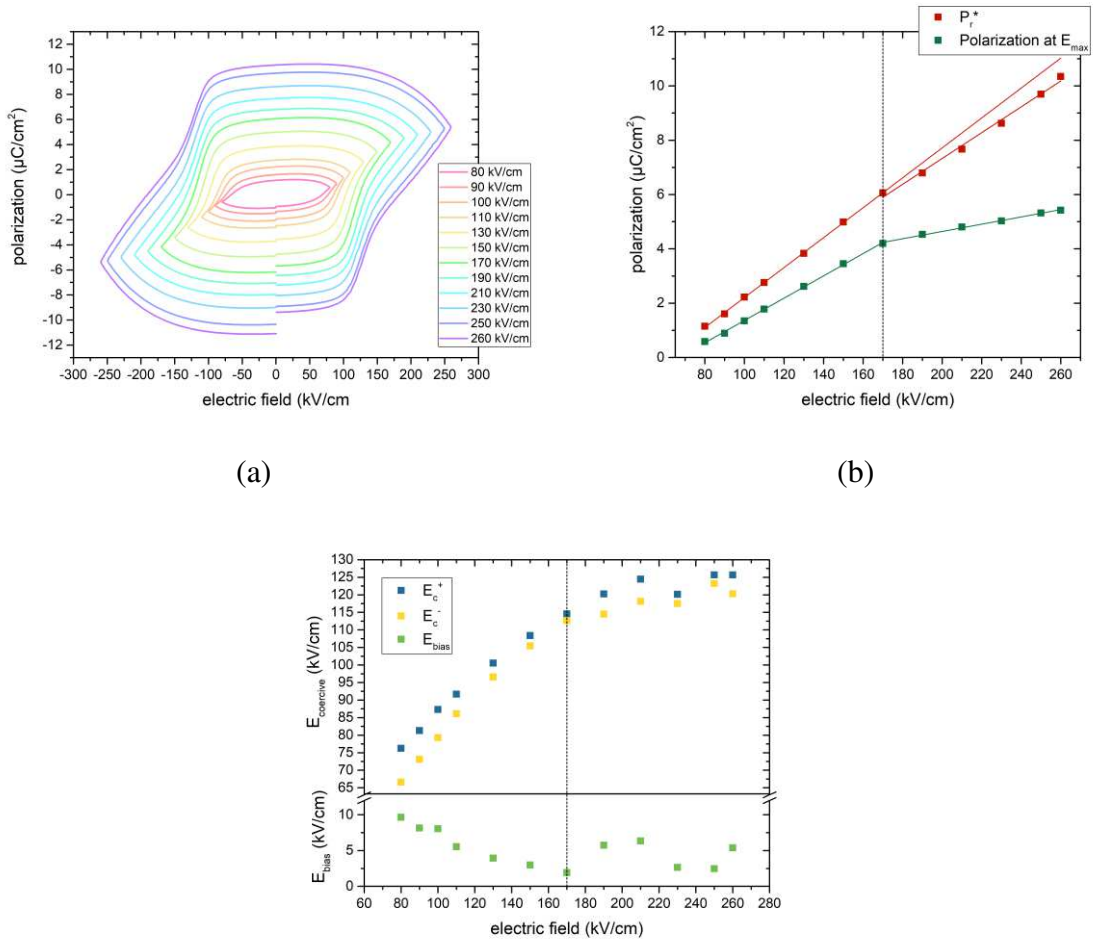

Figure 56: (a) Polarization-electric field loops of $[(CH_3)_4N][FeBrCl_3]$ (slow crystallization through evaporation at room temperature) at different maximum fields from 80-260 kV/cm. (b) Apparent remanent polarization P_r^* and polarization at E_{max} as a function of the maximum electric field applied. (c) Coercive filed E_c and bias of the coercive field E_{bias} as a function of the maximum electric field applied.

The hysteresis loop opened up with increasing electric field, resulting in a P_r^* of 10 µC/cm^2 at the maximum field, which was about twice as much as the sample crystallized quickly. Having a remanent polarization value higher than the polarization at maximum electric field was an indicator for a leaky ferroelectric. The difference between P_r^* and the polarization at E_{max} was more pronounced in the slowly crystallized sample, suggesting that this synthesis route caused more leakage in the final product. By investigating both the P_r^* and the polarization at E_{max}, plotted in Figure 56b as a function of the driving electric field, one can see a change in the behavior of the sample at 170 kV/cm, indicating switching saturation, similar to the quickly crystallized sample.

The gradient of the coercive field also changed at 170 kV/cm, visualized in Figure 56c. E_{bias} decreased linearly from 10 – 2 kV/cm up to 170 kV/cm applied field, with E_c^+ being larger than E_c^-. Having a bias at low fields could be explained by oriented defect complexes. Possible charged point defects of $V^{\bullet}_{[FeBrCl3]}$ and $Br^{'}_{[FeBrCl3]}$ could form a complex in $[(CH_3)_4N][FeBrCl_3]$, as previously identified. A preferred orientation of these complexes could be induced by the slow crystallization of the sample or the pressing into disks. Due to fact that the E_{bias} decreased to almost zero at 170 kV/cm, it was most likely that the defects were mobile at higher fields.

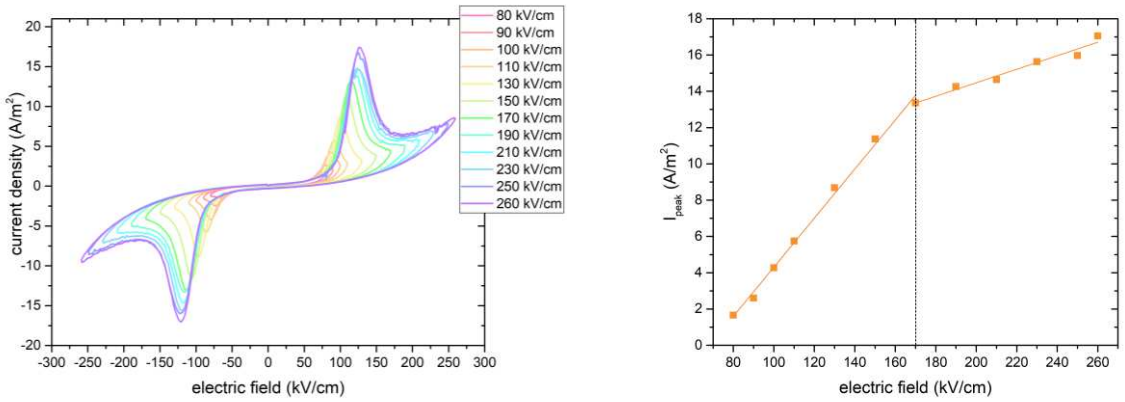

(a) (b)

Figure 57: (a) Current density-electric field (I-E) loops of $[(CH_3)_4N][FeBrCl_3]$ (slow crystallization through evaporation at room temperature) at different maximum fields from 80-260 kV/cm. (b) Peak current density I_{peak} as a function of the maximum electric field applied.

Information about the switching behavior of the domains and leakage current could be obtained from plots of the current density as a function of the electric field (I-E loops), as seen in Figure 57.[37,38]. After the maximum current peak there was another increase at the maximum and minimum applied field, a sign of leakage current. When plotting the peak current density I_{peak} against the applied electric field for each cycle (Figure 57b), one can see a change in the behavior of the sample at 170 kV/cm. The increase in I_{peak} after 170 kV/cm was smaller compared to lower fields because once the field strength was high enough to induce complete switching, any additional current that was measured belonged only to leakage contributions.

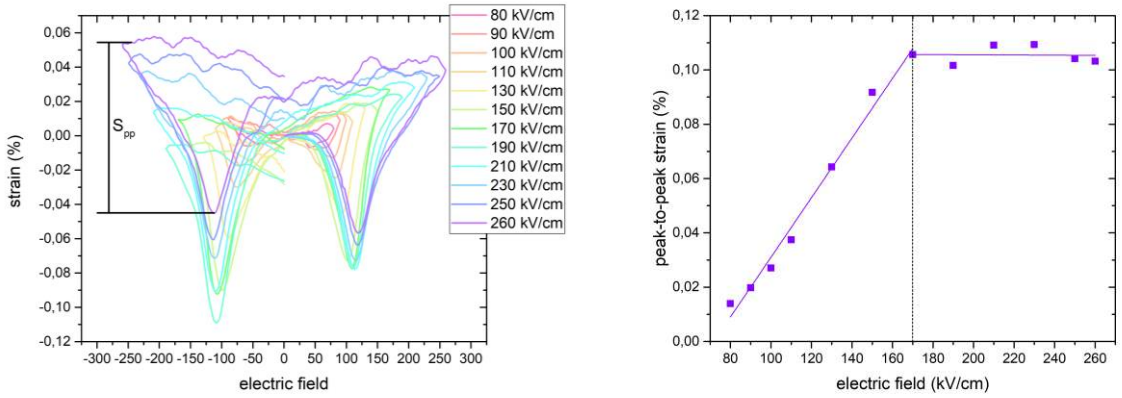

(a) (b)

Figure 58: (a) Strain-electric field loops of $[(CH_3)_4N][FeBrCl_3]$ (slow crystallization through evaporation at room temperature) at different maximum fields from 80-260 kV/cm. (b) Peak-to-peak strain (S_{pp}) as a function of the maximum electric field applied.

The strain of the sample was measured using optical laser interferometry, resulting in a strain-electric field hysteresis (S-E) loop, as seen in Figure 58. Showcasing a butterfly-shaped loop, typical for a ferroelectric, a maximum peak-to-peak strain (S_{pp}) of up to 0.109 % at 10 Hz could be achieved at fields upwards of 170 kV/cm. This value was about 36 % higher than the strain of the quickly crystallized sample. The strain was caused by ferroelastic domain switching, domain wall motion, piezoelectric response and electrostriction.[39,38] E_c could be identified from the minimum in the S-E loop, and matched up with the findings from the I-E measurements. While removing the electric field, the strain of the sample remained very stable. Up to 170 kV/cm, the peak-to-peak strain follows a linear pattern with increasing electric field, as seen in Figure 58b. Once the switching saturation was reached, no further strain could be induced, and the value remained constant. In contrast to the other characteristic values, which had a different slope above 170 kV/cm, but still increased, the strain values reached a plateau. This is caused the fact that electrical leakage does not directly contribute to the train measurements, thus the plateau reflects the main strain contributing factors, that is, the domain switching and indicates that an approximate saturation in the number of domains being switched is reached.

The comparison of $[(CH_3)_4N][FeBrCl_3]$ revealed higher leakage currents in the slowly crystallized material reflected in the polarization and current measurements and also slightly larger S_{pp} seen in the strain loops. High leakage was likely caused by a larger amount of moisture present in the material, trapped inside the larger crystal agglomerates. One possible explanation for the larger strain could be that high leakage currents aided the switching of

domains and thus helped produce larger strains during the switching, but this hypothesis was not supported in the literature and requires further study to verify. Table 3 compares the most important parameters of $[(CH_3)_4N][FeBrCl_3]$ at 230 kV/cm, synthesized at different crystallization rates.

Table 3: Comparison of important electrical parameters of $[(CH_3)_4N][FeBrCl_3]$ at 230 kV/cm, synthesized at different crystallization rates.

	fast crystallization	slow crystallization
P_r* ($\mu C/cm^2$)	4.41	8.62
Polarization at E_{max} ($\mu C/cm^2$)	3.45	5.03
E_c (kV/cm)	116	120
I_{peak} (A/m^2)	15.5	15.6
S_{pp} (%)	0.071	0.103

5.3.2. Hysteresis behavior of $[(CH_2CH_3)_4N][FeBrCl_3]$

A pressed sample of $[(CH_2CH_3)_4N][FeBrCl_3]$ showed very different polarization behavior from $[(CH_3)_4N][FeBrCl_3]$. Firstly, we knew from the wurtzite crystal structure that the material should not be ferroelectric and therefore should not exhibit a square hysteresis loop. This was indeed the case (Figure 59). The polarization loop showed no sign of ferroelectric like hysteresis and instead was very bloated and round, forming a loop that is typical for a high electrical loss dielectric.[40] We note that in this situation the "polarization" arised almost entirely due to electrical leakage current during measurements. The sample underwent dielectric breakdown at electric fields above 100 kV/cm, making it impossible to conduct measurements at higher fields. At higher fields the loops did not start and finish at approximately the same position and this was likely due to large amounts of charge injection during cycling.

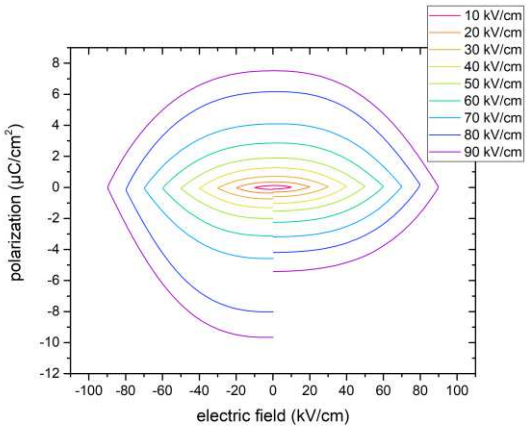

Figure 59: Polarization-electric field loops of [(CH₂CH₃)₄N][FeBrCl₃] at different maximum fields from 10 – 90 kV/cm.

5.3.3. Hysteresis behavior of [(CH₂CH₃)₄N]ₓ[(CH₃)₄N]₁₋ₓ[FeBrCl₃]

Polarization was also investigated on samples made from mixed compositions of [(CH₂CH₃)₄N]ₓ[(CH₃)₄N]₁₋ₓ[FeBrCl₃], as seen in Figure 60. The linear and oval shape of the polarization-electric field (P-E) loops showed no ferroelectric-like hysteresis indicating only a dielectric response with varying amounts of leakage current contribution, depending on the composition. The maximum polarization observed for the mixed compositions was lower compared to [(CH₃)₄N][FeBrCl₃] and [(CH₂CH₃)₄N][FeBrCl₃]. To try to compare the maximum polarizations of each mixed cation composition, the peak to peak polarization at an electric field of 180 kV/cm was plotted as a function of the composition (Figure 61).

As a general observation samples containing a majority of [(CH₃)₄N]⁺-cations had higher leakage current than those containing mostly [(CH₂CH₃)₄N]⁺, which can be seen by the widening of the loop. The maximum polarization decreased slightly with increasing [(CH₃)₄N]⁺-content. At 80 – 90 mol% [(CH₃)₄N]⁺-cations, there was an increase of the maximum polarization, which could be explained by the increased leakage current of these samples.

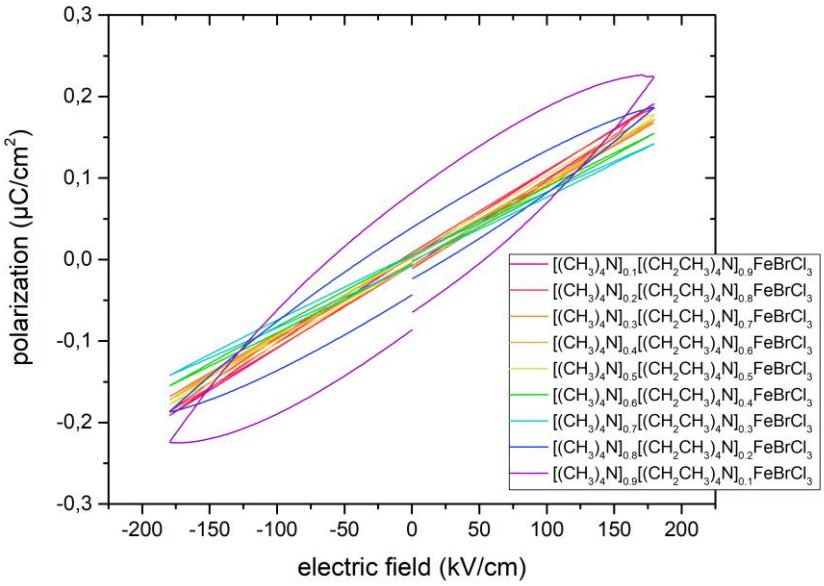

Figure 60: Polarization-electric field (P-E) loops of $[(CH_2CH_3)_4N]_x[(CH_3)_4N]_{1-x}[FeBrCl_3]$ (x = 0.1, 0.2, …0.9) at 180 kV/cm.

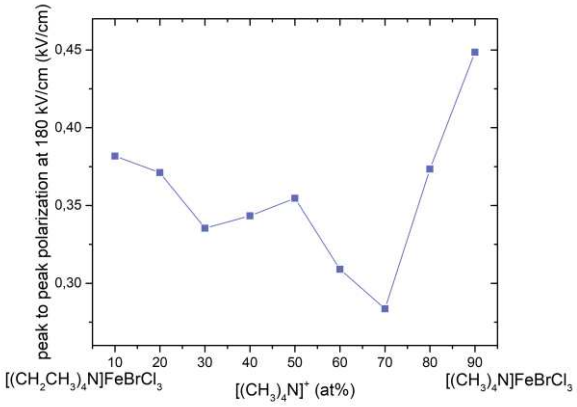

Figure 61: Plot of the peak to peak polarization at 180 kV/cm as a function of the composition of $[(CH_2CH_3)_4N]_x[(CH_3)_4N]_{1-x}[FeBrCl_3]$.

Each sample was exposed to a number of increasing electric fields. An example of this is shown for $[(CH_2CH_3)_4N]_{0.5}[(CH_3)_4N]_{0.5}[FeBrCl_3]$ in Figure 62. The sample had very low leakage, and displayed a strongly linear dielectric behavior even at the maximum field of 260 kV/cm at 10 Hz. This suggests a good, low loss dielectric response. The whole composition range stood up to the maximum electric fields that could be applied for the respective thickness, when being measured at 10 Hz, without any arching. The thinnest sample

($[(CH_2CH_3)_4N]_{0.3}[(CH_3)_4N]_{0.7}[FeBrCl_3]$) could be measured up to 340 kV/cm, where it still showed dielectric behavior with low leakage.

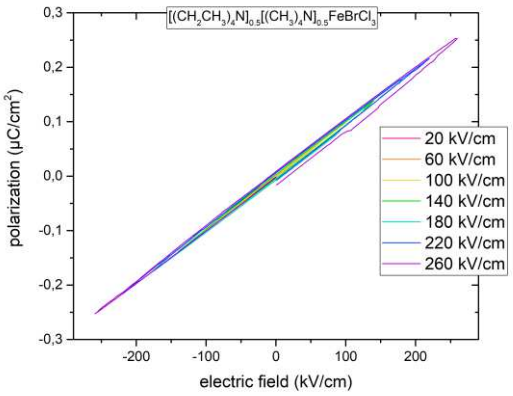

Figure 62: Polarization-electric field loops of $[(CH_2CH_3)_4N]_{0.5}[(CH_3)_4N]_{0.5}[FeBrCl_3]$ at different maximum fields from 20 – 260 kV/cm

This investigation of the $[(CH_2CH_3)_4N]_x[(CH_3)_4N]_{1-x}[FeBrCl_3]$-system showed that none of the samples, excluding $[(CH_3)_4N][FeBrCl_3]$, showed signs of ferroelectric switching. Instead, they all displayed linear dielectric behavior, some with low leakage current that could make them potential alternatives as cheap low capacitance dielectrics. Meanwhile future studies of the ferroelectric response will need to focus on compositions containing more than 90 mol% of the $[(CH_3)_4N]^+$-cation.

5.3.4. Leakage current measurements

Specific leakage current measurements were conducted to quantify the differences in the leakage current observed qualitatively with the hysteresis measurements. They were conducted in a range from ±1 kV/cm to ±10 kV/cm. Figure 63 displays the leakage current density of slowly crystallized $[(CH_3)_4N][FeBrCl_3]$, showing an increase of the current with increasing fields. As with all the other samples, a hysteresis of the current density was apparent while applying and removing the electric field. The values were higher when increasing the field. The median current density is displayed in Figure 64 for each composition of the solid solution system. This was done to simplify representation, and because the hysteresis did not change as a function of the composition. It is clearly visible that all samples follow a similar trend as a function of electric field magnitude on the logarithmic scale, but with different density magnitudes.

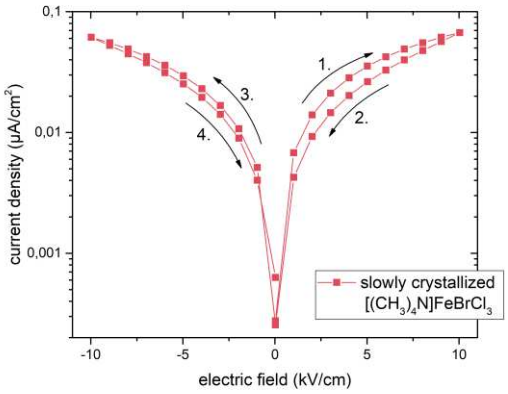

Figure 63: Leakage current measurement of $[(CH_3)_4N][FeBrCl_3]$, slowly crystallized at room temperature for electric fields from ±1 kV/cm to ±10 kV/cm.

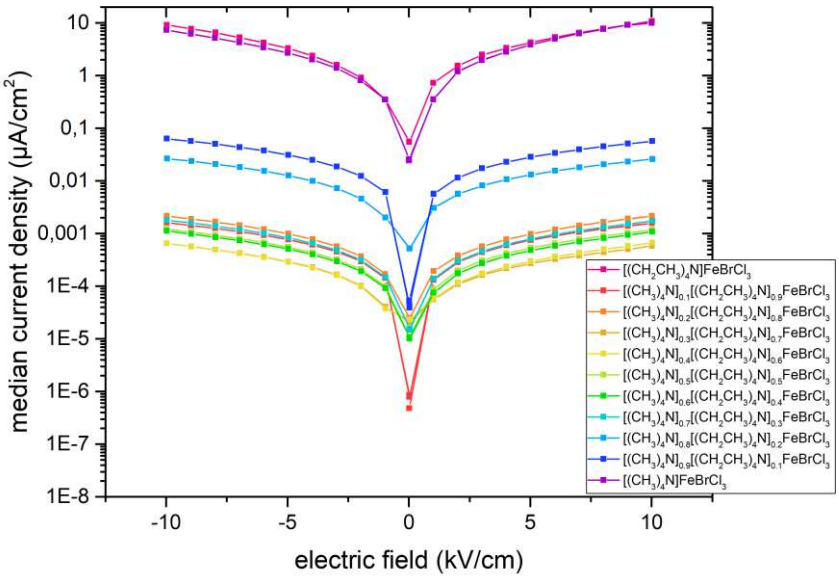

Figure 64: Leakage current measurements of different compositions of $[(CH_2CH_3)_4N]_x[(CH_3)_4N]_{1-x}[FeBrCl_3]$ for electric fields from ±1 kV/cm to ±10 kV/cm.

The median current density of all compositions at an electric field of 10 kV/cm is plotted as a function of composition in Figure 65. A polynomial fit of the fourth order was performed to demonstrate how the current density differs from composition to composition. All mixed compositions $[(CH_2CH_3)_4N]_x[(CH_3)_4N]_{1-x}[FeBrCl_3]$ had a lower current density than $[(CH_3)_4N][FeBrCl_3]$ and $[(CH_2CH_3)_4N][FeBrCl_3]$, which were very similar at about 10 µA/cm^2 at 10 kV/cm. Compositions ranging from $[(CH_2CH_3)_4N]_{0.9}[(CH_3)_4N]_{0.1}[FeBrCl_3]$ to $[(CH_2CH_3)_4N]_{0.3}[(CH_3)_4N]_{0.7}[FeBrCl_3]$ had a median current density of about 0.001 µA/cm^2 at

10 kV/cm, with $[(CH_2CH_3)_4N]_{0.7}[(CH_3)_4N]_{0.3}[FeBrCl_3]$ having the lowest value at $5.8 \cdot 10^{-4}$ µA/cm^2. $[(CH_2CH_3)_4N]_{0.2}[(CH_3)_4N]_{0.8}[FeBrCl_3]$ and $[(CH_2CH_3)_4N]_{0.1}[(CH_3)_4N]_{0.9}[FeBrCl_3]$ had higher values at 0.01 – 0.1 µA/cm^2 at the same electric field. These were also the compositions that stood out, when looking at the structural data of the composition range. Electrical properties are highly affected by compositional changes. Binary metal alloys display a similar behavior to the one presented here. This theory works under the assumption of limited solubility and the formation of a mechanical mixture of the two structures.[41]

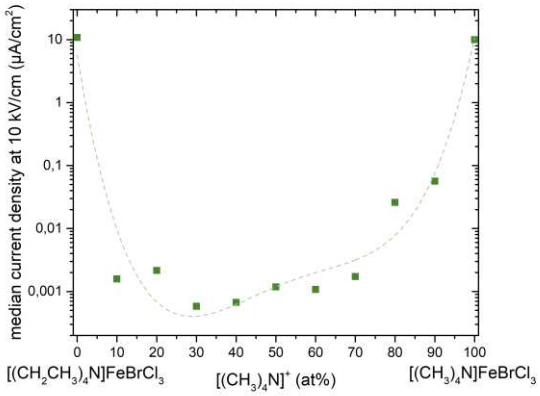

Figure 65: The median current density at 10 kV/cm as a function of the composition of the sample.

The current density measured on the slowly crystallized sample of $[(CH_3)_4N][FeBrCl_3]$, displayed in Figure 63, was more than two orders of magnitude lower than a sample of the same composition, crystallized in a rotary evaporator. This could be related to the size of the crystals that were pressed together during hot pressing or the number of defects caused by crystallizing the composition quickly, grinding it up and pressing it from a powder. Interestingly, however, the trend in leakage currents measured here at a maximum electric field of 10 kV/cm was opposite to that observed during the hysteresis measurements at fields up to 260 kV/cm. This means that even though the slowly crystallized sample had lower leakage at low fields, leakage increased more compared to the quickly crystallized samples at high fields. These potential contributions from nonohmic conductivity mechanisms could be caused by large charged defects, like lattice vacancies, or defect complexes that have a specific activation energy. They are only mobile once a certain threshold is reached. This hypothesis may also be supported by the change in the E_c and E_{bias} at high electric fields.

5.3.5. Piezoelectricity

5.3.5.1. Low field d_{33} measurements

Low field d_{33} measurements of the direct piezoelectric effect were performed on a Berlincourt meter to investigate the piezoelectric response of selected samples. First, single crystals of the piezoelectric, but not ferroelectric end member composition $[(CH_2CH_3)_4N][FeBrCl_3]$ were measured. They grew with two distinctively different shapes which resulted from their growth in different crystallographic directions. Both crystal morphologies were measured to determine the anisotropy of the piezoelectric response. The majority of the crystals grew as a cuboid with chamfered edges, producing values of only -1.1/0.5 pC/N, when measured parallel to the a or b lattice parameter and perpendicular to the surface they grew from. This d_{33} value was likely noon-zero but close to the noise floor of the measurement system. Positive and negative values were obtained by reversing the crystal in the measurement set up. About one third of the crystals grew with a hexagonal shape. This indicated that the polar c-axis was parallel to the direction of growth, and perpendicular to the surface on which the crystals were grown. When measured perpendicular to the c axis a d_{33}-value of about -7/7 pC/N was observed. These d_{33} values exceed the isostructural piezoelectric material aluminum nitride and gallium nitride with values of around 5.1±0.1 and 3.1±0.1 pC/N respectively, and thus may point to some potential application for the plastic crystals.[11] Hexagonal single crystals of the compositions $[(CH_2CH_3)_4N]_{0.9}[(CH_3)_4N]_{0.1}[FeBrCl_3]$ and $[(CH_2CH_3)_4N]_{0.2}[(CH_3)_4N]_{0.8}[FeBrCl_3]$ were also measured, resulting in values of -6.5/5.6 pC/N and -7.6/6.4 pC/N respectively. No other compositions with single crystals of the piezoelectric *P6₃mc*-structure could be grown. No notable piezoelectric response was expected from pressed disks of the mixed compositions, because of their randomly oriented grains. Therefore, no low field d_{33} measurements were performed, except of a sample of slowly crystallized $[(CH_3)_4N][FeBrCl_3]$, which had values of 7.1/-7 pC/N. This measurement was performed on a pressed sample because no suitable single crystals could be produced.

5.3.5.2. High field d_{33} measurements

The high-field (180 kV/cm) measurements were performed as part of the polarization-electric field (P-E) loops on pressed samples by applying unipolar electric field cycles. This additional measurement at high electric fields caused additional extrinsic effects to contribute to the measured strain response, resulting in a nonlinear behavior. Domain wall motion, growth of domains and mobility of defects are more prominent at high fields. Measuring both high and low field d_{33} allowed to determine the role of these different contributions to the strain.[42]

Two different disks of the composition $[(CH_3)_4N][FeBrCl_3]$ were measured, synthesized by slow and fast crystallization methods. The d_{33} of a slowly crystallized sample was about three times as high with about 12 pm/V, compared to the fast crystallization at around 4 pm/V. This shows the significance of the synthesis method and sample preparation for the final properties. The slowly crystallized sample of $[(CH_3)_4N][FeBrCl_3]$ had a low field d_{33} of 7.1/-7 pC/N and a high field value of 12 pm/V, which is almost twice as high. This was the contribution of the effects that were more pronounced at high electric fields, such as domain wall motion, growth of domains and the mobility of defects.

High field measurements of single crystals of the *P6$_3$mc*-structure, that grew from $[(CH_2CH_3)_4N][FeBrCl_3]$, $[(CH_2CH_3)_4N]_{0.9}[(CH_3)_4N]_{0.1}[FeBrCl_3]$ and $[(CH_2CH_3)_4N]_{0.2}[(CH_3)_4N]_{0.8}[FeBrCl_3]$ compositions could not be measured because their physical dimensions do not fit into the experimental setup. The majority of the piezoelectric response of pressed disks of mixed compositions at high fields is an effect of the non-linear extrinsic effects, so they were not investigated thoroughly either.

5.3.6. Dielectric spectroscopy

5.3.6.1. Frequency sweep at room temperature

Dielectric measurements were conducted on samples of the whole composition range. For these, a small alternating current (AC) electric signal (1 V_{rms}) was applied to the samples and the resulting displacement of charge from atoms, ions, dipoles and space charges in the materials were measured. The two main parameters describing dielectrics, the relative permittivity ε_r and the loss tangent tan (δ) were measured as a function of frequency. The dipoles of a dielectric reorient themselves when an external electric field E is applied. The polarization P of the material follows a harmonically oscillating field, though not instantly. At high frequencies (e.g. $>10^7$ Hz), there is not enough time for the material to switch polarization, and no orientation takes place. At low frequencies, on the other hand, the relaxation happens instantly and there is no phase difference between the field applied and the resulting polarization. In a certain range, the frequency is close to the relaxation time, resulting in a maximum of the shift in phase angle δ. The relative permittivity (or dielectric constant) ε_r describes the polarizability of a dielectric, while the loss angle δ is a measure of the energy dissipated. They are both frequency and temperature dependent and no constants, as the name would suggest.[43]

The real part of the relative permittivity and tan (δ) are displayed in Figure 66 and 67 in a frequency range of 0.05-10^6 Hz for all compositions synthesized.

The real part of the permittivity ε' is relatively constant for most compositions across the whole frequency range. Values for all samples, except $[(CH_3)_4N][FeBrCl_3]$ range from 15-20. Samples containing a bigger proportion of $[(CH_2CH_3)_4N]^+$-cations tend to have slightly higher ε'. This trend was also reflected in the polarization values at 180 kV/cm measured during the hysteresis measurement study (Figure 60).

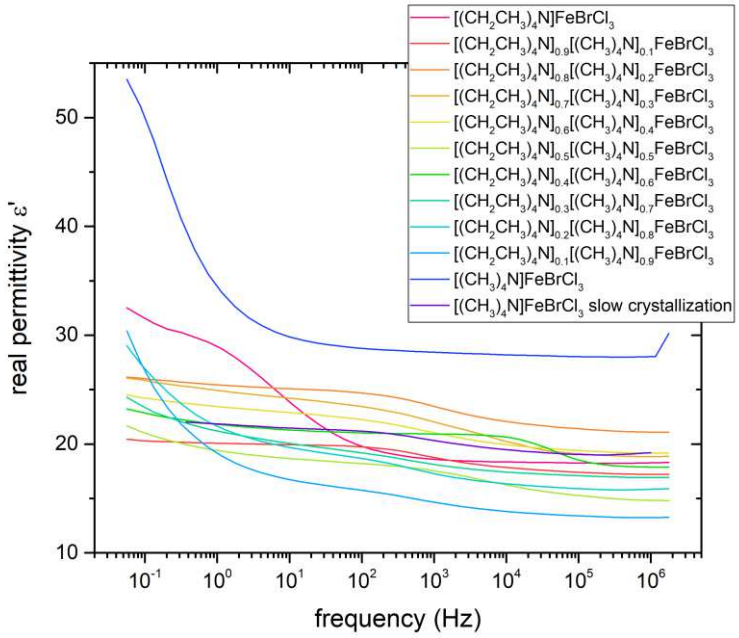

Figure 66: Dielectric measurements of different chemical compositions ($[(CH_2CH_3)_4N]_x[(CH_3)_4N]_{1-x}[FeBrCl_3]$) of the real permittivity ε' as a function of frequency (0.05 - 10^6 Hz) at room temperature.

The loss tangent at the same frequency range (Figure 67) showed a local maximum for most compositions at around 10^3 Hz. The relaxation was most likely related to space charges like defects moving in the material and possibly being pinned at interfaces like grain boundaries.[44] Compositions containing mostly $[(CH_2CH_3)_4N]^+$-cations had an overall lower tan (δ). An explanation for the increase of the loss tangent at low frequencies could be the Maxwell-Wagner polarization, which arises from a built-up of charge at inhomogeneous materials or at interfaces of the measuring setup.[45]

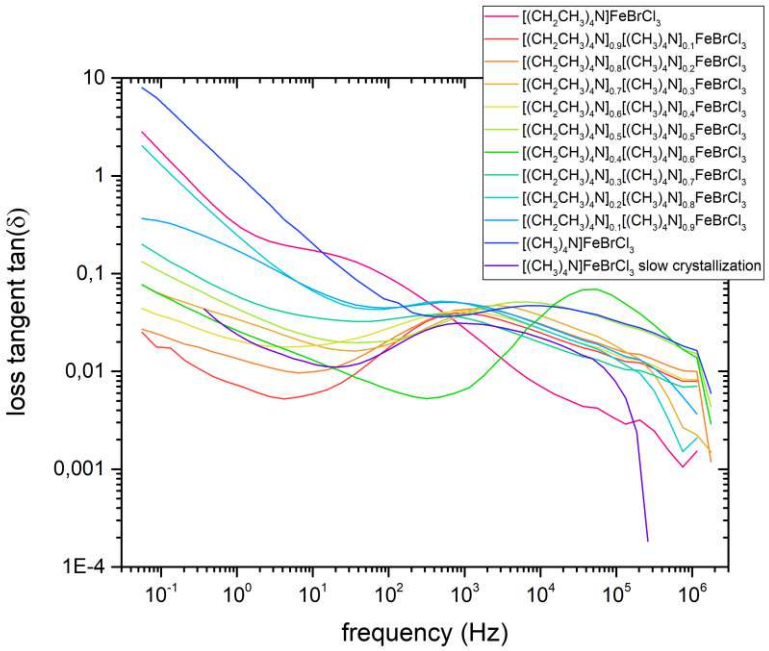

Figure 67: Dielectric measurements of different chemical compositions ($[(CH_2CH_3)_4N]_x[(CH_3)_4N]_{1-x}[FeBrCl_3]$) of the loss tangent tan (δ) as a function of frequency (0.05 - 10^6 Hz) at room temperature.

Some of the samples were measured multiple times to confirm the repeatability of the measurements. The values varied largely, even when only measuring a different fragment of the same pressed sample. It seems like both ε' and tan (δ) depend not only on the compositions of the samples, but also their homogeneity and grain structure, which was difficult to assess quantitatively. Therefore, no clear trend as a function of composition could be detected.

5.3.6.2. Temperature sweep

Both the loss tangent tan (δ) and the real permittivity ε' are temperature dependent. It is common for ferroelectrics to display a strong increase in the permittivity at the Curie temperature at which the phase transitions from the ferroelectric to the paraelectric high temperature phase takes place.[43] To assess the behavior of the dielectric properties at the mesophase transition in theses plastic crystals, the real permittivity ε' and the loss tangent tan (δ) were measured at selected frequencies as a function of temperature. The samples were measured up to 170 °C before cooling them down to room temperature again. Frequencies ranging from 1000-10^6 Hz were measured continuously, meaning there was a slight temperature difference between each frequency, even though all frequencies of one measurement are assigned to a single temperature. The low frequencies were measured first, so that data was obtained at slightly different temperatures than the high frequencies. Only the

heating part of the cycle is displayed below (Figure 68-70). Figures of the cooling part can be seen in the appendix, in section 7.3.

The values for tan (δ) and ε' were higher for lower frequencies, as expected from previous experiments. The low end of the frequencies measured, 1000 Hz, was already higher than the local maxima of ε' and tan (δ), determined in the previous section. The temperature at which the mesophase transition occurred, according to DSC, is marked in the figures. There was an observable anomaly at that temperature in the data observed. The complexity of the peaks in the real permittivity and their imperfect correlation with the phase transitions determined by DSC resulted from the fact that two mesophase transitions of the *Amm2*- and the *P6₃mc*-phase may be present, as well as further complexities arising from the solid solution chemistry. Large differences between heating and cooling (see Appendix) measurements were caused by the hysteresis of the phase transition as well as possible sample and electrode degradation caused by the known corrosivity of $[FeBrCl_3]$ for metals.

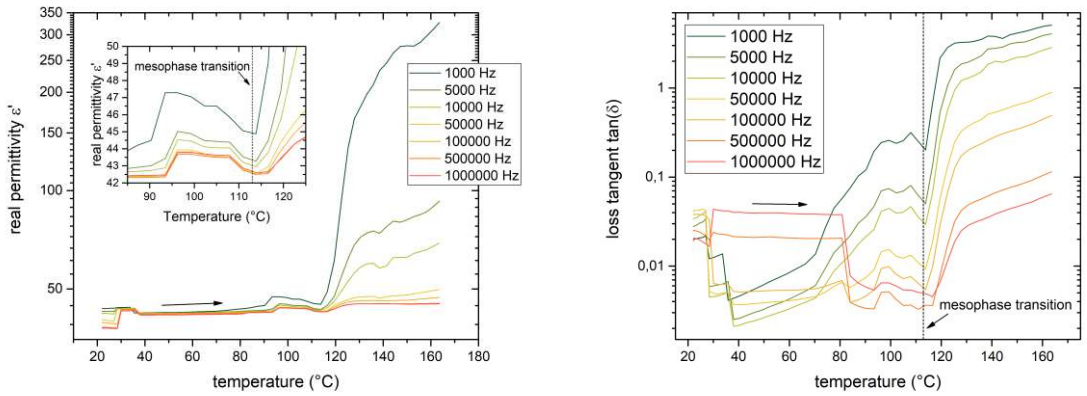

(a) (b)

Figure 68: Dielectric measurements of $[(CH_3)_4N][FeBrCl_3]$, investigating the real permittivity ε' (a) and the loss tangent tan (δ) (b) at different frequencies while heating up the sample from 25 – 170 °C.

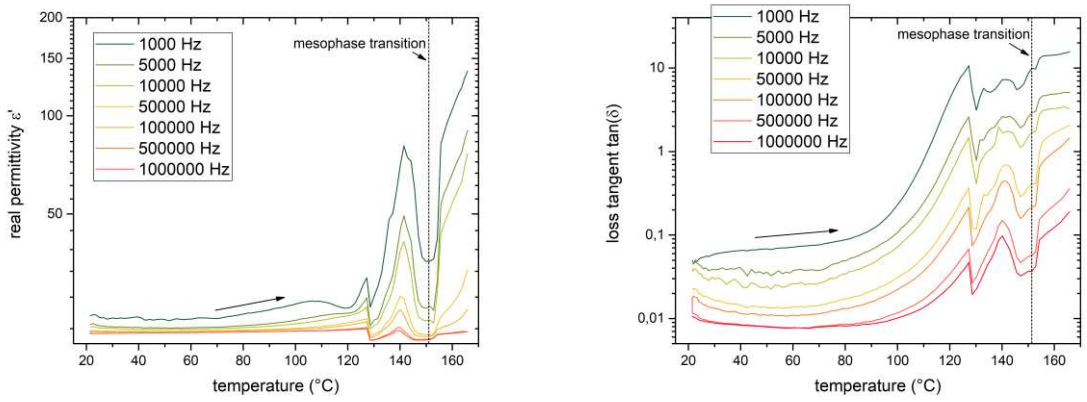

(a) (b)

Figure 69: Dielectric measurements of $[(CH_2CH_3)_4N]_{0.8}[(CH_3)_4N]_{0.2}[FeBrCl_3]$, investigating the real permittivity ε' (a) and the loss tangent tan (δ) (b) at different frequencies while heating the sample from 25 – 170 °C.

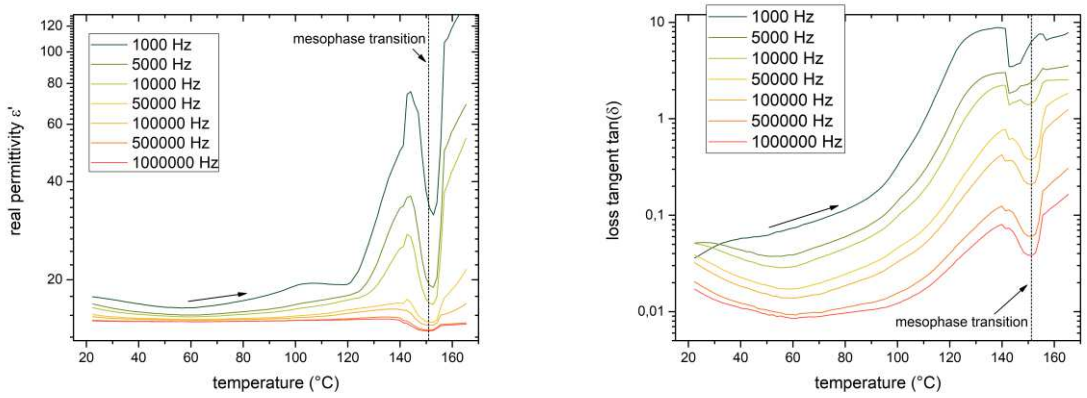

(a) (b)

Figure 70: Dielectric measurements of $[(CH_2CH_3)_4N]_{0.5}[(CH_3)_4N]_{0.5}[FeBrCl_3]$, investigating the real permittivity ε' (a) and the loss tangent tan (δ) (b) at different frequencies while heating the sample from 25 – 170 °C.

The permittivity of all measured samples increased drastically after the phase transition to the plastic mesophase. Multiple other peaks and anomalies were observed, but they were difficult to correlate to any phase transitions. The same trend was visible in the diagram of the tan (δ), where a distinct change in the values coincided with the phase transition obtained from DSC measurements. Samples of $[(CH_2CH_3)_4N]_{0.8}[(CH_3)_4N]_{0.2}[FeBrCl_3]$ (Figure 69) and $[(CH_2CH_3)_4N]_{0.5}[(CH_3)_4N]_{0.5}[FeBrCl_3]$ (Figure 70), which had both been found to be dielectric, had very similar ε' and tan (δ) diagrams. The data for the phase transitions marked in diagrams 68 - 70 were taken from DSC measurements of the as-synthesized powder, before pressing it into disks. It is known that the phase transitions are dependent on the thermal history, meaning

that the phase transitions during the dielectric measurements occurred at different temperatures, possibly explaining the mismatch. The behavior of the samples was not frequency dependent, suggesting that the transitions are of first order, like the Curie transition in a ferroelectric.[46]

Issues with corrosion of the sample holder prevented the investigation of the whole composition range, but the presented results give a good idea of the temperature dependent dielectric properties.

6. Conclusion

Technological advancements in recent decades have been one of the driving forces of research on highly functional materials. Electrical properties like ferro-, piezo-, or dielectric behavior have gained a lot of attention in particular, combined with the goal to develop cheap and environmentally friendly manufacturing methods. This work focuses on investigating the characteristics of a material class that combines electrical properties with plastic formability and an environmentally friendly synthesis route, that is, plastic crystals.

In this work we explore the possibility of engineering new plastic crystals with different ferroic properties by creating a novel solid solution system, $[(CH_2CH_3)_4N]_x[(CH_3)_4N]_{1-x}[FeBrCl_3]$ with two different organic cations with 1+ charge. So far, only the end members of this system have been studied, so the goal was to investigate the entire composition range and determine the synthesis, structural and functional properties. Based on the findings, specific compositions could be selected to be of interest for further investigation.

Synthesis

An evaporation crystallization synthesis method from precursor materials of $FeCl_3 \cdot 6H_2O$, $[(CH_3)_4N]Br$ and $[(CH_2CH_3)_4N]Br$ was performed using solvents water, ethanol or methanol to produce crystals of $[(CH_2CH_3)_4N]_x[(CH_3)_4N]_{1-x}[FeBrCl_3]$ across the entire compositional range from $x = 0 - 1$. SEM and optical microscopy revealed that the morphology of $[(CH_3)_4N][FeBrCl_3]$ and $[(CH_2CH_3)_4N][FeBrCl_3]$ as well as the morphology and crystal structure of $[(CH_2CH_3)_4N]_x[(CH_3)_4N]_{1-x}[FeBrCl_3]$ are influenced by the solvent, an effect that is likely related to its polarity. Based on varying solubility of the precursors and crystal products in solvents, water was chosen as the primary solvent for the synthesis for the comparative study of solution composition range $[(CH_2CH_3)_4N]_x[(CH_3)_4N]_{1-x}[FeBrCl_3]$.

The solution concentration had a profound impact on the crystallization of products and was studied by varying the concentration of the starting solutions and the rate of evaporation

(concentration change) during crystallization. Samples made from highly concentrated solutions precipitated immediately upon mixing, causing small crystals of irregular geometries to form. More diluted starting solutions did not crystallize right away, but later during evaporation. Slow evaporation rates, taking up to 7 days, cause growth of large (up to 10 mm long) single crystals as well as phase separation of the $[(CH_2CH_3)_4N]_x[(CH_3)_4N]_{1-x}[FeBrCl_3]$ composition. Fast evaporation over 30 min on the other hand produced smaller crystals and less pronounced phase separation. This indicated that the two phases present in the system were metastable and thus their presence could be influenced by the synthesis method.

The hygroscopic properties of the precursors made preparing perfect stochiometric ratios difficult, which could introduce defects into the materials. This could be improved by using stock solutions that are analyzed separately, or by quantifying the water uptake.

Structure

The room temperature crystal structures of orthorhombic *Amm2* and hexagonal *P6₃mc* for $[(CH_3)_4N][FeBrCl_3]$ and $[(CH_2CH_3)_4N][FeBrCl_3]$, respectively, were confirmed by powder-XRD. These phases were also identified as the two major, and only phase constituents of the solid solution system $[(CH_2CH_3)_4N]_x[(CH_3)_4N]_{1-x}[FeBrCl_3]$. Some limited site substitution between the organic cations was observed in their reciprocal solvent structures by changes in the lattice parameters and phase weight percentages as a function of composition determined by structure fitting of XRD profiles using Rietveld refinement. It was clearly seen that the phase weight percentages did not change with composition in the same manner as that of a metal solid solution system that obeys the lever rule, providing further evidence that the phase composition was the result of metastability in the system. These observations were confirmed to be related to cation solubility by comparisons with physical mixtures of compositions of the same weight percentages of each end member composition.

Based on the structural fits of *Amm2* and *P6₃mc*, both crystal structures exist simultaneously throughout the whole composition range of $[(CH_2CH_3)_4N]_x[(CH_3)_4N]_{1-x}[FeBrCl_3]$. The crystal structure of $[(CH_3)_4N][FeBrCl_3]$ and $[(CH_2CH_3)_4N][FeBrCl_3]$ can be determined with certainty, whereas the mixed compositions seem to crystallize in a complicated combination of both structures. A solid solution is formed as a kinetically favored metastable phase, based on comparative powder-XRD analysis. Further study with Raman- and infrared-spectroscopy might be useful to further evaluate the structure and molecular interaction in the mixed compositions.

The mesophase transitions were investigated using differential scanning calorimetry (DSC) to shed further light on the influence of compositions in the solid solution. Phase transitions of $[(CH_3)_4N][FeBrCl_3]$ and $[(CH_2CH_3)_4N][FeBrCl_3]$ matched the ones found in literature[6,8], at 113 °C and 153 °C. The temperature of the phase transition associated with the *Amm2* structure did not change as a function of the composition, suggesting that the $[(CH_2CH_3)_4N]^+$-cation had little effect, or solubility was limited. A decrease of the phase transition temperature belonging to the *P6₃mc* structure could indicate more substitution of the $[(CH_3)_4N]^+$-ion, or that the replaced cation had a greater effect on the transition. Large hysteresis of the phase transition could be attributed to the nature of the mesophase transition, increasing with a larger amount of $[(CH_3)_4N]^+$-ion in the system.

Structural changes taking place during the heating cycles caused a shift in the phase transition temperatures between runs, a finding that was confirmed by further powder-XRD studies. Chemical gradients within the materials could promote chemical diffusion at the measurement temperatures (260 °C), reaching within two thirds of the melting temperatures. This hypothesis was further supported by significant changes observed during DSC measurements of physical mixtures of the end members of the $[(CH_2CH_3)_4N]_x[(CH_3)_4N]_{1-x}[FeBrCl_3]$ system. Further information about the phase transitions could be obtained by using a more sensitive instrument that can be cooled down below 0 °C. Calculations of the peak areas visible in the available data may also provide further information about the Gibbs free energies associated with each phase transition.

Further in the structural analysis it was confirmed that structural changes occurred during pressing of the plastic crystals which was performed at 140 °C (some samples at 150 °C) and 1 t for 15 min. Shifts in the lattice parameters and the vanishing of a peak associated with the *Amm2*-structure indicates residual strain and crystallographic orientation. Investigation of this behavior could allow for manipulating crystallographic texturing at low temperatures which could improve the commercial potential of plastic crystals.

Electrical properties

The phase segregation of the system made interpreting the functional properties challenging. Ferroelectric behavior was confirmed for $[(CH_3)_4N][FeBrCl_3]$, in which it was observed that the crystallization method influenced the amount of leakage and possibly the domain switching kinetics, although further studies on this topic are necessary. Polarizations of >4 $\mu C/cm^2$ and peak-to-peak strains of >0.1 % were obtained, while piezoelectric measurements (using a

Berlincourt piezometer) revealed a d_{33} of -7/7 pC/N, and high field measurements a d_{33} of about 12 pm/V. Based on the obtained results, there are possibilities for $[(CH_3)_4N][FeBrCl_3]$ to be used in both ferroelectric and piezoelectric applications. High breakdown strength combined with easy manufacturing of parts and piezoelectric and ferroelectric response could make this material a suitable alternative for some current ceramic-based electronics in specific applications.

P-E loops of $[(CH_2CH_3)_4N][FeBrCl_3]$ reveal that this material behaves like a leaky dielectric. Mechanical breakdown occurred at fields below 100 kV/cm. Hexagonal single crystals of $[(CH_2CH_3)_4N][FeBrCl_3]$ have a high piezoelectric coefficient off -7/7 pC/N when measured with a Berlincourt piezometer. Isostructural piezoelectric AlN and GaN have roughly half the response. They are used as highly stable piezoelectric, but require complicated vacuum processes for manufacturing, whereas $[(CH_2CH_3)_4N][FeBrCl_3]$ can be synthesized at room temperature.[11] Potentially interesting piezoelectric properties of the single crystals can be studied further, like the frequency and voltage dependence as well as the effect of temperature.

None of the mixed compositions of the $[(CH_2CH_3)_4N]_x[(CH_3)_4N]_{1-x}[FeBrCl_3]$ solid solution system exhibited ferroelectricity in their hysteresis, instead behaving as dielectrics with low leakage current even at high fields (up to 340 kV/cm).

Leakage current measurements reveal a trend of increasing leakage with increasing electric field for all samples, but the values vary by orders of magnitude. All of the mixed compositions have significantly lower current density values at 10 kV/cm, compared to the end member compositions $[(CH_3)_4N][FeBrCl_3]$ and $[(CH_2CH_3)_4N][FeBrCl_3]$. $[(CH_2CH_3)_4N]_{0.7}[(CH_3)_4N]_{0.3}[FeBrCl_3]$ displays the lowest leakage current at $5.8 \cdot 10^{-4}$ $\mu A/cm^2$. Dielectric spectroscopy from 0.05 – 10^6 Hz at room temperature was used to investigate the frequency dependent behavior of the samples. Behavior was similar for all samples and sample to sample variation made it difficult to extract more precise trends as a function of composition.

Dielectric measurements as a function of temperature showed that anomalies in the real permittivity ε' and loss tangent tan (δ) corresponded with the expected phase transition temperatures determined with DSC. These anomalies were independent of frequency, indicating that the transition was likely first order and behaved similarly as a typical curie phase transition in a metal oxide ferroelectric. The only exception to this was the moderately frequency dependent behavior observed in the composition $[(CH_2CH_3)_4N]_{0.5}[(CH_3)_4N]_{0.5}[FeBrCl_3]$, where a peak shift towards higher temperatures with

increasing frequency was observed. While this behavior is more reminiscent of a relaxor like material further investigation is necessary.

The low leakage currents in combination with the breakdown at high electric fields could make the mixed compositions interesting for dielectric applications. Composition close to the end members containing less than 10 mol% of the substitute cation, should be studied to further understand the effect of cation substitution on the ferroelectric and piezoelectric properties by possibly producing a single-phase material.

Possible causes for defects in the materials, likely influencing the electrical leakage and dielectric loss behavior, are non-stochiometric precursor ratios, residual solvent and structural inhomogeneities. Recrystallization can be used to mitigate some of these problems. Meanwhile the choice of solvent and crystallization rate likely have a significant influence on the cation-ratios within each crystallographic phase that forms during crystallization and therefore play a strong role in the structure and properties of the entire solid solution system.

Summary

A thorough investigation of the synthesis and properties of the $[(CH_2CH_3)_4N]_x[(CH_3)_4N]_{1-x}[FeBrCl_3]$ system was conducted. Limited solubility of the substitution ion in the reciprocal structure was observed, resulting in a metastable biphasic system. Crystallization rate, solvent and heating cycles influence the ratio of phases in the composition. Mixed crystals of the two space groups *Amm2* and $P6_3mc$ precipitate. Samples from aqueous solutions can grow as large single crystals or small, powder-like particles that can be hot pressed into disks. $[(CH_3)_4N][FeBrCl_3]$ was found to have piezo- and ferroelectric behavior, the ability withstand high electric fields and produce strains >0.1 %. All of the mixed compositions are dielectrics with low leakage current up to high fields of 340 kV/cm. $[(CH_2CH_3)_4N][FeBrCl_3]$ has a high piezoelectric response, with a d_{33} of -7/7 pC/N. Further investigations of single phase solid solutions containing small amounts of substitution organic cations are necessary to see the effect on the electrical properties. The plastic crystals can be synthesized at low temperatures and easily formed into complex shapes. For this reason, their functional properties remain very interesting for their potential use in low energy and small environmental footprint electronic devices in the future.

7. Appendix

7.1. Strain rate

To get a better understanding of the kinetics of the ferroelastic switching behavior and the domain wall motions, the strain rate can be plotted as a function of electric field, as seen in Figure 71. The strain rate is the first derivative of the strain ($\frac{dS}{dt}$).

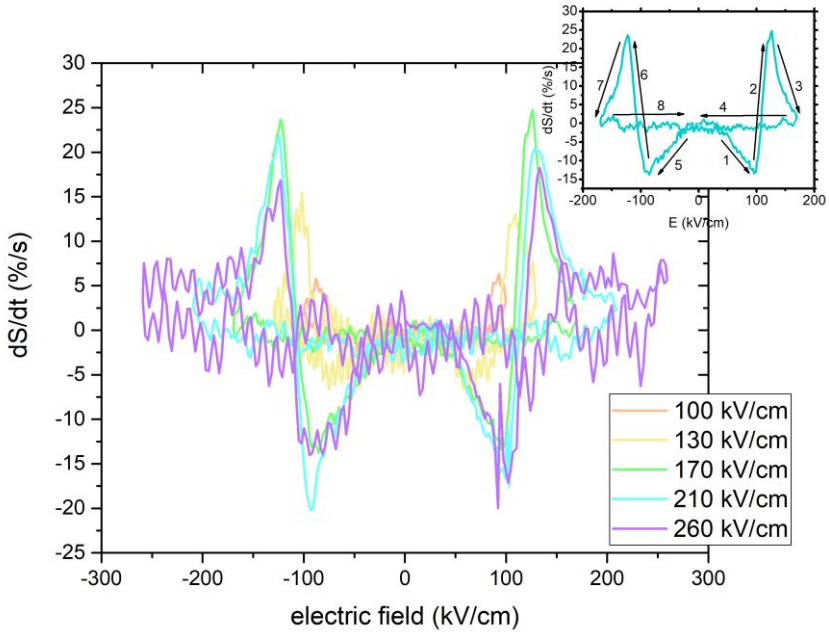

Figure 71: Strain rate ($\frac{dS}{dt}$) as a function of the applied electric field on a sample of $[(CH_3)_4N][FeBrCl_3]$ (slow crystallization through evaporation at room temperature) at different maximum electric fields.

The strain rate loop of $[(CH_3)_4N][FeBrCl_3]$ at 170 kV/cm was relatively free of noise, compared to other runs performed at different electric fields, so it was used to look into the characteristic points. This run is highlighted in the inset of Figure x. Four distinct peaks and a very symmetrical shape showed a lot of resemblance to the strain rate hysteresis loop of commercial soft PZT ceramics (PZT 5H).[47] This indicated two specific switching events on each side of the polarization cycle and high reproducibility. Starting from zero applied field, the strain rate value was negative in part 1, represented by shrinkage in the S-E loop. Since the sample is already in a poled state, based on the remanent polarization of the previous cycle, applying a field in the opposite direction caused a depoling and therefore a reduction in the strain. At a field of about 90 kV/cm, the first minimum was reached, indicating the point at which most of the anti-parallel oriented domains had moved to a perpendicular position relative to the electric field. From this point on (part 2 in Figure 71), the strain rate increased linearly while the domains rearranged to align with the applied field. When reaching a strain rate of zero, which

happened at an electric field of about 110 kV/cm, the first minimum of the strain in the S-E loop was reached. At the first maximum of the strain rate loop, which was at about 130 kV/cm, most of the domains had switched to a parallel orientation, relative to the electric field. In section 3 of the loop, the strain rate went back down to approximately zero at the maximum applied field. Since almost all the domains were already oriented parallel to the electric field, no significant increases in the strain were expected at even higher fields. While the electric field was removed in section 4 of the loop, the strain rate remained very stable at zero, which was also shown by the stability of the strain when the field is decreased. This indicates that only very little back-switching of domains took place. When applying a negative electric field, the same steps took place, so section 1 and 5, 2 and 6, 3 and 7, 4 and 8 are analogous.

Below 100 kV/cm, no distinct peaks could be observed in the strain rate loops. At higher fields up to 170 kV/cm, the four peaks started to become apparent, their position and intensity increasing with stronger fields. This shows that more and more domains were switched with higher electric fields. When applying even higher electric fields, the intensities of the peaks decreased, but remained approximately in the same position. The electric field at which the most ferroelastic domain-switching occurred remained the same at about 130 kV/cm, but the number of aligned domains was lower at higher fields. This makes sense when considering that all measurements were taken at a frequency of 10 Hz, meaning that the increase to the maximum field was much faster at 260 kV/cm, compared to 170 kV/cm. A possible explanation for the reduced number of parallel domains is the fact that they did not have enough time to switch at very high fields. So, in addition to the activation energy necessary to overcome the coercive field and to induce switching of domains, they also needed be given enough time to reorient.

All characteristic values of $[(CH_3)_4N][FeBrCl_3]$, P_r^*, polarization at E_{max}, I_{peak} and S_{pp} showed a distinct change in their behavior at field amplitudes of 170 kV/cm. Correlating these findings to the strain rate loops indicates that below 170 kV/cm, more domains were reoriented with increasing field strength which caused a rise in all the characteristic parameters. At fields higher than 170 kV/cm, fewer domains switched because there was not enough time for all of them to realign without adjusting the frequency. The ferroelastic domain switching saturated at 170 kV/cm, suggested by the plateau in S_{pp}, which was not affected by leakage current. A decrease in the slope of P_r^*, polarization at E_{max} and I_{peak} could suggest a saturation of the ferroelectric domain switching, but since the leaky behavior of the material became more prominent at high fields, it was difficult to predict a specific trend.

7.2. Positive-up negative-down measurement

A common and reliable method to separate ferroelectric switching from other effects that take place when an electric field is applied, is the positive-up negative-down (PUND) measurement. This was performed on the Aixacct ferroelectric test system on pressed disks with sputtered electrodes, analogous to the traditional ferroelectric measurements. Two electric field pulses in one direction were followed by the same pulses in the other direction. Afterwards, a fifth pulse was applied to normalize the sample. The shape of the pulse can be either triangular or trapezoidal, with the duration of the pulse and the maximum applied field determining the switching behavior. Pulse lengths ranged from 10-100 ms and the applied fields ranged from 10 – 250 kV/cm. Three typical pulse shapes and sequences can be seen in Figure 72.[48] All measurements were performed with a 1 s pause in between each pulse.

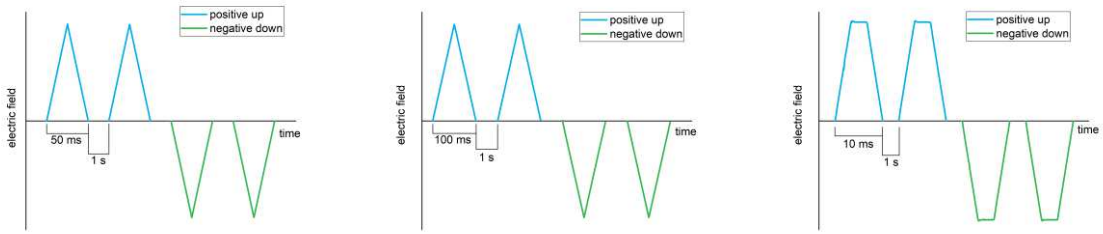

Figure 72: Pulse sequence and duration for positive-up negative-down (PUND) measurements. The electric field was varied from 10 – 250 kV/cm.

By applying a positive electric field pulse, the sample was polarized in one direction. This pulse contained the ferroelectric switching as well as any other contributions that could take place. By adding a second positive pulse, the signal only consisted of effects that took place in addition to the switching because of remanent polarization. By subtracting the second measurement from the first one, effects not related to the ferroelectric switching were eliminated. This measurement is usually done in both directions, by also applying two negative pulses. To ensure that a proper loop is obtained on the positive loop, a negative loop is done at the very beginning or end of each measurement.

PUND measurements were performed on a pressed sample of $[(CH_3)_4N][FeBrCl_3]$, (slow evaporation) at electric fields ranging from 10 – 250 kV/cm. Good ferroelectric response was achieved at around 200 kV/cm, as shown in Figure 73a.

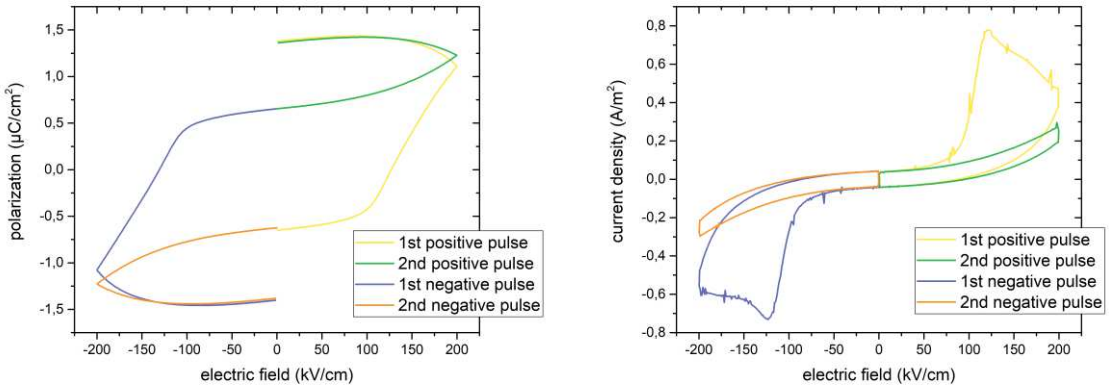

(a) (b)

Figure 73: (a) Polarization-electric field (P-E) and (b) current density-electric field (I-E) loops of a PUND measurement performed at 200 kV/cm maximum electric field of $[(CH_3)_4N][FeBrCl_3]$, manufactured from slow evaporation at room temperature. The pulse shape was a triangle with an overall duration of 100 ms.

During the first positive pulse, typical ferroelectric behavior was displayed by the sample. Since all domains were already aligned, polarization in the second positive pulse arose from leakage current only. The same happened during the negative pulses, where the domains switched on the first run and then stayed aligned. This was also represented in the current density-electric field plot in Figure 73b. The corrected ferroelectric hysteresis loops can be seen in Figure 74a. Leakage contributions were mostly removed. One can clearly see the effect of the pulse shape as well as the pulse duration on the appearance of the loop. The polarization was much bigger when the electric field was applied continuously for the traditional P-E hysteresis loops. At 170 kV/cm and 10 Hz, switching saturation was reached, meaning maximum domain switching. This was not the case for the PUND measurements, where a pulse of 100 ms (with a 50 ms rise time) was not enough to achieve this. Figure 74b demonstrates clearly that there was no saturation of the relaxed remanent polarization $P_{rrel+/-}$, which is the corrected polarization data of the PUND measurement. The minimum electric field necessary to achieve an opening of a ferroelectric loop was about 100 kV/cm. Polarization could be increased with longer pulse times at any field applied. A decrease of the $P_{rrel+/-}$ above 250 kV/cm with a triangular pulse shape and a pulse duration of 100 ms can only be explained by a degradation of the sample.

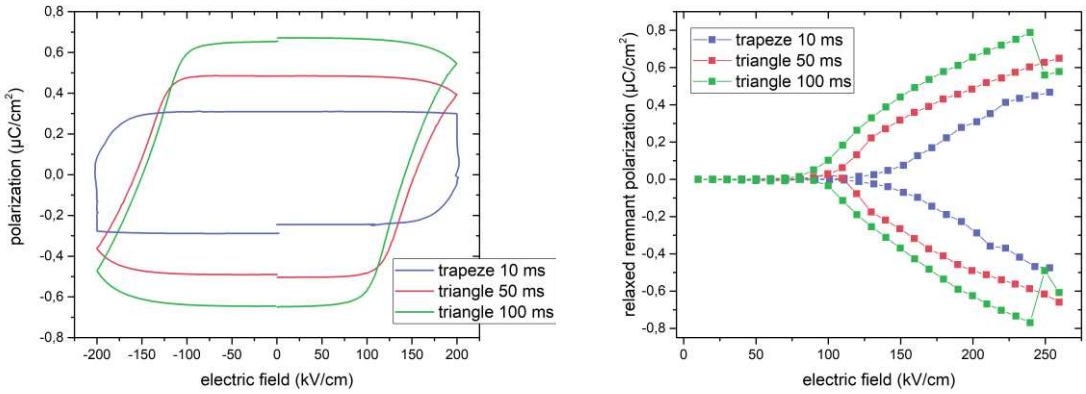

(a) (b)

Figure 74: (a) Corrected polarization-electric field (P-E) loops of a PUND measurement of a sample of $[(CH_3)_4N][FeBrCl_3]$, manufactured from slow evaporation at room temperature. Three different pulse shapes are compared. (b) Relaxed remanent polarization $P_{rrel+/-}$ as a function of the maximum electric field applied on a sample of $[(CH_3)_4N][FeBrCl_3]$, manufactured from slow evaporation at room temperature. Different pulse durations and pulse shapes have an impact on the measured values.

These experiments were originally performed to further understand the saturation switching behavior of $[(CH_3)_4N][FeBrCl_3]$. It was found though, that the relaxed remanent polarization increased up until the sample breaks down, due to the short pulse times, resulting in low $P_{rrel+/-}$ values. The duration needed to achieve complete switching exceeds the measuring times, so no information about the switching saturation was obtained.

7.3. Dielectric spectroscopy

Temperature dependent dielectric measurements were conducted in a selected frequency range (1000 – 10^6 Hz). The cooling parts of the thermal cycles are displayed in Figures 75 - 77, showing the real permittivity ε' and the loss tangent tan (δ) as a function of the temperature.

Upon cooling of $[(CH_3)_4N][FeBrCl_3]$ (Figure 75), a drop in both ε' and tan (δ) occurred right above the phase transition, indicating a structural transition influencing the electrical properties. The slight mismatch of the DSC and dielectric measurement could be caused by the supercooled phase transition.

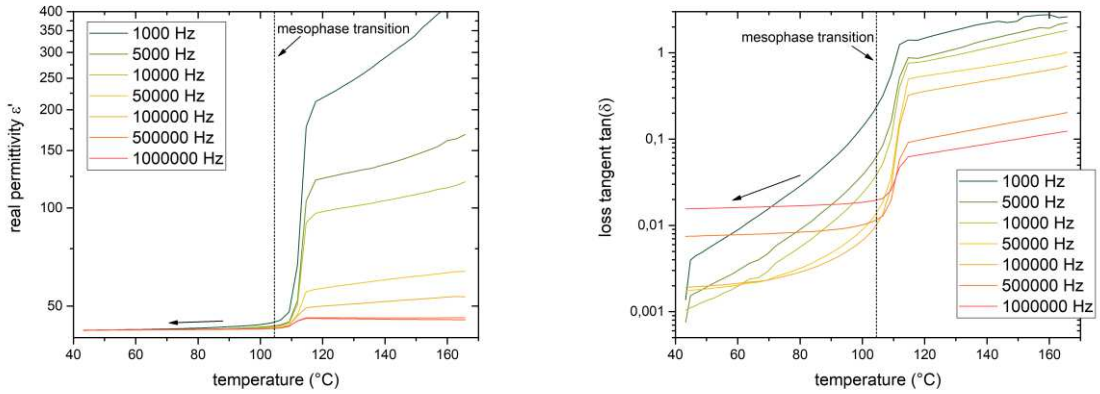

(a) (b)

Figure 75: Dielectric measurements of $[(CH_3)_4N][FeBrCl_3]$, investigating the real permittivity ε' (a) and the loss tangent tan (δ) (b) at different frequencies while cooling the sample down from 170 – 25 °C.

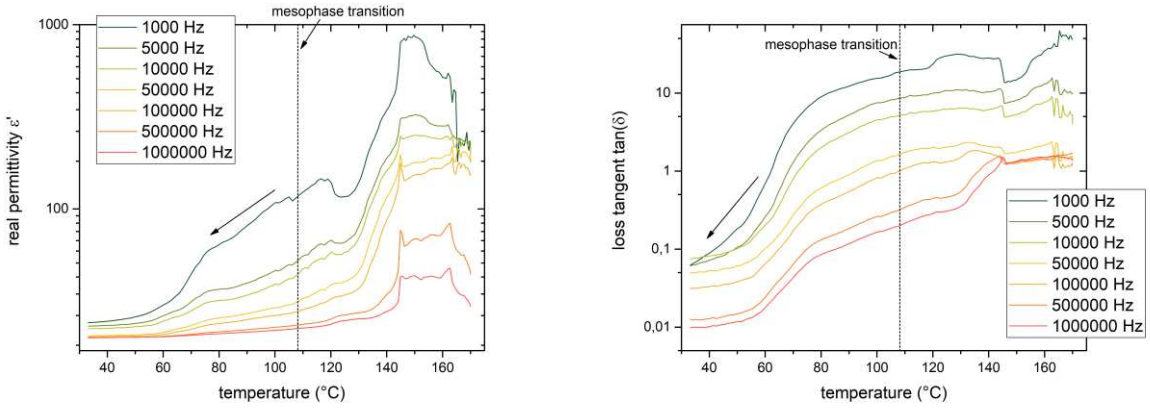

(a) (b)

Figure 76: Dielectric measurements of $[(CH_2CH_3)_4N]_{0.8}[(CH_3)_4N]_{0.2}[FeBrCl_3]$, investigating the real permittivity ε' (a) and the loss tangent tan (δ) (b) at different frequencies while cooling the sample down from 170 – 25 °C.

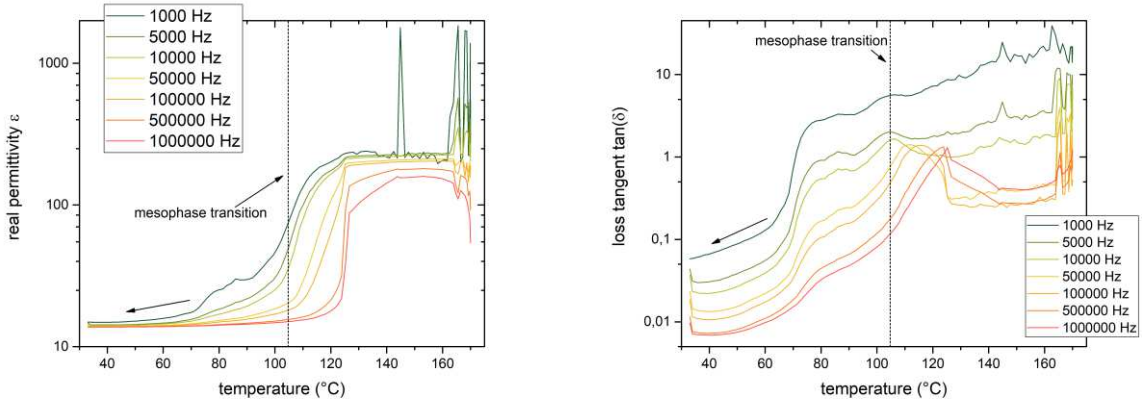

(a) (b)

Figure 77: Dielectric measurements of $[(CH_2CH_3)_4N]_{0.5}[(CH_3)_4N]_{0.5}[FeBrCl_3]$, investigating the real permittivity ε' (a) and the loss tangent tan (δ) (b) at different frequencies while cooling the sample down from 170 – 25 °C.

The ε' value of $[(CH_2CH_3)_4N]_{0.5}[(CH_3)_4N]_{0.5}[FeBrCl_3]$ has a large drop above the actual phase transition, and a very prominent spike at around 145 °C at 1000 Hz, as seen in Figure 77a. This spike could be an error of the measurement since it does not show up in any of the other frequencies. The drop of the loss tangent occurs at temperatures below the phase transition, and there was a frequency-dependent peak at 110 – 120 °C, which coincides with the phase transition (Figure 77b).

8. References

1. Trolier-McKinstry, S. Impact of ferroelectrics. *Am. Ceram. Soc. Bull.* **99**, 22, 23 (2020).

2. So, Y. W. *et al.* Effects of Lanthanide Dopants on the Ferroelectric Property of $Bi_4Ti_3O_{12}$ Thin Films. *Ferroelectrics* **271**, 347–352 (2002).

3. Ketsuwan, P. *et al.* Effects of Niobium Doping on Dielectric and Ferroelectric Properties of Chromium Modified Lead Zirconate Titanate Ceramics. *Ferroelectrics* **380**, 183–189 (2009).

4. Lusi, M. Engineering Crystal Properties through Solid Solutions. *Cryst. Growth Des.* **18**, 3704–3712 (2018).

5. Acosta, M. *et al.* $BaTiO_3$-based piezoelectrics: Fundamentals, current status, and perspectives. *Appl. Phys. Rev.* **4**, (2017).

6. Harada, J. *et al.* Ferroelectricity and Piezoelectricity in Free-Standing Polycrystalline

Films of Plastic Crystals. *J. Am. Chem. Soc.* **140**, 346–354 (2018).

7. Lutz, M., Huang, Y., Moret, M. & Klein Gebbink, B. Phase transitions and twinned low-temperature structures of tetraethyl-ammonium tetrachloridoferrate(III). *Acta Crystallogr. Sect. C, Struct. Chem.* **70**, 470–476 (2014).

8. Ben Brahim, K., Ben gzaiel, M., Oueslati, A. & Gargouri, M. Electrical conductivity and vibrational studies induced phase transitions in $[(C_2H_5)_4N]FeCl_4$. *RSC Adv.* **8**, (2018).

9. Evans, D., Hills, A., Hughes, D. & Leigh, G. Structure of tetraethylammonium tetrachloroferrate(III) and the mixed halide iron(III) complex, $[NEt_4][FeBrCl_3]$. *Acta Crystallogr. C.* **46**, 1818 (1990).

10. Wyrzykowski, D., Klak, J. & Warnke, Z. Structural and magnetic characteristics of tetramethylammonium tetrahalogenoferrates(III). *Inorganica Chim. Acta* **361**, 262–268 (2008).

11. Lueng, C., Chan, H., Surya, C. & Choy, C. Piezoelectric coefficient of aluminum nitride and gallium nitride. *J. Appl. Phys.* **88**, 5360–5363 (2000).

12. Fu, J., Liu, P., Cheng, J., Bhalla, A. & Guo, R. Optical measurement of the converse piezoelectric d33 coefficients of bulk and microtubular zinc oxide crystals. *Appl. Phys. Lett.* **90**, (2007).

13. Grove, C. S., Jelinek, R. V & Schoen, H. M. *Crystallization from Solution*. vol. 3 (Academic Press, 1962).

14. Aue, D. H., Webb, H. M. & Bowers, M. T. A thermodynamic analysis of solvation effects on the basicities of alkylamines. An electrostatic analysis of substituent effects. *J. Am. Chem. Soc.* **98**, 318–329 (1976).

15. Ibrahim, A.-B., Murgan, R., M. Kamil, A.-R. & Osman, J. Morphotropic Phase Boundary in Ferroelectric Materials. in *Ferroelectrics* (ed. Lallart, M.) (IntechOpen, 2011).

16. Pringle, J. M., Howlett, P. C., MacFarlane, D. R. & Forsyth, M. Organic ionic plastic crystals: recent advances. *J. Mater. Chem.* **20**, 2056–2062 (2010).

17. Simpkins, A. Robotic Tactile Sensing: Technologies and System. *IEEE Robot. Autom.*

Mag. **20**, 107 (2013).

18. Whatmore, R. Ferroelectric Materials. in *Springer Handbook of Electronic and Photonic Materials* (eds. Kasap, S. & Capper, P.) 1 (Springer International Publishing, 2017).

19. Damjanovic, D. Ferroelectric, Dielectric and Piezoelectric Properties of Ferroelectric Thin Films and Ceramics. *Reports Prog. Phys.* **61**, (1998).

20. Lines, M. E. & Glass, A. M. *Principles and Applications of Ferroelectrics and Related Materials*. *Oxford Classic Texts in the Physical Sciences* (Oxford University Press, 2001).

21. Arnau, A. & Soares, D. Fundamentals of Piezoelectricity. in *Piezoelectric Transducers and Applications* (ed. Vives, A. A.) 1–38 (Springer Berlin Heidelberg, 2008).

22. Horiuchi, S. & Tokura, Y. Organic ferroelectrics. *Nat. Mater.* **7**, 357–366 (2008).

23. Goldsmith, G. J. & White, J. G. Ferroelectric Behavior of Thiourea. *J. Chem. Phys.* **31**, 1175–1187 (1959).

24. Muralt, P. Stress Coupled Phenomena: Piezoelectric Effect. in *Encyclopedia of Materials: Science and Technology* (eds. Buschow, K. H. J. et al.) 8894–8897 (Elsevier, 2001).

25. Stewart, M. & Cain, M. Direct Piezoelectric Measurement: The Berlincourt Method. in *Characterisation of Ferroelectric Bulk Materials and Thin Films* vol. 2 37–64 (2014).

26. Kumar Bain, A. & Chand, P. *Ferroelectrics: Principles and Applications*. (Wiley-VCH Verlag, 2017).

27. Scott, J. F. & Paz de Araujo, C. A. Ferroelectric Memories. *Science.* **246**, 1400–1405 (1989).

28. Chen, J. & Panda, R. Commercialization of Piezoelectric Single Crystals for Medical Imaging Applications. in *Proceedings - IEEE Ultrasonics Symposium* vol. 1 235–240 (2005).

29. Gocha, A. Smart materials make smartphones. *Am. Ceram. Soc. Bull.* **97**, (2018).

30. Uchino, K. Manufacturing Methods for Piezoelectric Ceramic Materials. in *Advanced Piezoelectric Materials (Second Edition)* 385–421 (2017).

31. Ginsberg, A. P. & Robin, M. B. The Structure, Spectra, and Magnetic Properties of Certain Iron Halide Complexes. *Inorg. Chem.* **2**, 817–822 (1963).

32. Ye, H.-Y. *et al.* Molecular Ferroelectric with Most Equivalent Polarization Directions Induced by the Plastic Phase Transition. *J. Am. Chem. Soc.* **138**, 13175–13178 (2016).

33. Gesi, K. Effect of hydrostatic pressure on the phase transitions in tetraethylammonium tetrahalogenometallic compounds. *Ferroelectrics* **159**, 49–54 (1994).

34. Czapla, Z., Czupiński, O., Galewski, Z., Sobczyk, L. & Waśkowska, A. Successive phase transitions in tetramethylammonium tetrachloroferrate (III). *Solid State Commun.* **56**, 741–742 (1985).

35. Reichardt, C. *Solvents and Solvent Effects in Organic Chemistry*. (Wiley-VCH Publishers, 2003).

36. Campbell, C. F. *Phase Diagrams: Understanding the Basics*. (ASM International, 2012).

37. Yan, H. *et al.* The contribution of electrical conductivity, dielectric permittivity and domain switching in ferroelectric hysteresis loops. *J. Adv. Dielectr.* **01**, 107–118 (2011).

38. Schenk, T. *et al.* About the deformation of ferroelectric hystereses. *Appl. Phys. Rev.* **1**, 41103 (2014).

39. Damjanovic, D. Hysteresis in piezoelectric and ferroelectric materials. in *The Science of Hysteresis* (eds. Mayergoyz, I. & Bertotti, G.) 337–452 (2005).

40. Cain, M. G. *Characterisation of Ferroelectric Bulk Materials and Thin Films*. (Springer, 2014).

41. Dul'nev, G. N. & Zarichnyak, Y. P. Thermal and electrical conductivities of binary-alloy mixtures. *J. Eng. Phys.* **14**, 298–301 (1968).

42. Sharma, S., Renu, V. & Kumar, N. Effect of Electric Field and Temperature on Dielectric Constant and Piezoelectric Coefficient of Piezoelectric Materials: A Review. *Integr. Ferroelectr.* **167**, 154–175 (2015).

43. Zuo-Guang, Y. *Handbook of advanced dielectric, piezoelectric and ferroelectric materials*. (Woodhead Publishing in Materials, 2008).

44. Kleppe, N., Nurge, M. & Bowler, N. *Dielectric characterization of high-performance spaceflight materials*. *AIP Conference Proceedings* vol. 1650 (2015).

45. Kremer, F. & Schönhals, A. *Broadband Dielectric Spectroscopy*. (Springer Berlin Heidelberg, 2003).

46. Samara, G. The relaxational properties of compositionally disordered ABO_3 perovskites. *J. Phys. Condens. Matter* **15**, 367 (2003).

47. Viola, G. *et al.* Contribution of piezoelectric effect, electrostriction and ferroelectric/ferroelastic switching to strain-electric field response of dielectrics. *J. Adv. Dielectr.* **03**, (2013).

48. Everhardt, A. Novel phases in ferroelectric $BaTiO_3$ thin films: Enhanced piezoelectricity and low hysteresis. (University of Groningen, 2017).